Improving Dielectric Thin Films for Metal Insulator Metal Diodes and Perovskite Solar Cells

by

Abdullah Hamoud Q Alshehri

A thesis
presented to the University of Waterloo.
in fulfillment of the
thesis requirement for the degree of
Doctor of Philosophy
in
Mechanical and Mechatronics Engineering (Nanotechnology)

Waterloo, Ontario, Canada, 2021

AUTHOR'S DECLARATION

I hereby declare that I am the sole author of this thesis. This is a true copy of the thesis, including any required final revisions, as accepted by my examiners.

I understand that my thesis may be made electronically available to the public.

Abstract

Metal-insulator-metal (MIM) diodes are nano-electronic devices that operate by quantum tunneling of electrons through a thin dielectric layer to rectify high frequency alternating current (AC) to usable direct current (DC). Despite the crucial role played by the insulating layers, dielectric films for MIM diodes have not been thoroughly optimized. In this thesis, three fabrication techniques are explored to improve dielectric films for MIM diodes; doping of the insulator layer, using a rapid, scalable, open-air technique to deposit the insulator and the introduction of a thickness gradient.

Metal-insulator-insulator-metal (MIIM) diodes based on nitrogen-doped titanium dioxide (NTiOx) and aluminum oxide (NAlOx) are fabricated by plasma-assisted atomic layer deposition. The doped MIIM diodes show higher performance than diodes with undoped insulators due to the introduction of defect-mediated conduction mechanisms. A Pt/TiOx-NAlOx/Pt diode shows an asymmetry of 8.76 × 103, nonlinearity of 4, and zero-bias responsivity of 36.8 A W^{-1}.

MIM diodes are then fabricated by atmospheric pressure chemical vapor deposition (AP-CVD), demonstrating that clean room fabrication is not a prerequisite for quantum-enabled devices. The MIM diodes fabricated by AP-CVD show a lower effective barrier height, lower turn on voltage, lower zero-bias resistance, and better asymmetry than similar diodes made by plasma-enhanced atomic layer deposition.

An atmospheric pressure spatial atomic layer deposition (AP-SALD) system is then used to produce spatially varying chemical vapor deposition rates on the order of angstroms per second. An Al_2O_3 film is printed with nm-scale thickness gradients in as little as 45 s and used for combinatorial and high-throughput (CHT) analysis of MIM diodes. By testing 360 Pt/Al_2O_3/Al diodes with 18 different Al_2O_3 thicknesses on a single substrate, the insulator thickness (6.5 to 7.0 nm) for optimal diode performance is determined.

A double thickness gradient metal-insulator-insulator-metal diode is then fabricated by AP-CVD for the first time. This high-throughput method is used to produce 414 MIIM diodes with 414 different Al_2O_3/ZnO film-thickness combinations on a single substrate. The nm-scale Al_2O_3/ZnO films are printed in only 2 minutes and the entire device fabrication

takes 7 h, much less than conventional approaches for studying a large number of insulator-thickness combinations. High performance diodes (asymmetry = 2580, nonlinearity= 13.1 and responsivity=12 A/W) are observed when a resonant tunneling mechanism is dominant for insulator thicknesses of 7.4 nm (Al_2O_3) and 3.4-4.4 nm (ZnO).

Finally, to demonstrate the applicability of the CHT approach to other devices, an Al_2O_3 thickness gradient thin film encapsulation layer is deposited by AP-CVD on a perovskite solar cell stack for the first time and a convolutional neural network is used to analyze the perovskite stability. The rapid nature of AP-CVD enables thicker films to be deposited at a higher temperature than is practical with conventional methods. The CHT analysis shows enhanced stability for 70 nm encapsulation films. The stability of the combinatorial perovskite solar cells is observed over 94 hours and shows the efficacy of thicker encapsulation layers.

Acknowledgements

I would like to express my special thanks to Prof. Mustafa Yavuz for accepting me to undertake my PhD studies at a university of high standing such as the University of Waterloo. His support, patience, and guidance during my studies are truly appreciated. NO words can ever sufficiently express my thanks and gratitude to Prof. Kevin Musselman. He has been a supportive older brother, adviser and developer. I learned a great deal from him, including critical thinking and time organization, as well as how to write papers for high-impact journals.

I also thank my groupmates and co-authors for my papers, especially for their help to complete this work. Special appreciation goes to all my friends in Canada who made my life easier and more fun.

I am also grateful to Drs. David Muñoz-Rojas and Viet Huong Nguyen from the University Grenoble Alpes-CNRS, Grenoble, France for their collaboration on AP-SALD that enabled part of this work.

Furthermore, I would like to thank my funding sources for their support during my journey: Sattam bin Abdulaziz University, the Saudi Arabian Cultural Bureau, the Waterloo Institute for Nanotechnology and CMC Microsystems.

Thank you to my family for their patience with my study abroad, which has taken me away from them over the past seven years. Also, a special thanks to my wife for her support, help, encouragement and patience when I spent so much time in the university away from her.

Dedication

To my father: Hamoud

To my mother: Fatima

To my wife: Amjad

To my brothers: Mohammed, Hassan, Fares, Osama and Qasem

To my sister: Afaf

Table of Contents

List of Figures

List of Tables

List of Abbreviations

AFM	Atomic Force Microscopy
ALD	Atomic Layer Deposition
AP-SALD	Atmospheric Pressure Spatial Atomic Layer Deposition
AP-CVD	Atmospheric Pressure Chemical vapor Deposition
CHT	Combinatorial High Throughput Techniques
CsI	Cesium Iodide
CVD	Chemical Vapor Deposition.
DEZ	Diethylzinc
DMF	Dimethylformamide
DMSO	Dimethyl sulfoxide
DT	Direct Tunneling
FAI	Formamidinium Iodide
FNT	Fowler-Nordheim Tunneling
GAI	Gallium Iodide
GPC	Growth Per Cycle
IoT	Internet of Things
MIM	Metal-Insulator-Metal
MIIM	Metal-Insulator-Insulator-Metal
MI^4M	Metal-Insulator-Insulator-Insulator-Insulator-Metal
PEALD	Plasma Enhanced Atomic Layer Deposition.
PF	Poole Frenkel Emission
PL	Photoluminescence

PSC	Perovskite Solar Cell
R&D	Research and design
Rectenna	Rectifying antenna
RF	Radio frequency
RT	Resonant Tunneling
ST	Step Tunneling
SE	Schottky Emission
TAT	Traps Assisted Tunneling
TFE	Thin Film Encapsulation
TIIP	Titanium Isopropoxide
TMA	Trimethylaluminum
Uv-vis	Ultraviolet–visible
XPS	X-ray Photoelectron Spectroscopy
XRD	X-ray diffraction

Chapter 1
Introduction

1.1 Introduction to high-frequency MIM diodes

The global demand for energy, as well as its applications in our lives, continues to increase, thus it has become important to find alternative sources of green and economical energy to eliminate the use of fossil fuels due to the high cost and negative environmental effects. Researchers have recently worked on improving energy-harvesting devices that convert electromagnetic waves into usable electricity. A rectenna (RECTifying antENNA) can work as an energy-harvesting device in different electromagnetic energy regimes from infrared (IR) to ultraviolet (UV). It consists of two major components: an antenna and a rectifier diode as shown in Figure 1.1.

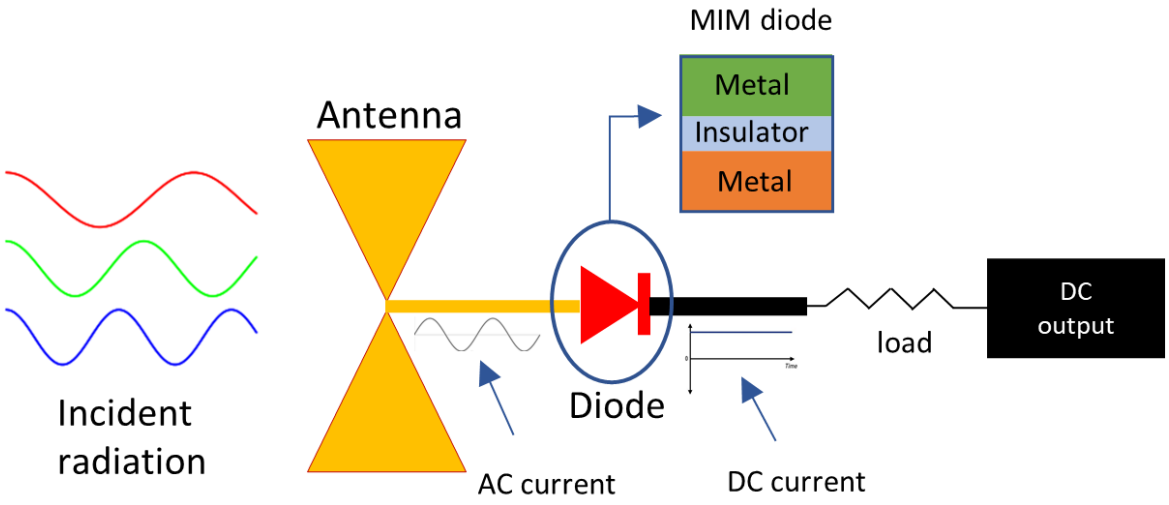

Figure 1.1. Block diagram of a rectenna device.

Electromagnetic waves (GHz or THz range) captured by the nanoantenna are converted to an alternating current (AC) and subsequently rectified to usable direct current (DC) transferred to a load. A rectifier diode in the rectenna system plays an important role to improve the conversion efficiency of electromagnetic waves into electricity. In order to harvest more energy, a rectenna that works at high frequencies is needed because of the frequency of the IR and visible light spectrum. Schottky diodes are popular rectifying devices based on a semiconductor-metal junction but are limited to GHz or low-THz-frequency applications such as IR detectors. For solar or infrared harvesting, rectifier diodes that operate in the high-THz range are needed to rectify the high-frequency current that is received from the antenna. Metal-insulator-metal (MIM) diodes are capable of rectification in the high-frequency range because they are based on a femtosecond electron transport mechanism through the insulator. Thus, the MIM diode is

attractive for many applications such as solar rectennas[1], IR detectors[2], and wireless power transmission[3].

A MIM diode is a nonlinear nano-electronic device that operates by quantum tunneling of electrons through a thin dielectric layer stacked between two metal contacts. Rectification is achieved as a result of the asymmetry of the two potential barriers formed between the metals and the insulator, which influences the electron tunneling rates. While the electrons tunnel to overcome the potential barriers, the tunneling probability is reduced by the barrier. A larger potential barrier at one metal-insulator interface results in a larger reduction in the tunneling probability than at the other metal-insulator interface.

The materials selection of the diode determines its energy band diagram and has a significant impact on diode performance, as shown in Figure 1.2. Potential barriers are formed at the interfaces of the metals and the insulator. The barrier height ($q\phi$) is the difference between the work function (ψ) of the metal and the electron affinity (χ) of the insulator, and the barrier width is defined by the insulator thickness. E_f in Figure 1.2 indicates the Fermi level in the diode.

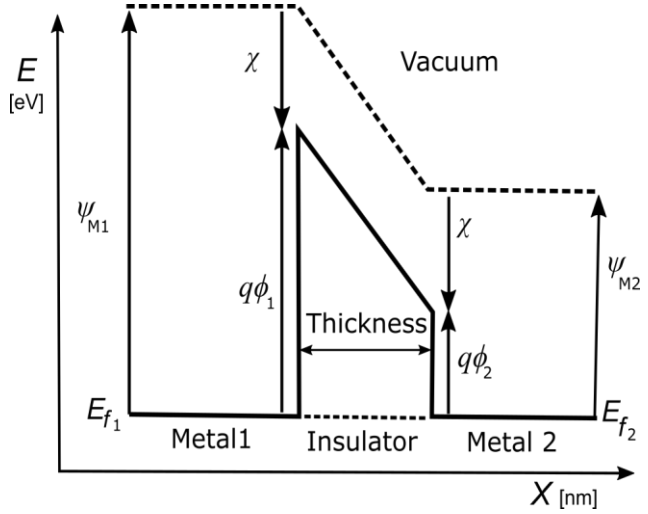

Figure 1.2. Energy diagram of a MIM diode.

1.2 Current MIM diode challenges

A number of challenges need to be addressed in MIM diodes, most of which follow from unoptimized device architectures and fabrication processes. Notably, optimization of the critical dielectric (insulator) films for MIM diodes is largely unexplored, including the deposition method, the role of defects, and the thickness of the dielectric.

To work effectively in detection and harvesting applications, MIM diodes require high figures of merit (asymmetry, nonlinearity, and responsivity), and a low diode resistance and capacitance are needed to achieve a low RC time constant that enables high-frequency rectification. Attempts to improve the figures of merit of MIM diodes often increase the diode resistance, which is undesirable[4–6]. Previous work has attempted to reduce the MIM diode capacitance by minimizing the diode area using fabrication techniques such as electron beam lithography[7]; however, resistance is expected to increase when the diode area is reduced[8].

Similarly, increasing the thickness of the insulator layer in order to reduce the capacitance is expected to increase the diode resistance. The lack of a material combination that exhibits a suitably low barrier, low resistance, effective tunneling and good antenna-diode matching remains a challenge[9].

Furthermore, high-throughput fabrication of MIM diodes is limited by slow deposition rates and the need for a vacuum environment. Atomic layer deposition (ALD) is the most common technique used to deposit the insulator in a MIM diodes due to its ability to deposit nanoscale films with high accuracy and uniformity. However, the ALD process is slow and high ALD temperatures can hinder the design of a small area diode that requires lift off of an ALD film, due to the possibility of degrading the resist layer. Etching is the method commonly used to pattern an ALD films but difficulty producing precise features makes this method undesirable. The need for high temperatures, specific metal films for oxidation, and complex compound precursors in previous techniques, as well as challenges in reproducibility, highlight the need for new methods to reliably deposit enabling films for cost effective quantum devices.

The effect of the insulator layer thickness on the performance of MIM diodes has been studied theoretically. Previous simulation work has varied the insulator thickness in the range of 0.5-2 nm[10], 1-4 nm[4], and 4-10 nm[6], along with the metal work function difference, to optimize the diode figures of merit. In contrast, few experimental studies have been performed, which is likely due to the challenging and time-consuming nature of MIM diode fabrication. Slow vacuum-based deposition methods are traditionally used to produce the required ultra-thin insulator layers. Krishnan *et al.*[11] and Chin *et al.*[12] examined the effect of NiO and Nb_2O_5 thickness, respectively. However, their studies were limited to only two insulator thicknesses.

Novel techniques are therefore needed for depositing nanoscale films in a manner that facilitates thickness dependent studies in MIM diodes and other emerging devices.

1.3 Overview of the thesis

The thesis focuses on optimizing the state of the art of MIM diodes, including their fabrication and performance, by improving the fabrication techniques and properties of the dielectric films. Three different dielectric film fabrication strategies are explored, including doping the insulators, insulator deposition by rapid atmospheric pressure chemical vapor deposition, and insulator deposition by a combinatorial and high-throughput technique.

One of the objectives of this thesis is the optimization of the fabrication and characterization of multi-insulator MIIM diodes. In Chapter 4, defect engineering in multiple insulator layers is introduced as a strategy to simultaneously improve the figures of merit and lower the resistance of MIM diodes. To achieve this end, doped insulator layers are employed in double-insulator MIM diodes (MIIM) for the first time. Titanium dioxide (TiO_x) and aluminum oxide (AlO_x) films doped with nitrogen are fabricated using plasma enhanced atomic layer deposition (PEALD) and integrated into MIIM diodes. Doping-induced defects are found to provide control over the dominant conduction mechanisms in the insulators. By doping a specific insulator in the MIIM diode, asymmetric conduction mechanisms are imparted, which result in high figures of merit (notably a responsivity that surpasses the Schottky diode limit), while simultaneously maintaining low diode resistance.

Another objective is to investigate a new scalable fabrication technique for MIM diodes. In Chapter 5, an atmospheric pressure spatial atomic layer deposition (AP-SALD) system

operated to produce atmospheric pressure chemical vapor deposition (AP-CVD) conditions is utilized for the first time to fabricate Al_2O_3 insulating films for MIM diodes. The performance of the MIM diodes fabricated by AP-CVD is characterized and compared to MIM diodes fabricated by conventional, vacuum-based PEALD.

As discussed in Section 1.2, nanoscale thickness-dependent studies are required to accelerate the development of emerging devices, such as MIM diodes and perovskite solar cells (PSCs). This can be addressed by using combinatorial and high-throughput (CHT) techniques[13]. In CHT approaches, a thin film is produced whose properties (in this case, thickness) vary across its surface. Multiple devices can then be produced at different locations on the film surface and compared without batch-to-batch variation, making the technique faster and more reliable. This approach also significantly reduces the time and material costs during experimentation. In addition to CHT analysis, films with thickness gradients present an opportunity for novel functionality.

In Chapter 6, large-area thin films with thickness gradients on the nanometer scale are manufactured using spatially varying AP-CVD techniques. This allows the study of different film thicknesses at once. Metal oxide films (Al_2O_3, ZnO) are rapidly printed with nanoscale thickness gradients in atmosphere and used in CHT studies of MIM diodes.

In Chapter 7, the CHT approach is extended to MIIM diodes. Double-insulator (Al_2O_3, ZnO) thickness-gradients films are introduced into MIIM diodes by AP-CVD for the first time. This high throughput approach allows the fabrication and characterization of more than 414

insulator thickness combinations on a single wafer, enabling quick identification of the most effective Al_2O_3 and ZnO insulator thicknesses. The thickness gradient and CHT technique isn't only applicable to MIM diodes but can also be applied to other nanoscale devices.

Another objective of this thesis is demonstrating the CHT approach in another device. In Chapter 8, Al_2O_3 thickness gradient films are deposited in atmosphere as encapsulation layers for PSCs and CHT studies are performed to analyze the role of thickness in the degradation of perovskites films on a single sample.

In advance of presenting these experimental results in Chapters 4-8, Chapter 2 provides a review of previous work on MIM and MIIM diodes, as well as the AP-SALD technique used in this thesis. Chapter 3 describes the fabrication process used for the MIM diodes throughout the thesis. Finally, Chapter 9 discussed the key conclusions for this work and directions for future research.

Chapter 2
Theory and Literature Review

2.1 Principle of operation of MIM diodes

a) MIM diode with a single insulator

Figure 2.1 explains the principle of operation of a MIM diode. Consider a designed MIM diode with different metal electrodes where Metal 2 has a smaller work function than Metal 1. Figure 2.1a shows the diode in the unbiased condition (V=0), where equilibrating the Fermi levels of the two metal contacts forms a trapezoidal barrier atop the potential barrier. Reverse current results when negative bias (V<0) is applied to Metal 2 and the band diagram has a small shift in its shape due to raising of the fermi level of Metal 2, as shown in Figure 2.1b. In this configuration, the electrons must tunnel through the entire dielectric thickness (t). Forward bias current occurs when positive bias is applied to Metal 2 (V>0), resulting in a change in the trapezoidal barrier to a triangular barrier, allowing Fowler-Nordheim tunneling (FNT) to occur, as shown in Figure 2.1c. In FNT, the probability of electron tunneling through the triangular barrier increases due to

the reduced tunneling distance atop of the barrier, which follows from the difference in work functions of the metals (Δφ) and the applied voltage (V). A further increase in positive bias will further decrease the tunneling distance and consequently the tunneling current density will increase. The diode's rectification capability follows from the reduced tunneling distance in the forward direction that encourages electron tunneling under forward bias, as compared to the limited reverse bias current at the same voltage magnitude. Electron conduction mechanisms in MIM diodes will be discussed in detail in Section 2.2.

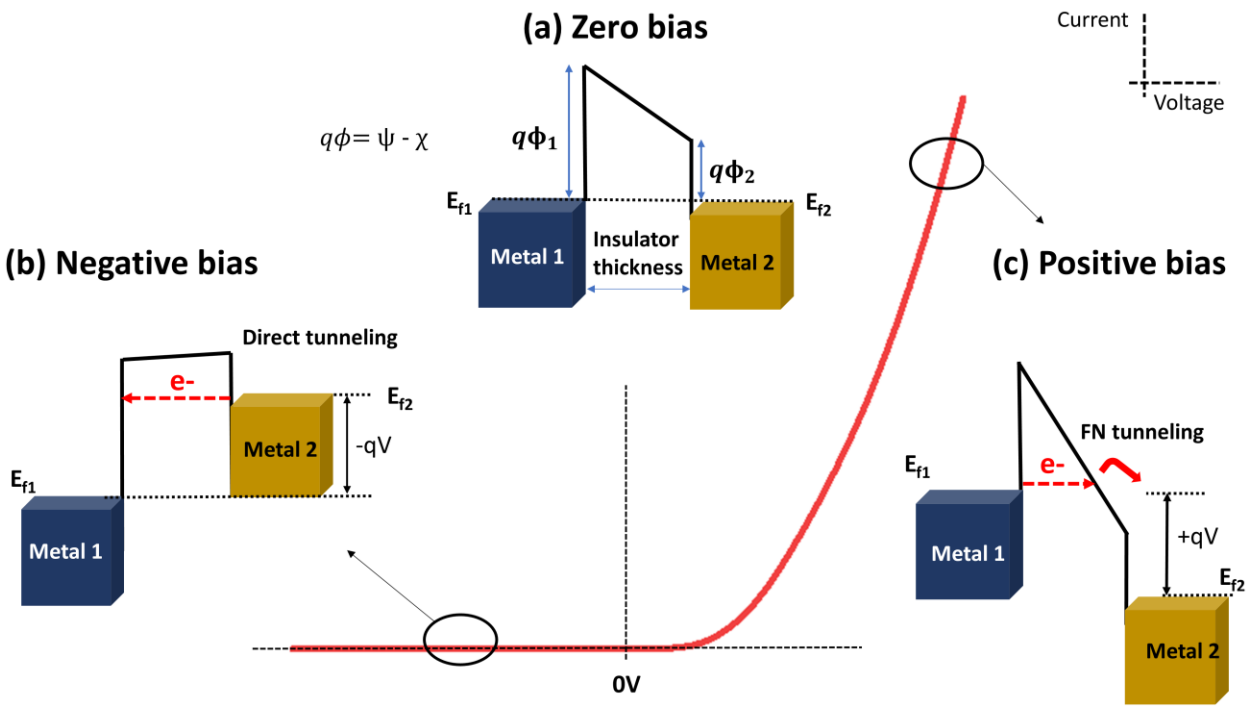

Figure 2.1. Energy band diagrams of a MIM diode for (a) unbiased, (b) negative bias, (c) positive bias conditions.

b) MIIM diode with double insulators

Adding another insulator with different electronic properties, including electron affinity (χ) and band gap (E_g), can improve the diode performance. In addition to using different metals, insulators with different electron affinities can form asymmetric barriers at the interfaces. Thus, a further enhancement in the figures of merit (FOM) and lower diode resistances can be obtained. This enhancement results from the dominance of asymmetric conduction mechanisms. The most common conduction mechanisms in double insulators are step tunneling (ST) and resonant tunneling (RT), both of which depend on properties and thicknesses of different insulators. Figure 2.2 explains the principle of operation of an MIIM diode by ST. It shows a designed MIIM diode with different metal electrodes and insulators, where Metal 2 has a smaller work function than Metal 1 and Insulator 2 has a higher electron affinity than Insulator 1. By applying positive bias to Metal 2, forward bias current occurs, as shown in Figure 2.2a. The electron tunnels from Metal 1 through Insulator 1 and then overcomes the barrier of Insulator 2 to reach Metal 2. This reduces the effective tunneling distance and results in a higher current density. In reverse bias, the electron needs to tunnel from Metal 2 to Metal 1 through both insulators resulting in a lower tunneling probability, as shown in Figure 2.2b.

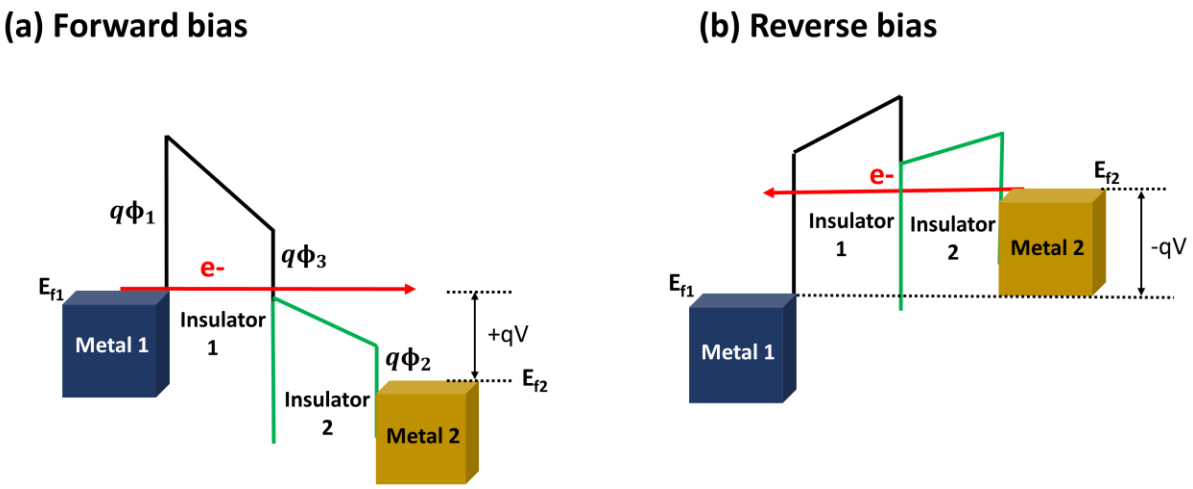

Figure 2.2. (a) Step tunneling at forward bias, (b) direct tunneling at reverse bias.

In RT, a triangular quantum well (QW) is formed between the two insulators, and has discrete energy levels. The shape of this well (depth and width) mostly depends on the thickness of the higher-electron-affinity layer (Insulator 2 in Figure 2.3a). It should be noted that a thicker insulator is preferable for forming a deep and wide well that leads the electron to tunnel using the available energy pathways. Forward bias occurs when the positive bias is applied to Metal 1, resulting in an increase in the Fermi level of Metal 2 in order to reach the energy level in the QW, then the electron can tunnel through the insulators with the assistance of this energy pathway, as shown in Figure 2.3a. In reverse bias, the electron must tunnel through the entire width of the insulators from Metal 1 to Metal 2, as shown in Figure 2.3b.

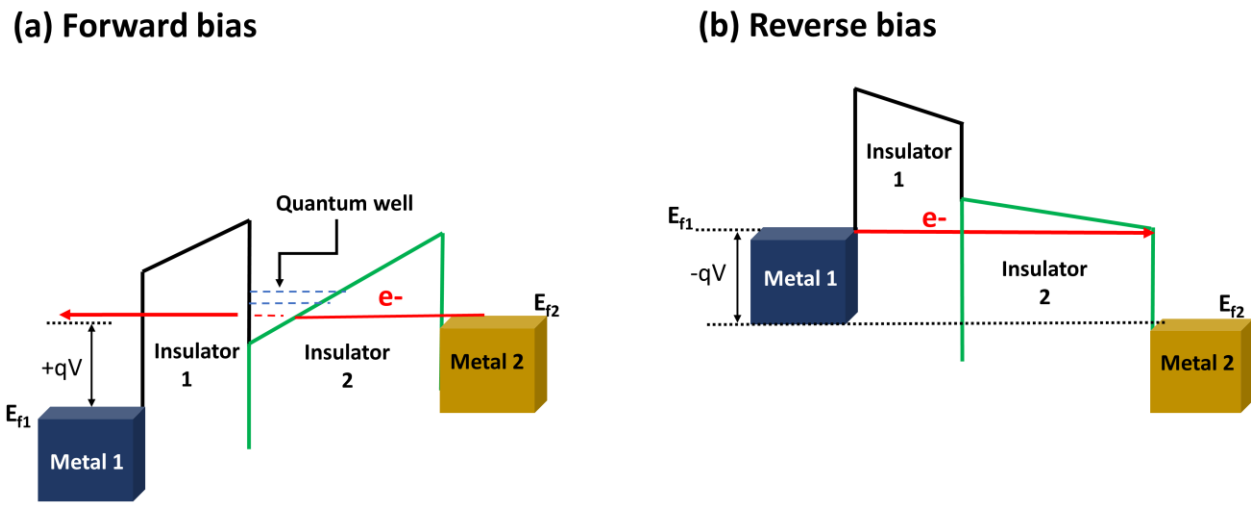

Figure 2.3. (a) Resonant tunneling at forward bias, (b) direct tunneling at reverse bias.

To understand and improve the rectification performance of MIM diodes, it is important to study the effect of many factors, such as the type of conduction mechanisms present, the barrier heights between the metals and the insulators, as well as any roughness and defects in the insulator.

2.2 Conduction mechanisms of MIM diodes

The conduction current in the insulator of MIM diodes includes two types: electrode-limited and bulk-limited conduction mechanisms.

1. *Electrode-limited conduction mechanisms*: These mechanisms depend on the metal electrode and metal-insulator interface. The barrier height at the interface is an important parameter that can be affected by material selection and their deposition methods. These

mechanisms include: (a) Schottky or thermionic emission (SE) and (b) quantum electron tunneling.

(a) Schottky or thermionic emission: the conduction results from the transport of electrons over the metal-insulator barrier when the electron energy obtained by thermal activation is higher than the barrier at the metal-insulator interface, as shown in Figure 2.4. The expression for the current density resulting from SE (J_{SE}) is defined as[14]

$$J_{SE} = \frac{120 m_{ox}}{m_0} T^2 exp\left[\frac{-q(\phi_B - \sqrt{qE/4\pi\varepsilon_0\varepsilon_r})}{kT}\right] \quad (2.1)$$

where q is the elementary charge, ε_r is the optical dielectric constant (i.e., the dynamic dielectric constant), ε_0 is the permittivity in free space, k is the Boltzmann constant, T is the temperature, m_{ox} is the effective electron mass in the insulator, m_0 is the free electron mass, E is the electric field, and $q\phi_B$ is the Schottky barrier height.

(b) Quantum electron tunneling through the thin insulator occurs by two mechanisms. Direct tunneling (DT) and Fowler–Nordheim tunneling (FNT). DT takes place when the electrons travel through the entire barrier thickness. In FNT, applying a large electric field can tunnel the electrons a shorter distance through the triangular portion of the barrier that results from the difference between the metal work functions, as shown in Figure 2.4. FNT is considered as the most important mechanism for increasing rectification performance. The FNT current density is expressed as[15,16]:

$$J_{FNT} = C_1 \frac{1}{\phi_b} E^2 exp\left[\frac{-C_2 m_{ox}^{1/2} \phi_b^{3/2}}{E}\right] \quad (2.2)$$

where C_1 and C_2 are constants; and ϕ_b is the metal-insulator barrier height. DT and FNT can be observed on an FNT plot (ln (J/V^2) versus 1/V). On an FNT plot, a positive slope at low voltage is attributed to the dominance of DT while a negative slope at high voltage is attributed to dominant FNT[17]. The metal-insulator barrier heights can be calculated from the slopes of the FNT plots.[18]

$$\text{Slope}_{FNT} = (m_{ox}/\, m_0)\ \phi_b^{1/3}$$

2. *Bulk-limited conduction mechanisms:* These mechanisms depend on the electrical properties of the insulator. Thus, the deposition method or adding impurities to create defects sites (electron traps) can impact the film properties and the extent of bulk-limited conduction. These mechanisms include: (c) Poole Frenkel and (d) trap-assisted tunneling emission.

(c) Poole-Frenkel (PF) emission: conduction results from the transport of electrons through the insulator via traps states. The trapped electrons emit from the traps into the insulator conduction band by thermal excitation under presence of the electric field, as shown in Figure 2.4. For PF, the current density is expected to have the following relationship with the electric field E[14].

$$J_{PF} = E\ exp\left[\frac{-q(\phi_T - \sqrt{qE/\pi\varepsilon_0\varepsilon_r})}{kT}\right] \tag{2.3}$$

where q is the elementary charge, ϕ_T is the trap energy of the insulator, ε_r is the optical dielectric constant, ε_0 is the permittivity in free space, k is the Boltzmann constant, and T is the temperature.

(d) Trap assisted tunneling (TAT): In TAT, the electrons tunnel to the anode via the trap states. TAT is expected to be the dominant mechanism in ultrathin (less than 10 nm) defective oxides[19,20]. The current density expression is[21]:

$$J_{TAT} \sim exp\left[\frac{-4\sqrt{2qm_{ox}}}{3\hbar}\phi_T^{3/2}/E\right] \tag{2.4}$$

where $\hbar$ is the reduced Planck constant.

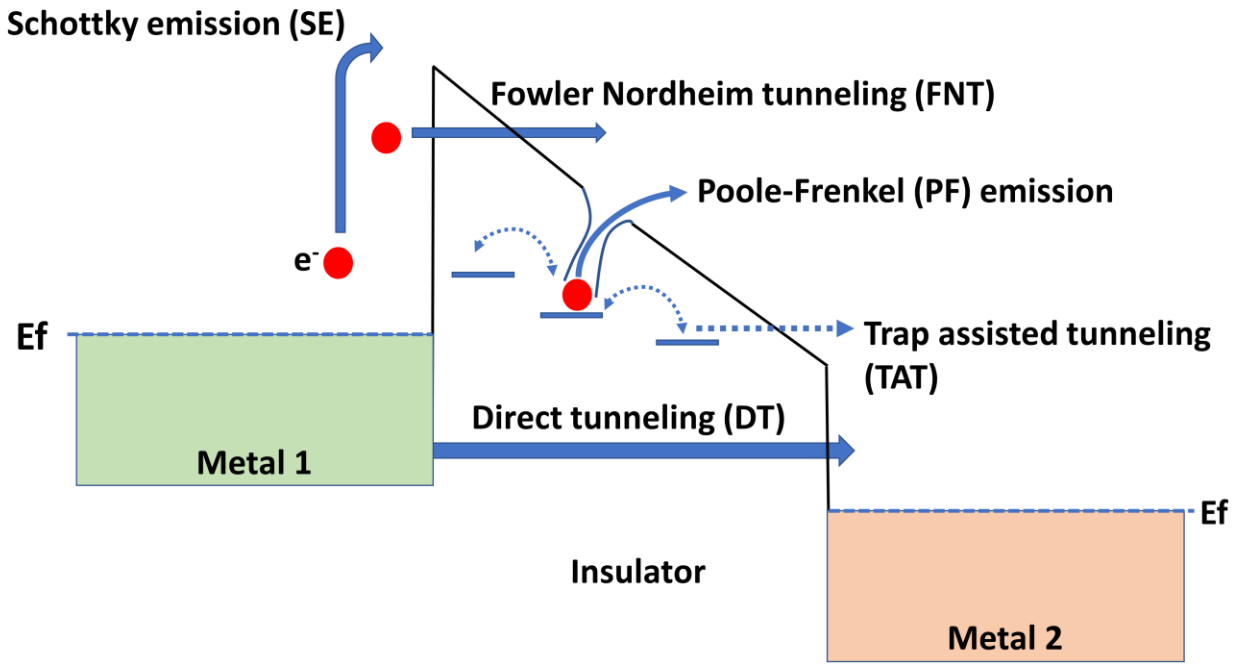

Figure 2.4. Conduction mechanisms on Metal-insulator-metal diodes.

2.3 Figures of merit of MIM diodes

The rectification performance of MIM diodes is characterized by three figures of merit (asymmetry, nonlinearity, and responsivity) as listed in Table 2.1, which are affected by several

factors, including metal and insulator selection, insulator thickness, and barrier heights between the metals and the insulator.

Table 2.1. Figures of merits of MIM diodes

Asymmetry	$Asy = \lvert I_F/I_R \rvert$	(2.5)
Nonlinearity	$NL = \frac{dI}{dV} \Big/ \frac{I}{V}$	(2.6)
Responsivity	$Res = \frac{d^2I}{dV^2} \Big/ \frac{dI}{2dV}$	(2.7)

The asymmetry, which is the absolute value of the ratio of forward current (I_F) to reverse current (I_R) at a voltage, can be calculated from Equation 2.5, where a value greater than 1 indicates rectification in the diode. Nonlinearity, which is a measure of the degree of variation from a linear I-V curve. It is the ratio of the slope of the I-V curve to the conductance at a bias, as shown in Equation 2.6. Responsivity is a measure of the ability of a MIM diode to generate DC current per input of AC electrical power. It is defined numerically in Equation 2.7 as the ratio of the second derivative to the first derivative of the I-V curve at a bias. The output direct current (I_{dc}) obtained from a diode is proportional to the diode responsivity (*Res*) and the AC incident power (P_{AC}) supplied to the diode from an antenna:

$$I_{dc} = Res \times P_{AC} \tag{2.8}$$

Diodes for detection applications should also have high responsivity, as the detectivity (*D*) is proportional to the responsivity of the detector system (Res_{system}), including the diode[22]:

$$D = Res_{system}\sqrt{A_{abs}}\sqrt{R_d/4kT} \tag{2.9}$$

where A_{abs} is the absorption area for the detector, R_d is the diode resistance, k is the Boltzmann constant and T is the absolute temperature.

Lastly, the cut-off frequency f_c is the theoretical maximum rectified frequency that can be achieved by a MIM diode. A high cut-off frequency can be achieved with a small resistance and capacitance as shown in Equation 2.10:

$$f_c = \frac{1}{2\pi RC} \tag{2.10}$$

where R is the series resistance of the MIM diode with an antenna and usually $R_{antenna}$=50-100 ohm. The differential diode resistance of the MIM diode is described by Equation 2.11 and it is equal to the ratio of voltage change to the current change. C is the diode capacitance, which can be calculated using Equation 2.12.

$$R = \frac{dV}{dI} \tag{2.11}$$

$$C = \varepsilon_0 \varepsilon_r \frac{A}{d} \quad \text{[single insulator]}$$
$$\frac{1}{C} = \frac{1}{C_1} + \frac{1}{C_2} \quad \text{[double insulators stacked in series]} \tag{2.12}$$

where A is the diode contact area, d is the insulator thickness, $\mathcal{E}_0$ is the permittivity of free space, and $\mathcal{E}_r$ is the relative permittivity or dielectric constant of the insulator. To increase the cut off frequency, decreasing the diode capacitance is required. This can be achieved by decreasing the

diode contact area, using a low dielectric insulator such as Al_2O_3 (ε_r= 9), or increasing the insulator thickness. However, a thicker insulator reduces the tunneling probability, leading to an increase in the diode resistance. This thesis addresses this trade-off in Chapter 4 by doping a thick low-dielectric layer, in order to increase the thickness without an unwanted increase in resistance.

2.4 . Previous MIM and MIIM diodes

2.4.1 Fabrication of previous MIM diodes

The insulator layer in the MIM stack plays a crucial role in determining the diode performance[16]. It is typically deposited using vacuum-based methods, such as sputtering[23], anodic oxidation of sputtered films[24], electron beam deposition[25], and especially atomic layer deposition (ALD)[26], which is commonly used due to its ability to deposit nanoscale films with high accuracy and uniformity. For example, Abdel-Rahman *et al*. [23] fabricated Cu-CuO-Cu diodes. The copper metal was deposited by sputtering and patterned by electron beam lithography then the copper oxide was deposited by sputtering. Their MIM diode showed a responsivity of 2.2 A/W. Alimardani *et al*.[16] used an ALD system to deposit different insulators with different electron affinities for MIM diodes, including Nb_2O_5, Ta_2O_5, ZrO_2, HfO_2, Al_2O_3, and SiO_2 . They study the impact of the insulator on diode performance and reported asymmetries of 10^3 for Al_2O_3, 8 for ZrO_2, 5 for SiO_2, and 1 for Ta_2O_5, HfO_2, and Nb_2O_5.

Some deposition processes have been introduced to fabricate thin films at atmospheric pressure for nano-electronic devices that utilize quantum phenomena. Atmospheric pressure metal organic vapor phase epitaxial growth (AP-MOVPE), or atmospheric pressure metal

organic chemical vapor deposition (AP-MOCVD), has been used to fabricate InGaAsP multi quantum-well structures for optical devices[27], and a chemical vapor deposition (CVD) furnace operated at atmospheric pressure has been used to deposit a TiO_2 film in a tunneling transistor[28]. These atmospheric techniques have been extended to MIM diodes. The Langmuir-Blodgett method, where an air-water interface is used to deposit a monolayer of a material at the liquid surface by immersion of the substrate into the liquid, was used to deposit 10,12-pentacosadiynoic acid as an insulator layer between two Ni metal electrodes. The I-V diode characteristic showed tunneling behavior with an asymmetry of 110 at 0.2 V[29]. ZnO films for MIM diodes were also deposited by this method and showed an asymmetry of 12 and responsivity of 16 A/W[30]. Furthermore, thermal and anodic oxidation have been used to grow thin CrO_x and Nb_2O_5 films on Cr and Nb layers for MIM diodes[24,31]; and the diodes showed sensitivities as high as 1.29 A/W at 0.3 V.

2.4.2 Performance of previous MIM diodes

Most previous reports have a focus on improving the diode performance by optimizing material selection and by using different fabrication processes. Using similar metal contacts is expected to result in a symmetric I-V curve. However, some systems such as $Al/Al_2O_3/Al$[32], $Ni/NiO/Ni$[33], $ZrCuAlNi/Al_2O_3/ZrCuAlNi$[34], and $Nb/Nb_2O_5/Nb$[35] show asymmetric I-V behavior due to the formation of two different metal-insulator interfaces arising from dissimilar deposition processes, thus creating regions of enhanced leakage currents through the barrier.

Using dissimilar metals with different work functions increases the asymmetry ratio due to different barrier heights at the metal-oxide interface. Chin *et al.*[12] observed that the highest

FOMs were observed for $Nb/Nb_2O_5/Pt$, which displayed an asymmetry ratio of 1500, nonlinearity of 4, and responsivity of 10 A/W at 0.5 V. This work has been improved by fabricating the same $Nb/Nb_2O_5/Pt$ diode with a contact area of 6400 μm^2. The optimal FOMs included an asymmetry of 7.74×10^3, nonlinearity of 4.7, zero bias responsivity of 15 A/W and current density of 10^{-2} A/cm^2 at +0.5 V[24].

However, high-FOM diodes that used a single insulator layer showed high diode resistance which is undesirable. One promising strategy to tackle this trade-off has been the use of multiple insulator layers (e.g., MIIM)[5,8,26]. MIIM studies have shown improvement in FOMs over the single insulator diode. Asymmetry was increased, even when the same metals were used, which was attributed to the difference in electron affinity of the insulators.

Ferhat *et al.*[26] fabricated double MIIM and quadra MI^{4}M diodes using TiO_2 and Al_2O_3 insulators with dissimilar metals pads, Cr and Al. They showed asymmetry ratios of 3 and 90 at 1.6 V for MIIM and MI^{4}M diodes respectively. Table 2.2 summarizes the FOMs of a variety of MIM, MIIM, and MI^{4}M diodes at different biases.

Table 2.2. Properties of previously reported MIM, MIIM, and MI^{4}M diodes.

Diode structure and area [μm^2]	Insulator thickness [nm]	Insulator growth method	Asymmetry at ~0.5V	Max nonlinearity	Zero-bias responsivity [A/W]	Max responsivity [A/W]	Max current density [A/cm^2]	Zero bias resistance (R_0) [ohm]	Zero bias resistance [ohm] normalized to A=100 μm^2	Ref
Al/AlO_x/Pt [8×10^{-3}]	0.1-0.2	Oxidation	1	9.9×10^{-6}	-	1×10^{-3}	43×10^{6}	1.25×10^{2}	1×10^{-2}	[32]
Al/AlO_x/Pt [4×10^{-3}]	1-2.5	Oxidation	-	-	-	4.8	5×10^{2}	312×10^{6}	1.25×10^{4}	[36]
Al/AlO_x/Pt [4×10^{-3}]	2.5-3.5	Oxidation	1	3×10^{-3}	-	10^{-2}	500×10^{3}	1.65×10^{3}	6.6×10^{-2}	[37]
Cr/TiO_x-AlO_x/Al [10^2]	3	PEALD	1	2	-	-	2×10^{-2}	$\sim10^{8}$	$\sim10^{8}$	[26]
Cr/TiO_x-AlO_x-TiO_x-AlO_x/Al [10^2]	3	PEALD	8	8	-	-	8×10^{-2}	$\sim10^{7}$	$\sim10^{7}$	[26]
Cr/AlO_x-HfO_x/ Cr	4	ALD	9	11	-	2.5	-	$\sim10^{6}$	-	[38]
Co/CoO_x-TiO_x/Ti [7.1×10^{-2}]	5.2	Plasma Oxidation	1.1	-	1.2	4.4	10^{5}	14×10^{3}	10	[39]
Al/AlO_x/Ag [1.76×10^{6}]	0.75	Plasma Oxidation	1.2	12.5	9	9	3.4×10^{-10}	27×10^{3}	4.75×10^{8}	[40]
Ni/NiO/Pt [2.5×10^{-3}]	1-2	Oxidation	-	9	-	6.5	3.6×10^{-2}	$\sim10^{7}$	2.5×10^{2}	[41]
Ni-NiO-NbO_x-Cr/Au [1.55×10^{-1}]	5	Plasma Oxidation	1.1	-	0.46	3	6.4×10^{5}	3.8×10^{2}	0.6	[22]
Ni/NiO-ZnO/Cr [4×10^{2}]	7	Sputtering	16	-	2.5	8	4.3×10^{-2}	234×10^{6}	9.3×10^{8}	[42]
Highest reported FOMs: Nb/NbO_x/Pt [6.4×10^{3}]	15	Oxidation	7.74×10^{3}	4.7	15	16.9	10^{-2}	$\sim7.8\times10^{9}$	5×10^{11}	[12]

2.5 Conventional Atomic Layer Deposition (ALD) vs Atmospheric Pressure Spatial Atomic Layer Deposition (AP-SALD)

ALD is a vacuum-based technique used to deposit conformal, uniform, pinhole-free thin films with precise control of thickness in the sub-nanometer range. Figure 2.5a illustrates the working principle of conventional temporal ALD. A fixed substrate is exposed to the first precursor 1 and is given enough time for the precursor to saturate the surface, such that a reactive monolayer is formed. Then precursor 1 is purged by an inert gas (typically N_2) to remove any unreacted precursor. After that, precursor 2 is injected to react with the monolayer of precursor 1. In some ALD systems, a plasma (e.g., oxygen plasma) is used to facilitate the reaction of the

precursors. After waiting for the precursors to react completely, the vacuum chamber is again purged. By repeating this cycle, the desired film thickness can be growth, one atomic layer at a time. The drawbacks of this technique are that it is very slow because it has the sequential injection and purge steps for the precursors, and that it is mostly done in vacuum and that makes scaling up more complicated and expensive.

Atmospheric pressure spatial atomic layer deposition (AP-SALD) is a fast and scalable thin film deposition technique that operates in atmospheric pressure. Recently, AP-SALD systems have been utilized to grow uniform films for different applications including solar cells[43], transistors[44], and light emitting diodes[45]. AP-SALD has the ability to control the film thickness in the atomic scale range and produce uniform and pinhole-free films at modest temperatures (e.g., 100-350°C)[46]. By adjusting the conditions to allow precursor mixing in the gas phase, chemical vapor deposition (CVD) can also be performed in the same system[47,48]. AP-CVD conditions are attractive for device manufacturing, as it has been shown that higher deposition rates are obtained, while still producing smooth, pinhole-free, conformal films with thicknesses proportional to the number of cycles[46]. Figure 2.5b illustrates the working principle of AP-SALD. The system has two precursors separated by an inert gas. The inert gas is bubbled through the precursors to vaporize them and enable the precursor delivery. The substrate is placed under the atmospheric gas manifold with a small vertical separation (typically less than 100μm) to expose the substrate to the alternating precursors. To grow a monolayer, the substrate moves underneath the first precursor to adsorb the first layer of the precursor, then the substrate moves under the flow of inert gas to remove the remaining precursor 1 in the gas phase, then the monolayer is completed when the substrate moves under precursor 2 to react with the layer of

precursor 1. By repeating this cycle with oscillations of the substrate back and forth, the desired thickness can be grown as a high-quality, pinhole-free film. Figure 2.6 illustrates the plasma-enhanced ALD (PEALD) and AP-SALD systems used in this work.

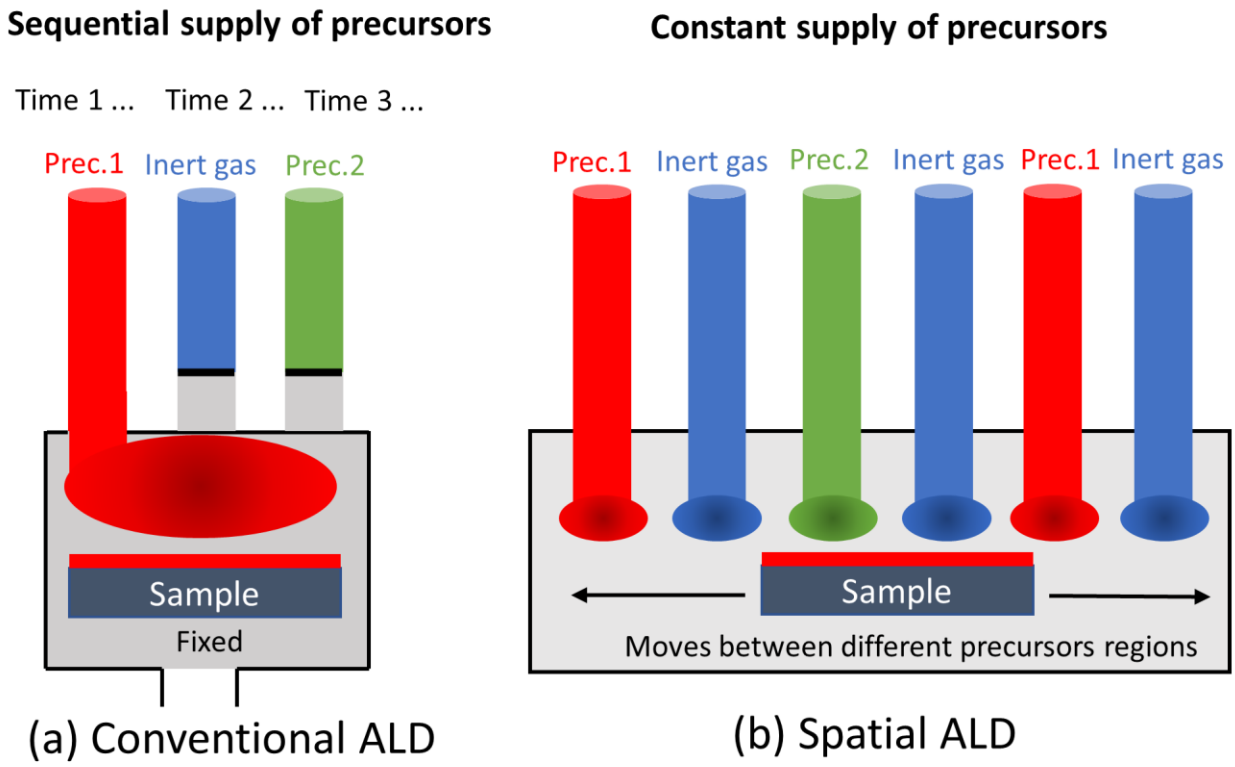

Figure 2.5. Schematic representation of an ALD deposition cycle by (a) conventional (temporal ALD) and (b) AP-SALD. In temporal ALD the sample is fixed, while it is exposed to the precursors sequentially in time. In spatial ALD the sample oscillates across the different precursors zones to reproduce an ALD cycle.

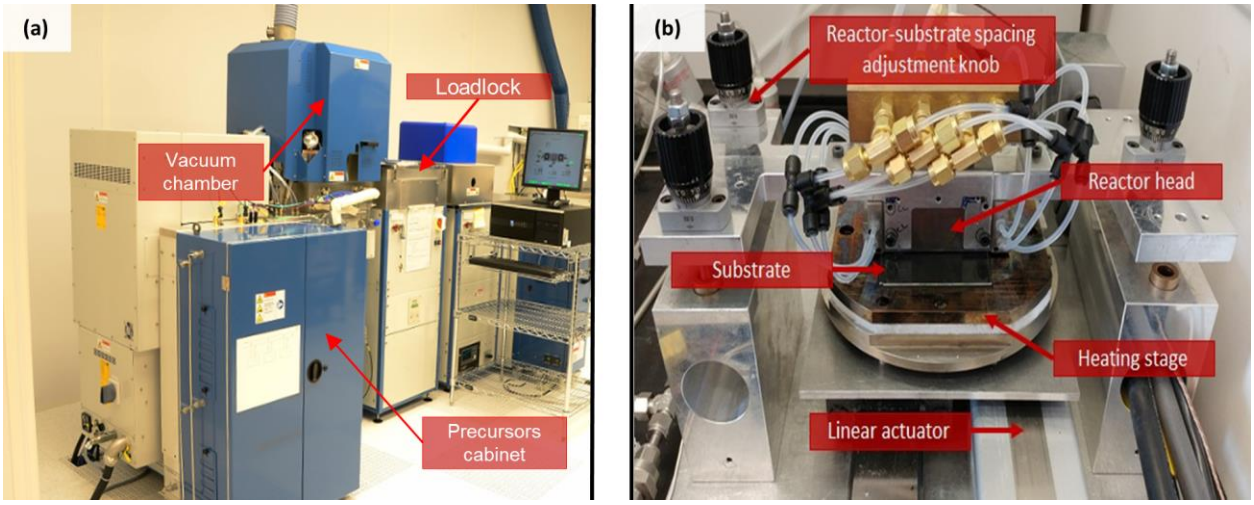

Figure 2.6. (a) PEALD Oxford-FlexAL system in clean room. (b) AP-SALD in open air (in a fume hood).

Chapter 3
Metal-Insulator-Metal Fabrication Process

3.1 Material selection

MIM diodes were fabricated using platinum (Pt) as the bottom electrode and aluminum (Al) as the top electrode, except in Chapter 4 where Pt was also used as the top contact for some devices. TiO_2, Al_2O_3, and/or ZnO were selected as the thin dielectric layers between the two metals. The metals are chosen based on their high difference in work function to form two different barrier heights and achieve asymmetric behavior in the I-V curve. Pt has a work function of 5.65 eV[49] and Al has a work function of 4.28 eV[50]. The electron affinity of TiO_2 is 4 eV[51], Al_2O_3 is 1.3-2.8 eV[52], and ZnO is 4.5 eV[53].

3.2 Sample preparation and first photoresist spin coating

The diodes were fabricated on SiO_2 wafers. The SiO_2 wafer was cleaned sequentially in baths of acetone and IPA (isopropanol), and subsequently rinsed with deionized water and dried with N_2. Before photoresist coating, the substrate was coated with hexamethyldisilazane

(HMDS) for 25 s with a spin speed of 3000 rpm to increase the adhesion of photoresist to the silicon oxide surface. The micro negative photoresist, maN-1410, was used because it is suitable for the lift off process, and compatible with the designed photomask. With negative photoresist, the unexposed area was removed from the sample after development. The spin coating was started by dispensing the resist over ¾ of the substrate surface followed by spinning at 500 rpm for 5 s with an acceleration of 100 rpm/s. The wafer was further spun at 3000 rpm for 60 s with an acceleration of 500 rpm/s. This spin speed results in an approximately 1.2 μm thick resist layer. To remove the solvent component in the photoresist, the samples were soft baked at 100°C for 90 s.

3.3 First photolithography and development

This technique uses UV light to pattern the micro-scale shapes on the photoresist using a designed photomask. The photomask consists of a glass plate with a patterned chromium film. The photolithography process is applied twice before depositing the metal electrodes. In the first exposure, Mask 1 is used to pattern the desired shape on the photoresist, as shown in Figure 3.1a. MaN-1410 resist requires a dose of 350 mJ/cm^2 at 365 nm. The Karl Sauss (MA6) Mask Aligner is calibrated to provide 10 mW/cm^2 of UV at 365 nm. The wafer is therefore exposed for 35 s. The MA6 exposure parameters are summarized in Table 3.1.

Table 3.1. The MA6 exposure parameters for photolithography method

Alignment gap	20 µm
Wedge error Compensation (WEC) offset	0
WEC type	contact
Exposure type	vacuum
Pre vacuum	5 s
Full vacuum	15 s
Purge vac	10 s

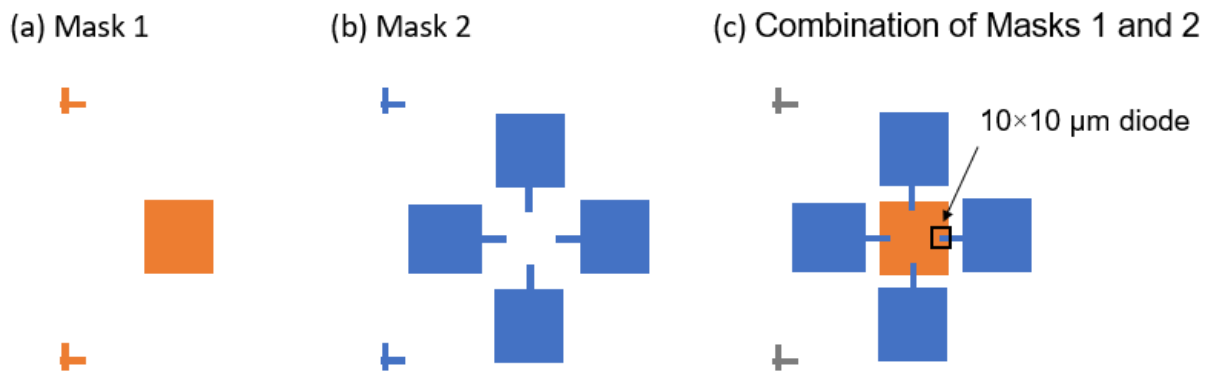

Figure 3.1. (a) Mask 1, (b) Mask 2, (c) Combination of Masks 1 and 2.

The development is used to remove unexposed areas of the photoresist. The sample was developed in Ma-D 533/S (tetramethylammonium hydroxide (TMAH)) and agitated lightly for 120 s at room temperature. After development, the sample was placed in deionized (DI) water for one minute followed by a DI rinse under the water tap and N_2 drying steps. The resolution attained with this recipe is 3.5 µm. The undercut achieved is approximately 2 µm.

3.4 Bottom metal deposition and lift off

Platinum (Pt) with 100 nm thickness and 1 Å/s deposition rate was deposited on the substrate using an E-beam evaporation (EBV) system with a base pressure set to 4×10^{-6} torr. The lift off method uses a suitable chemical solvent to create structures from a deposited film. In this method, the undesired deposited film is removed with photoresist while the film deposited on the substrate remains. To lift off the maN-1410 photoresist, the following four process were applied to the sample:

•Sonicate the sample in acetone for five minutes at 50°C.

•Sonicate the sample in Remover PG for five minutes at 50°C.

•Sonicate the sample in acetone for five minutes at 50°C.

•Sonicate the sample in IPA for five minutes at 50°C, then blow dry with nitrogen.

3.5 Insulator thin film deposition

PEALD and AP-SALD/AP-CVD were used to deposit different insulator films as detailed in Chapters 4-7.

3.6 Second photoresist coating, photolithography, deposition and lift off

To deposit the metal top contact, the same processes that were used to deposit the bottom contact are repeated with a few changes in the second UV exposure and metal deposition. The Pt contact on the sample was aligned with Mask 2 (shown in Figure 3.1b) for the UV exposure. Pt or Al was deposited as a second contact on top of the insulator layer. After that, the second lift

off process was applied to remove the photoresist and achieve the desired MIM diode, as shown in Figure 3.1c. A device area of 10 × 10 μm was obtained. Reactive ion etching was used to remove any oxidant on top of the electrode layers. A flow of Argon plasma (30 sccm) was generated by radio frequency (RF) with a power of 20 W for 60 s. Figure 3.2 presents a summary of the fabrication process.

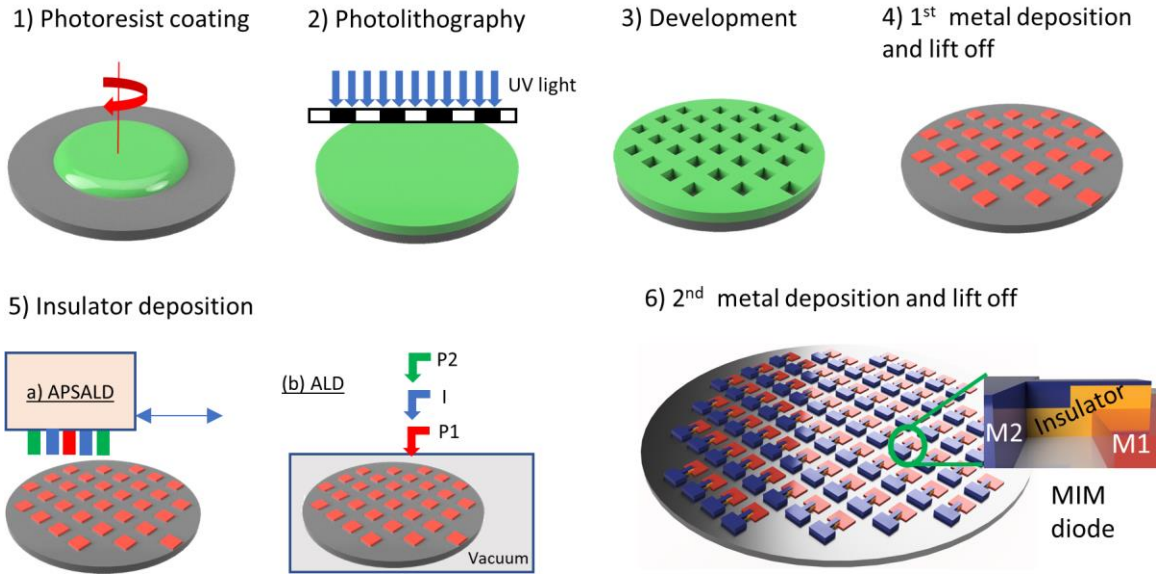

Figure 3.2. Summary of the fabrication process of a MIM diode using AP-SALD and ALD.

3.7 Characterization

Film thickness measurements: A Woollam M-2000 DI ellipsometer with a wavelength range of 200–1800 nm was used to measure the thickness and the refractive indices of the insulator films, which were modeled using the Cauchy formula.

Atomic force microscopy: A Dimension 3100 atomic force microscope (AFM) was used to measure the thickness and roughness of the insulator films.

Ultraviolet–visible (Uv-vis) absorption spectroscopy for PSCs: The PSC samples were placed inside a humidity chamber and moved to measure different locations on the surface of the samples. An Ocean Optics DH-2000 lamp was used as a light source and an Ocean Optics HDX spectrometer was used to measure the transmitted light.

Photoluminescence (PL) spectroscopy for PSCs: A Quanta Master 8000 Fluorometer by HORIBA was used to perform PL measurements on PSCs by exciting at 680 nm and observing the spectral range of 810 to 850 nm. The samples were moved to measure different locations on their surfaces.

X-ray diffraction (XRD): XRD measurements of ZnO films that were deposited on glass substrates were performed with a XPERT-PRO diffractometer with Cu Kα radiation (X-ray wavelength of 0.154 nm).

X-ray photoelectron spectroscopy (XPS): A VG Scientific ESCALAB 250 system was used to examine the surface of the films using Al Kα X-rays.

Optical microscopy: Optical microscope images of an Al_2O_3 thickness gradient film were obtained with an Olympus MX61A optical microscope.

Diode characterization: A Keithley 4200-SCS semiconductor characterization system connected to a probe station was used to measure the I–V properties of the MIM diodes.

Chapter 4

Metal-Insulator-Insulator-Metal Diodes with Responsivities Greater Than 30 A/W Based on Nitrogen-Doped TiO_x and AlO_x Insulator Layers

4.1 Overview

Researchers have recently worked on improving energy-harvesting devices based on rectennas that convert environmental electromagnetic waves into DC power. Near-zero-bias-voltage operation is desired for the rectenna diode since the self-limiting operating voltage for power conversion is between 0.03 and 0.1 V[39]. Conventional rectifier diodes show low rectification at low biasing, limiting their use in the conversion of low-power electromagnetic waves. Consequently, a high-response diode is needed. The current responsivity is a critical parameter that describes the rectifying capabilities of a diode. In Schottky diodes, the electron transport is by thermal emission. Thus, the current responsivity of Schottky diodes is limited by the inverse of the thermal voltage $V_T = (q/2kT)$, where q is the electron charge, which corresponds to 19.4 A/W at room temperature. Schottky diodes reached this maximum responsivity over 50

years ago. To surpass this limit, diodes must be constructed with barriers that are not fully dependent on thermal activation.

In contrast to Schottky diodes, MIM diodes are not restricted by the *q/2kT* responsivity limit[54,55]. However, the highest zero-bias responsivity obtained for a MIM diode, a Nb/Nb_2O_5/Pt diode reported by Chin *et al.* was 15 A/W[12,54]. This is significantly lower than that of the best Schottky diodes (19.4 A/W). Backward tunnel diodes have shown a higher responsivity of 23.5 A/W by using an inter-band tunnelling mechanism[54,55]. To improve the responsivity of MIM diodes, it is necessary to fabricate diodes that do not fully depend on SE or PF conduction mechanisms, but instead leverage the quantum-tunnelling mechanism that is not restricted by the responsivity limit[54]. Ideally this should be conducted without sacrificing the other figures of merit, as well as the resistance and capacitance of the diode. To work effectively in these applications, MIM diodes require high figures of merit (asymmetry, nonlinearity, and responsivity), and a low diode resistance and capacitance are needed to achieve a low RC time constant that enables high-frequency rectification.

In this chapter, defect engineering in multiple insulator layers is introduced as a strategy to simultaneously improve the figures of merit and lower the resistance of MIM diodes. To achieve this, doped insulator layers are employed in double-insulator MIM diodes (MIIM) for the first time. Titanium dioxide (TiO_x) and aluminum oxide (AlO_x) films doped with nitrogen are fabricated using remote PEALD and integrated into MIIM diodes. Doping-induced defects are found to provide control over the dominant conduction mechanisms in the diodes.[56] By doping a specific insulator in the MIIM diode, asymmetric conduction mechanisms are imparted, which

result in high figures of merit (notably a responsivity that surpasses the Schottky diode limit), while simultaneously maintaining low diode resistance.

4.2 Experimental

Five types of diodes were fabricated in this work, as illustrated in Figure 4.1a-e. Undoped Pt/TiO_x/Pt and Pt/TiO_x-AlO_x/Pt diodes were fabricated as reference devices to the nitrogen-doped Pt/TiO_x-$NTiO_x$/Pt and Pt/TiO_x-$NAlO_x$/Pt diodes, as shown in Figure 4.1a-d. The TiO_x thickness in the Pt/TiO_x/Pt device was 60 nm. In the other devices, the TiO_x and nitrogen-doped TiO_x ($NTiO_x$) films were 30 nm thick and the AlO_x and nitrogen-doped AlO_x ($NAlO_x$) films were 5 nm thick, as measured by ellipsometry. A Pt/$NTiO_x$-$NAlO_x$/Al diode with thinner insulator layers (3 nm AlO_x, 7 nm $NTiO_x$) was also fabricated, as shown in Figure 4.1e. The diodes, which were fabricated on 3-inch silicon wafers, had an area of 100 μm^2, as defined by lithographic patterning of the Pt contacts, as shown in Figure 4.1f.

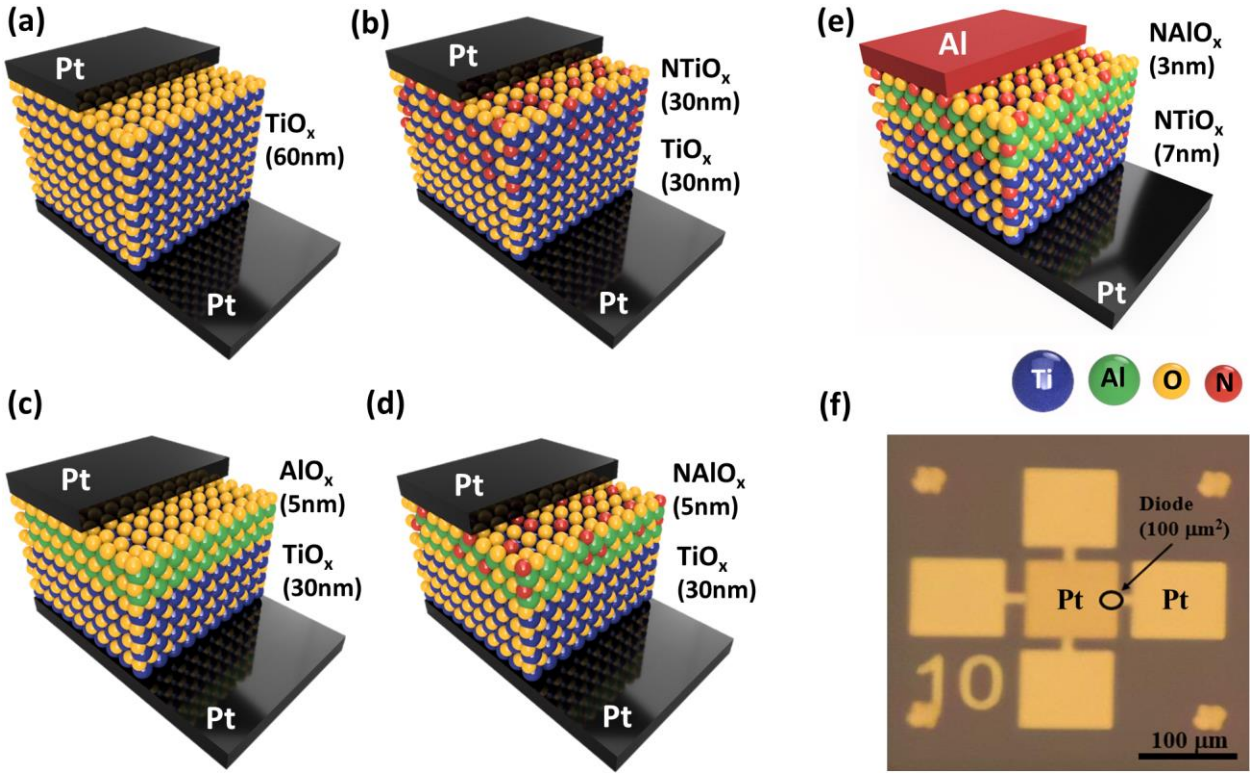

Figure 4.1. Device architecture of (a) Pt/TiO_x/Pt, (b) Pt/TiO_x-$NTiO_x$/Pt, (c) Pt/TiO_x-AlO_x/Pt, (d) Pt/TiO_x-$NAlO_x$/Pt, and (e) Pt/$NTiO_x$-$NAlO_x$/Al diodes. (f) A microscope image of fabricated MIIM diodes (labelled 10, which means 10 μm×10 μm). Materials are represented by blue (Ti), green (Al), yellow (O), and red (N) spheres.

All insulator films were deposited by PEALD. A nitrogen plasma technique, previously reported in Ref[57], was used to deposit the nitrogen doped TiO_x[57]. A similar nitrogen plasma technique for doping the AlO_x was developed in this study. Nitrogen-doped AlO_x has been produced previously via thermal atomic layer deposition (ALD) with ammonia water[58] and by PAALD with ammonia as the nitrogen source[59,60]. In this work, nitrogen plasma is used as the nitrogen source for doping the AlO_x in a remote PEALD system. Doping AlO_x with nitrogen requires high energy because the breaking of Al–O bonds by nitrogen atoms is not thermodynamically favored. No O_2 precursor sources are used but applied a pure nitrogen

plasma so that the formation of Al–O bonds is inhibited, allowing the nitrogen an opportunity to react with aluminum. Residual water vapor in the PEALD chamber was an oxygen source, and TMA was selected as the aluminum precursor because it is highly reactive with water vapor. Even though there is very little water vapor in the chamber compared to nitrogen, its affinity for the Al precursor is much greater, which is anticipated to ensure the formation of nitrogen-doped AlO_x in this arrangement. To deposit undoped TiO_x and AlO_x, the nitrogen plasma was replaced with an oxygen plasma. 1400 cycles of undoped TiO_x (60 nm thick) were deposited for $Pt/TiO_x/Pt$ diode at 250℃ with a base pressure below 1.33×10^{-4} Pa. In this process, three precursors are used: titanium (IV) isopropoxide (TIIP), O_2/N_2, and Ar as the inert gas. The vacuum chamber was first purged with Ar for 3 min to stabilize the chamber pressure and temperature. TIIP bubbled with argon was used to dose the substrate for 2 s at a pressure of 10.6 Pa, and the precursor line was then purged with Ar for 3 s at a pressure of 2 Pa. For undoped TiO_x films, a flow of O_2 was then stabilized for 500 ms before generating a plasma via radio frequency (RF) with a power of 300 W at a pressure of 2 Pa. The substrate was exposed to the O_2 plasma for 3 s and then purged with Ar for 2 s at a pressure of 10.6 Pa.

A similar process was used to fabricate the Pt/TiO_x-$NTiO_x/Pt$ diodes. 700 PEALD cycles were used to deposit the TiO_x (30nm thick). For the N-doped TiO_x, 810 cycles were employed to deposit a thickness of 30 nm and 190 cycles to deposit a thickness of 7 nm for $Pt/NTiO_x$-$NAlO_x/Al$. N_2 plasma was used, and the only sources of oxygen were the TIIP and residual water vapor in the vacuum chamber in a pressure range of 1.3×10^{-4} to 1.3×10^{-5} Pa. The N_2 plasma flow

was stabilized for 500 ms, and RF plasma was generated with a power of 300 W. The substrates were exposed at a pressure of 2 Pa for 3s, followed by Ar purging for 2 s at a pressure of 10.6 Pa.

For Pt/TiO_x-AlO_x/Pt diodes, the 30 nm TiO_x layers were deposited with the same process as detailed above. To deposit AlO_x, trimethylaluminum (TMA) and O_2 plasma precursors were employed, and 40 cycles were used to deposit a 5 nm thick film. The film was deposited at 300℃. TMA bubbled with argon was used to dose the substrate for 20 ms at a pressure of 2 Pa, and the precursor line was then purged with Ar for 1 s at a pressure of 2 Pa. A flow of O_2 was then stabilized for 500 ms before generating a plasma by RF with a power of 300 W at a pressure of 2 Pa, following which the substrate was exposed to the O_2 plasma for 2 s and then purged with Ar for 1s at a pressure of 2 Pa.

A similar process was used for the Pt/TiO_x-$NAlO_x$/Pt diodes. To deposit the $NAlO_x$ film, TMA and N_2 plasma precursors were employed, and 55 cycles were used to deposit a 5 nm thick film and 35 cycles to deposit a thickness of 3 nm for Pt/$NTiO_x$-$NAlO_x$/Al, again at 300℃. TMA bubbled with argon was used to dose the substrate for 20 ms at a pressure of 2 Pa, and the precursor line was then purged with Ar for 1 s at a pressure of 2 Pa. N_2 plasma was used, and the only source of oxygen was the residual water vapor in the vacuum chamber in a pressure range of 1.3×10^{-4} to 1.3×10^{-5} Pa. The N_2 plasma flow was stabilized for 500 ms, and an RF plasma was generated with a power of 300 W. The substrates were exposed at a pressure of 2 Pa for 5s, followed by Ar purging for 1s at a pressure of 2 Pa.

4.3 Results and discussion

UV-vis absorption and photoelectron spectroscopy measurements confirmed the deposition of nitrogen-doped AlO_x using this nitrogen-plasma PEALD approach. The normalized absorbance calculated from UV-vis transmittance and reflectance measurements of the AlO_x and $NAlO_x$ films are shown in Figure 4.2a. An absorbance edge is observed at 210 nm for AlO_x films (0s N_2 plasma) similar to reported previously[61]. An increasing shift in the absorbance edge is observed as the nitrogen plasma exposure was increased. The absorbance edges shift to 225 nm for the second procedure (3s N_2 plasma), 270 nm for the third procedure (5s N_2 plasma). A reduced bandgap from 6.2 to 5.4 eV is clearly observed in Figure 2b and is consistent with previous report that showed the bandgap of 6.2 eV for Al_2O_3[62]. This band gap reduction is attributed to the incorporation of N2p states in the band gap of AlO_x[63]. A similar shift in the bandgap of $NTiO_x$ was reported previously for the employed PEALD recipe[57]. X-ray photoelectron spectroscopy (XPS) was performed to study the valence band position for the AlO_x, $NAlO_x$, TiO_x, and $NTiO_x$ (Figure 4.3a-d). The results showed a shifting in the AlO_x valence band maximum from 2.7 eV (relative to the initial fermi level E_{Fi}) to 1.9 eV after nitrogen doping, consistent with the presence of N2p states above the valence band. The TiO_x showed upward and downward shifts in the valence and conduction bands, respectively, with nitrogen doping.

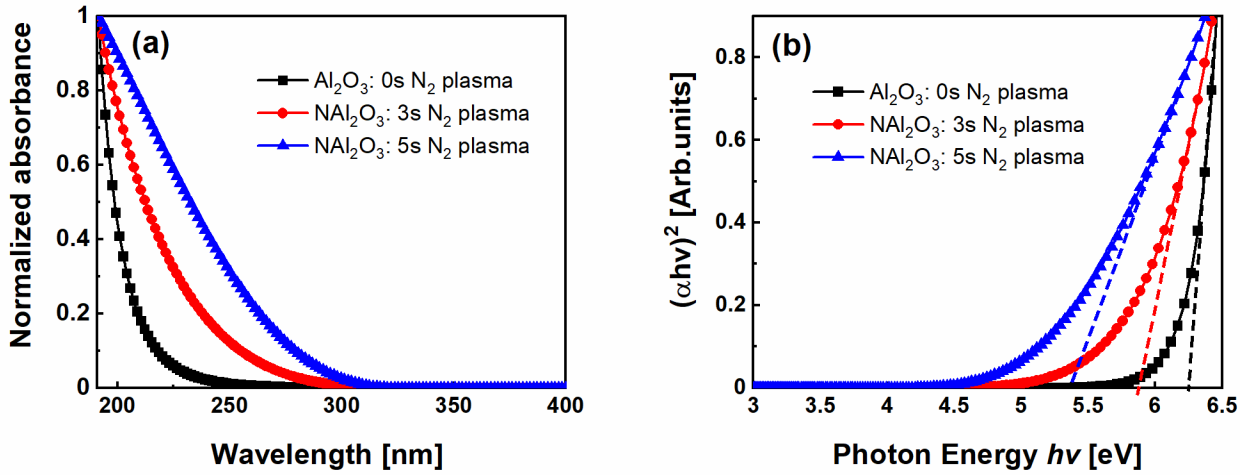

Figure 4.2. (a) Normalized absorbance and (b) Tauc plots of AlO_x and $NAlO_x$ films.

XPS was also used to clarify the chemical composition, bonding, and introduction of defects in the AlO_x and $NAlO_x$ films. The XPS spectra are shown in Figure 4.3e,f and the chemical compositions are included in Table 4.1. Deconvolution of the O1s peaks by Gaussian fitting in Figure 4.3e and f reveals peaks at 530.5 and 532 eV, which correspond to the O^{2-} in AlO_x and hydroxyl OH^- groups[15,64,65]. Compared to the AlO_x film, a much larger contribution from the OH^- peak is seen in the $NAlO_x$ film, similar to what was observed previously for the $NTiO_x$ deposited in this manner[57]. Other reported works have observed similarly large OH^- signals when measuring the surface of AlO_x, consistent with that observed here[66,67]. The N1s peaks in Figure 4.3f confirm that nitrogen is incorporated into the $NAlO_x$ films with an atomic percentage of 11.5%. The peaks at 398 eV and 400 eV are attributed to N-Al and N-N bonds, respectively.

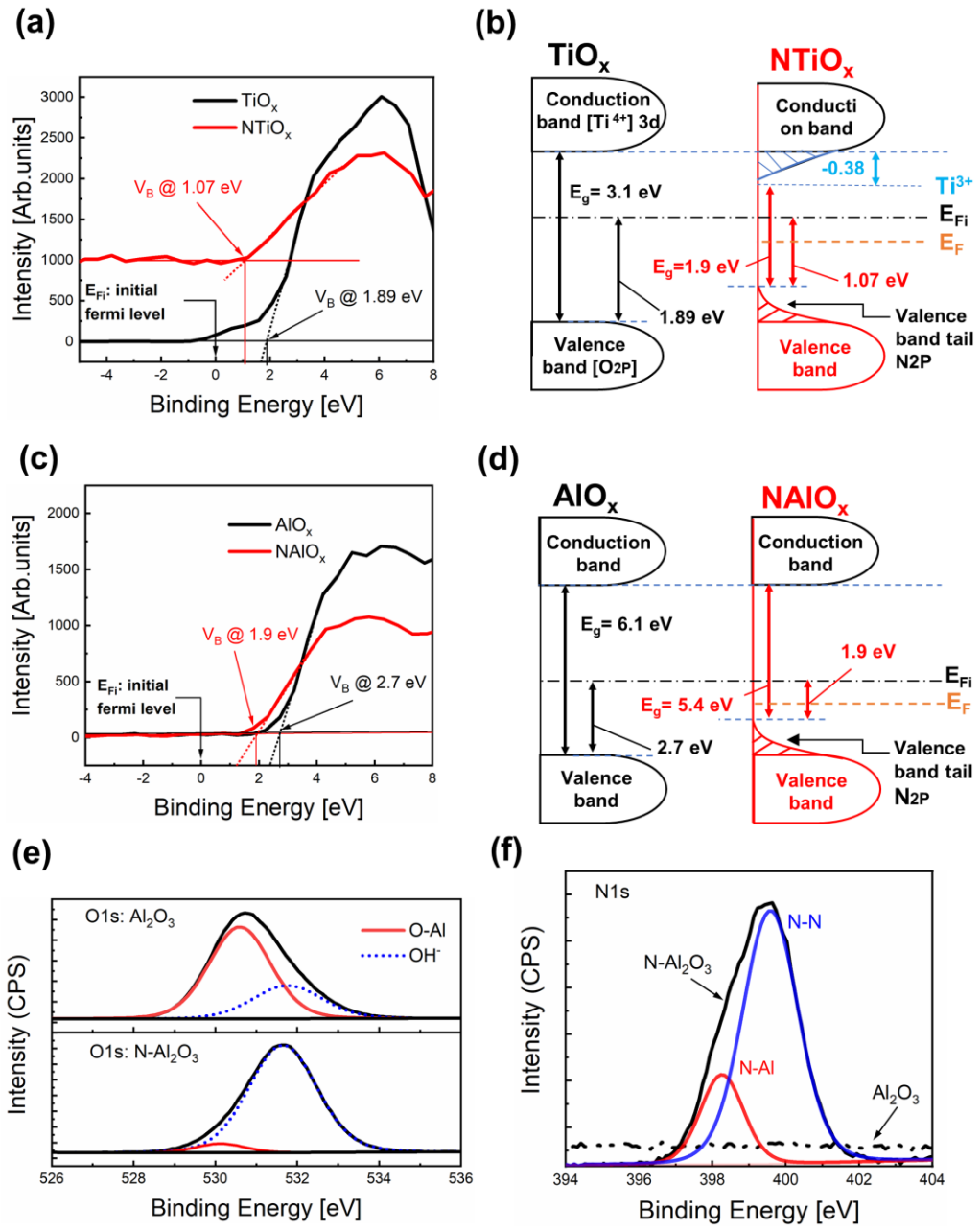

Figure 4.3. (a) XPS valence band spectra of TiO_x and $NTiO_x$ films. The binding energy at 0 eV is attributed to the initial fermi level. The valence band edge is measured by linear extrapolation of the curves. (b) Schematic diagrams of the density of states of TiO_x and $NTiO_x$. The bandgaps (E_g) were measured by UV-vis spectroscopy. (c) XPS valence band spectra of AlO_x and $NAlO_x$ films. (d) Schematic diagram of the density of states of AlO_x and $NAlO_x$. E_{Fi} is the initial fermi level, E_F indicates a modified fermi level after doping. XPS spectra of (e) O1s: AlO_x and NAlOx. (f) N1s: AlO_x and $NAlO_x$ films.

Table 4.1. Film compositions of deposited films.

Film	Film compositions (at. %)				
	Ti	O	N	C	Al
TiO_x[57]	24	55	-	21	-
$NTiO_x$[57]	13.1	26	23	37.8	-
AlO_x	-	48.5	-	12	39.5
$NAlO_x$	-	39.5	11.5	29.3	19.2

The introduction of defects into the films is expected to result in the formation of trap states within the bandgap of the materials. In addition to the aforementioned incorporation of N2p states in the band gap of $NAlO_x$, it has been shown that the OH^- groups observed in Figure 4.2d can serve as deep electron traps in $NAlO_x$[15,64]. In the $NTiO_x$ films, peaks at 457 eV and 463 eV were previously observed in the Ti 2p XPS spectra and attributed to Ti^{3+} (Ti_2O_3) defect states, and a Ti-OH^- peak was observed at 531 eV[57]. Both Ti^{3+} and OH^- have been reported to act as shallow electron traps below the conduction band[68–70]. Deep electron traps close to the valence band in $NTiO_x$ include N2p states[70] (see Figure 4.3). Electrons are not expected to be thermally excited from these deep trap states, but trapped electrons can result in the formation of space charge layers (dipole layers) at the insulator interfaces. Excess nitrogen at the interfaces would be expected to attract electrons due to the high electronegativity of nitrogen, resulting in the formation of dipole layers[71,72].

In Figure 4.4a,d the expected energy levels for the undoped TiO_x and AlO_x insulators are illustrated. The nitrogen dopant is expected to generate N2p states above the valence band[63] and

shift the Fermi level (E_F) downward for $NTiO_x$ and $NAlO_x$, as shown in Figure 4.4b and e. Thus, when the layers are joined, larger barriers are expected at the TiO_x-$NTiO_x$ and TiO_x-$NAlO_x$ interfaces, as shown in Figure 4.4c and f, respectively. The defects formed in the oxide films through doping and the stacking of insulators with different dielectric constants (e.g., TiO_x-$NAlO_x$) can result in the formation of traps and a dipole layer at the interface between the doped and undoped layer, as previously reported[73,74]. Increasing this barrier height or incorporating a dipole can prevent electrons from tunneling in the reverse direction, i.e., from left to right, as shown in Figure 4.4. The electric field at the interface is also expected to favor electron tunneling in the forward direction (right to left) for the doped diodes. In the next section, the diode performance is characterized and the conduction mechanisms are investigated to clarify how the diodes are affected by the presence of an interfacial barrier and defect states.

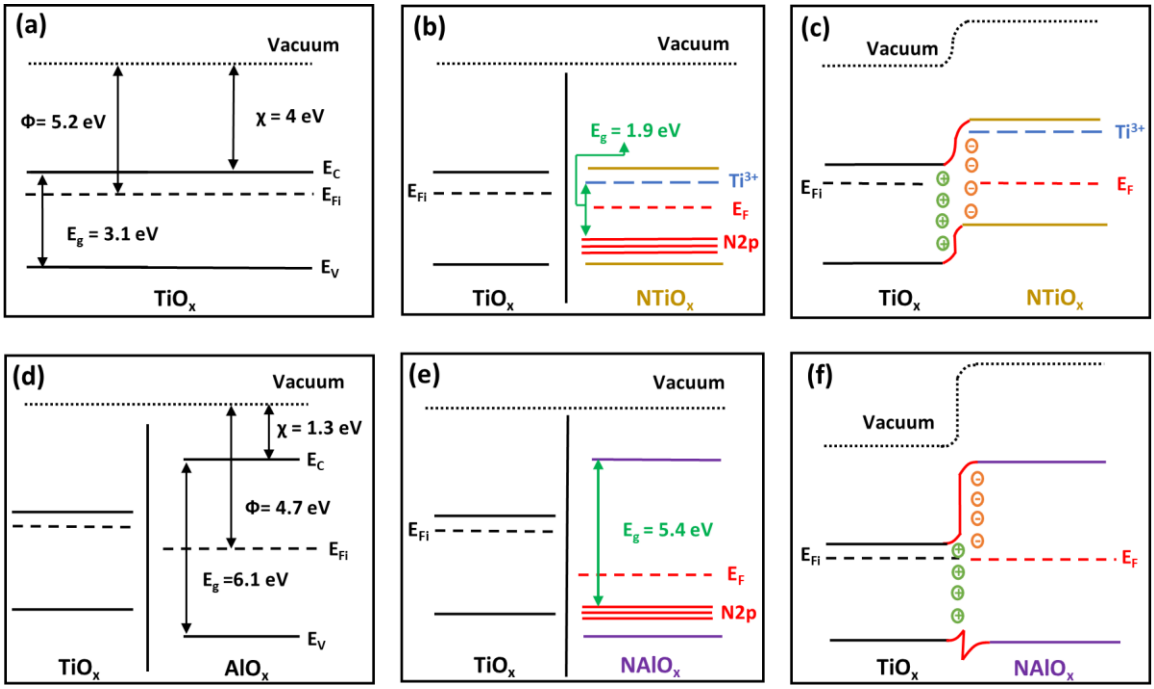

Figure 4.4. (a) Energy level diagram for undoped TiO_x-TiO_x interface, (b) N2p state formation for $NTiO_x$ and downward shifting of E_F results in a mismatch in Fermi levels, (c) equilibrium state and barrier formation between TiO_x and $NTiO_x$, (d) energy level diagram for undoped TiO_x-AlO_x interface, (e) N2p state formation for $NAlO_x$ and downward shifting of E_F results in a greater mismatch in Fermi levels, (f) equilibrium state and increased barrier height between TiO_x and $NAlO_x$. E_{Fi} and E_F indicate an initial fermi level and a fermi level after doping, respectively.

4.3.1 Diode performance

The current-voltage (*I*–*V*) characteristics of the undoped and N-doped diodes were measured over a range of −1 to +1 V, with the exception of the undoped TiO_x diode, which was measured from -2 to +2 V in order to observe its turn on voltage. The rectification performance of the MIIM diodes is characterized by three figures of merit (asymmetry, nonlinearity, and responsivity), listed in Table 2.1 in Chapter 2, which are affected by several factors, including metal and insulator selection, insulator thickness, and barrier heights at the interfaces.

Interpolation fitting was used to obtain the figures of merit from the *I-V* data. Data intervals of 0.01V were used to minimize any interpolation errors that could affect the figures of merit. Both exponential fitting, as used by Pelz *et al*.[75], and polynomial fitting were also tested as methods to obtain the figures of merit, as shown in Figures 10.1 and 10.2 in Chapter 10. For our data, the exponential fitting was inferior (R^2=0.992) while the polynomial method showed poor fitting at negative voltage bias.

I. Performance of diodes with thick insulator layers

Figure 4.5 shows the *I-V* measurements of representative undoped Pt/TiO_x/Pt and N-doped Pt/TiO_x-$NTiO_x$/Pt diodes. Figure 4.5a shows that the current density reaches 3.5 A/cm^2 for the undoped TiO_x diode while it reaches 1618 A/cm^2 for the N-doped diode at +1V. The asymmetry is 28.6 for the N-doped TiO_x diode and 0.4 for the undoped TiO_x diode at +0.5 V, as shown in Figure 4.5b. The current is observed to increase significantly in Figure 4.5a as the voltage increases, which is expected to coincide with the position of the turn on voltage (TOV) and the region of maximum nonlinearity[15]. TOVs of 1.6 and 0.5 V were determined for the undoped TiO_x and $NTiO_x$ diodes by the extrapolation in the linear region (ELR) method[6,76]. The nonlinearity is shown in Figure 4.5c. At a low applied voltage, the nonlinearity shows a slight improvement for the N-doped TiO_x diode compared to the undoped TiO_x diode. The nonlinearity at 0 V is approximately 3 for the doped diode and 3.5 for the undoped diode. The zero-bias responsivities are 0.1 A/W for the undoped TiO_x diode and 13.5 A/W for the N-doped diode at zero bias, as shown in Figure 4.5d. The differential zero-bias resistances are 5×10^6 Ω for the undoped TiO_x diode and 2.8×10^4 Ω for the N-doped diode, as shown in Figure 4.5e. Hence N-

doping of the TiO_x simultaneously improves the figures of merit and reduces the resistance of the diode.

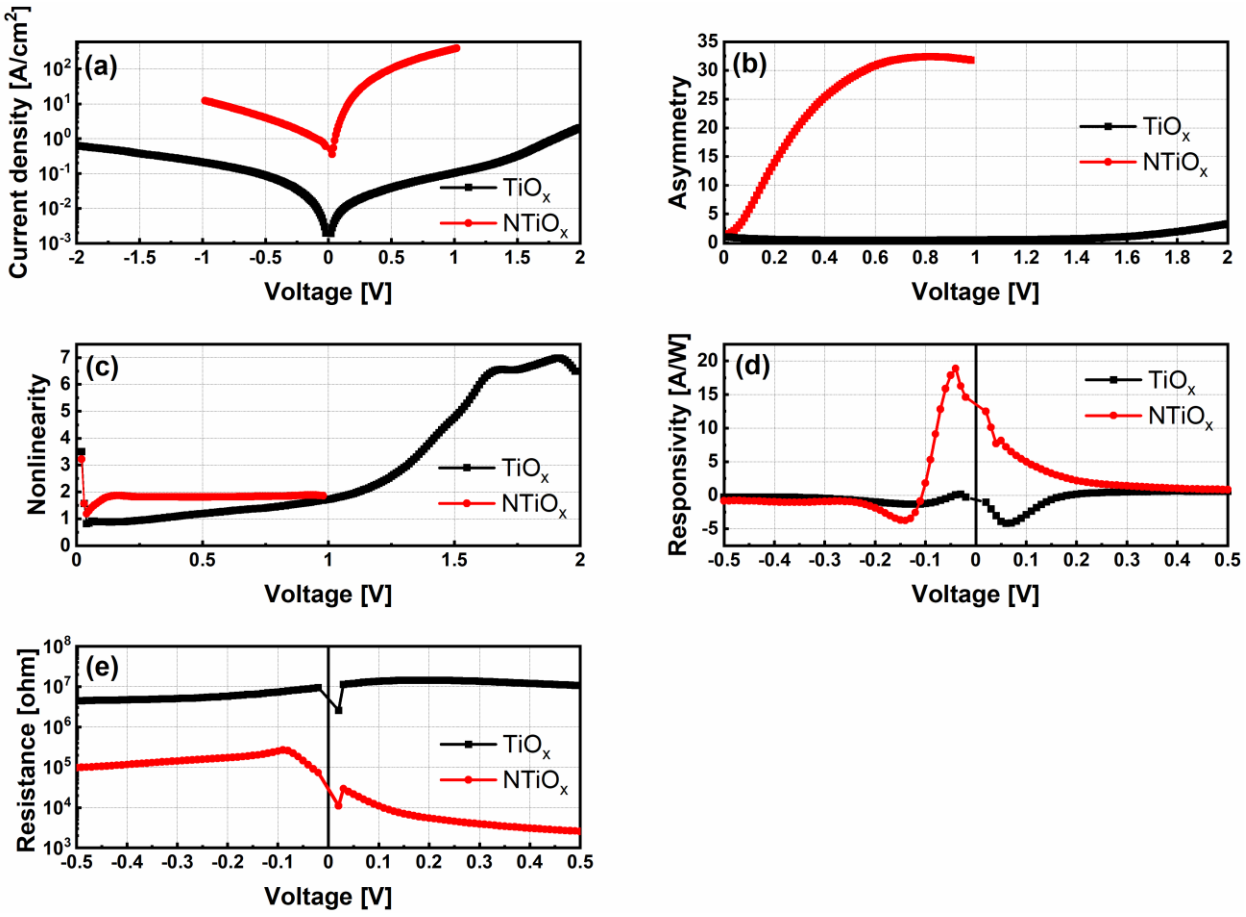

Figure 4.5. Performance of typical Pt/TiO_x/Pt and Pt/TiO_x-$NTiO_x$/Pt diodes. (a) Current density vs. voltage, (b) asymmetry, (c) nonlinearity, (d) responsivity, and (e) differential resistance of the diodes.

The improved performance of the $NTiO_x$ diode may result from the presence of defects in the insulator and different conduction mechanisms[74]. The conduction current in the insulating layers of MIM diodes may be electrode-limited or bulk-limited. Electrode-limited conduction mechanisms depend on the metal-insulator interface. Thus, the potential barrier height at the

interface, which is an important parameter, can be affected by material selection and fabrication methods. Electrode-limited conduction mechanisms include SE, FNT, DT. Bulk-limited conduction mechanisms depend on the electrical properties of the insulator. Thus, the deposition method or the addition of impurities to create defects (electron traps) can tune the film properties and the extent of bulk-limited conduction. These mechanisms include PF and TAT.

To understand the superior performance of the $NTiO_x$ diode, the equations for the different conduction mechanisms were fitted to the *I–V* data. Plots with $R^2 > 0.999$ are considered to be highly linear and representative of the dominant conduction mechanism. Figure 4.6a shows the summary of dominant conduction mechanisms across the voltage range for the undoped TiO_x diode. In the Pt/TiO_x/Pt device, the relatively thick (60 nm) TiO_x layer inhibits tunneling mechanisms. Schottky emission is dominant for most voltages, as shown in the highly linear ($R^2 = 0.999$) SE plots in Figure 4.6b. This is consistent with the formation of a Schottky barrier at the Pt/TiO_x interface[77]. The dominance of SE in both the forward and reverse directions results in a low asymmetry ratio of 5, as seen in Figure 4.5b. A transition from SE to FNT occurs at larger voltages (TOV = 1.6 V), as shown in the FNT plots in Figure 4.5c. In FNT, applying a large electric field enables electrons to tunnel a shorter distance through the triangular portion of the potential barrier. The Pt/TiO_x-$NTiO_x$/Pt diode shows markedly different conduction mechanisms in Figure 4.6d. PF emission is dominant at most forward voltages (0.1 V to 0.81 V), as indicated by the linear fit of the PF plot in Figure 4.6e. The appearance of a trap-mediated conduction mechanism (PF) clearly indicates that the introduction of defects into the $NTiO_x$ alters the diode behavior. It is expected that PF is dominant in this device because nitrogen doping introduces bulk traps into the $NTiO_x$ layer, such as the Ti^{3+} and OH^- observed in

the Ti2p and O1s XPS peaks[57], which can act as electron traps to facilitate PF conduction. The dominance of PF conduction at forward biases suggests that the $NTiO_x$ layer is thick enough (30 nm) to eliminate or minimize direct tunneling or TAT, and that the thermal energy is sufficient to excite electrons from traps to the conduction band. At reverse bias in the Pt/TiO_x-$NTiO_x$/Pt diode, SE remains the dominant mechanism, as seen in Figure 4.6f, consistent with the fact that the Pt/TiO_x junction remains unchanged.

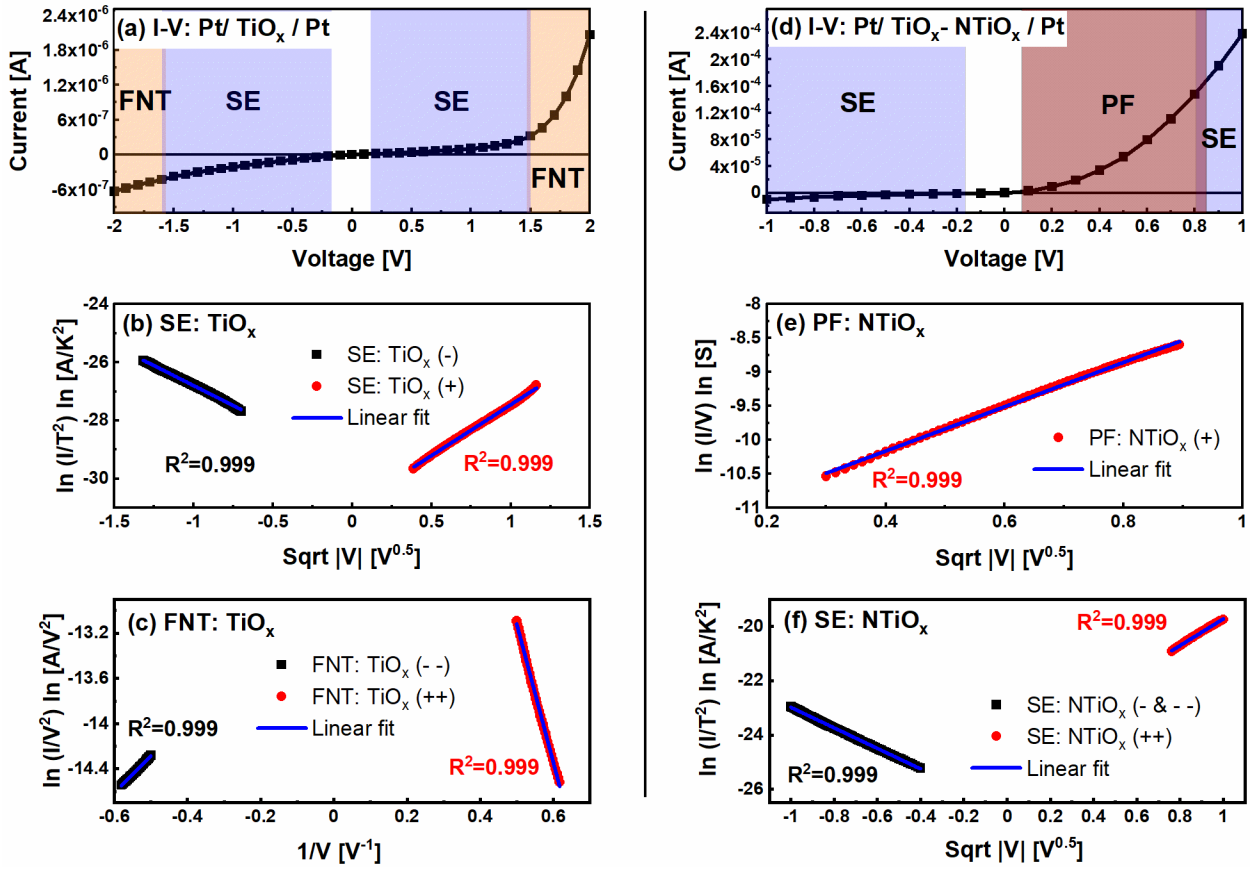

Figure 4.6. (a) I-V curve and dominant conduction mechanisms of Pt/TiO_x/Pt diode, (b) Schottky emission fitting of TiO_x diode, (c) Fowler–Nordheim tunneling fitting for TiO_x diode, (d) I-V curve and dominant conduction mechanisms of Pt/TiO_x-$NTiO_x$/Pt diode, (e) Poole-Frenkel fitting for $NTiO_x$ diode, (f) Schottky emission fitting of $NTiO_x$ diode. Black squares and red circles represent negative and positive polarities, respectively. Plots with $R^2 >$ 0.999 are considered to be highly linear and representative of the dominant conduction mechanism.

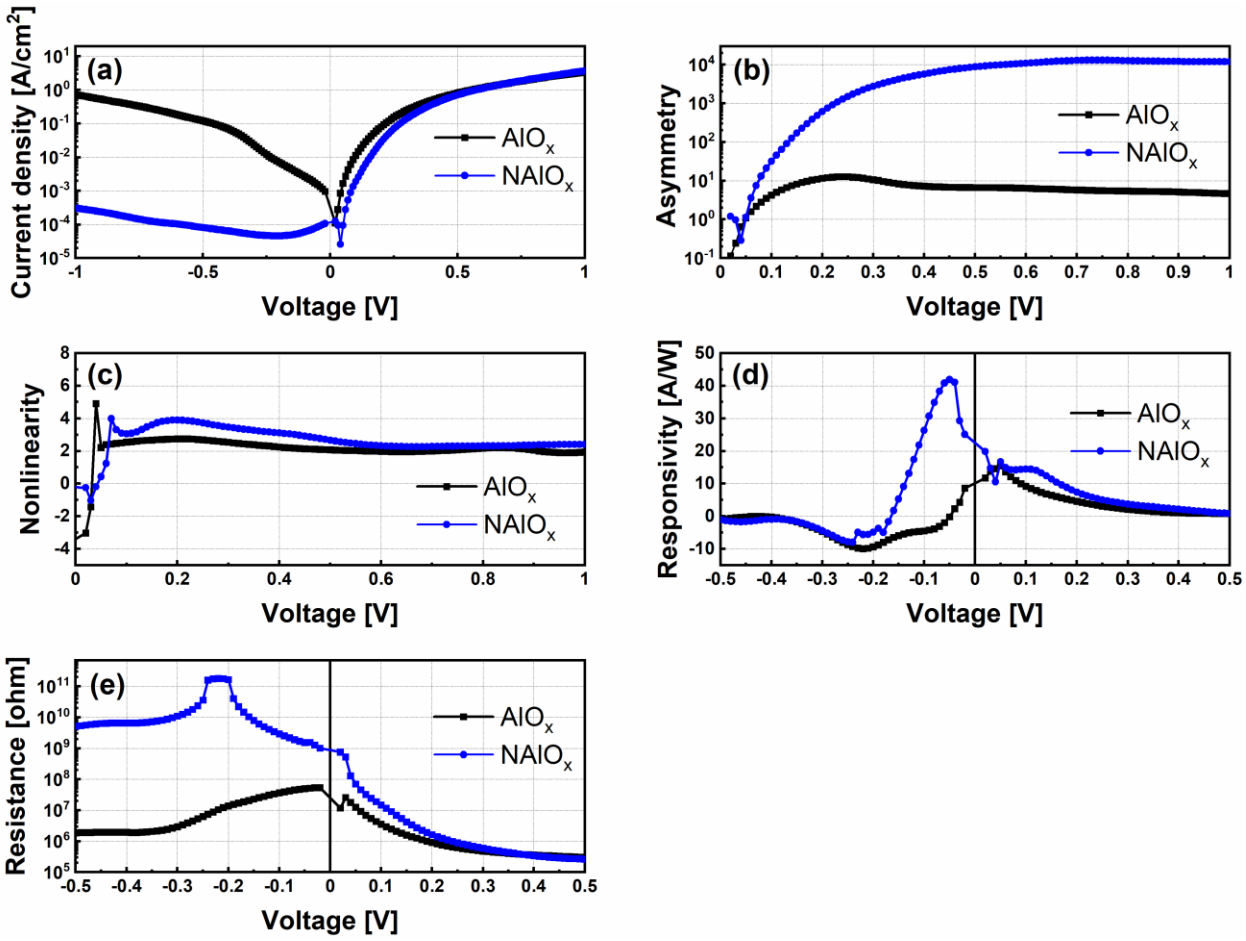

Figure 4.7. Performance of typical Pt/TiO_x-AlO_x/Pt and Pt/TiO_x-$NAlO_x$/Pt diodes. (a) Current density vs. voltage, (b) asymmetry, (c) nonlinearity, (d) responsivity, and (e) differential resistance of the diodes.

Figure 4.7 shows the *I-V* data and figures of merit for representative Pt/TiO_x-AlO_x/Pt and Pt/TiO_x-$NAlO_x$/Pt diodes. Figure 4.7a shows that the current density reaches 3.3 A/cm^2 for the AlO_x diode and 3.6 A/cm^2 for the $NAlO_x$ diode at +1 V. The asymmetry is 6.6 for the AlO_x diode and 8.76×10^3 for the $NAlO_x$ diode at +0.5 V, as shown in Figure 4.7b. TOVs of 0.46 and 0.45 V were determined for the undoped AlO_x and $NAlO_x$ diodes. The max nonlinearity is 5 and 4 for the AlO_x and $NAlO_x$ diodes, respectively, as shown in Figure 4.7c. The zero-bias

responsivities are 10 A/W for the AlO_x diode and 22.3 A/W for the $NAlO_x$ diode, as shown in Figure 4.7d. Finally, the differential zero-bias resistances of the AlO_x and $NAlO_x$ diodes are 2.5×10^7 Ω and 83×10^7 Ω, respectively, as shown in Figure 4.7e.

The median zero-bias resistance was calculated as in Ref.[39] for 21 Pt/TiO_x-AlO_x/Pt diodes and 21 Pt/TiO_x-$NAlO_x$/Pt diodes. The median zero-bias resistance was 9.8×10^6 Ω for the $NAlO_x$ diodes, which was slightly higher than 4.0×10^6 Ω for the undoped AlO_x diodes. Both the AlO_x and $NAlO_x$ diodes showed a median current density of 3 A/cm^2. For comparison, the zero-bias resistances of previously reported diodes were normalized to a contact area of 100 μm^2 and are summarized in Table 2.2 in Chapter 2. The resistances of the diodes produced in this work are comparable to many of the previous diodes in Table 2.2, despite the thicker insulator layers used here.

The figures of merit for 21 Pt/TiO_x-$NAlO_x$/Pt diodes are included in Figure 4.8. The highest current density observed was 15 A/cm^2 at +1 V, the highest asymmetry was 1.85×10^4 at +0.7 V, the highest nonlinearity was 15.8 at +0.1 V, and the highest zero-bias responsivity was 36.8 A/W. Notably, the zero-bias responsivity was >10 A/W for all 21 of the diodes. To our knowledge, many of the zero-bias responsivities observed here are more than triple the highest value previously reported for a MIM diode. Moreover, this is the first time that a zero-bias responsivity exceeding the 0.5(q/kT) =19.4 A/W theoretical responsivity limit for Schottky diodes (at 300 K) has been demonstrated in a MIM diode.

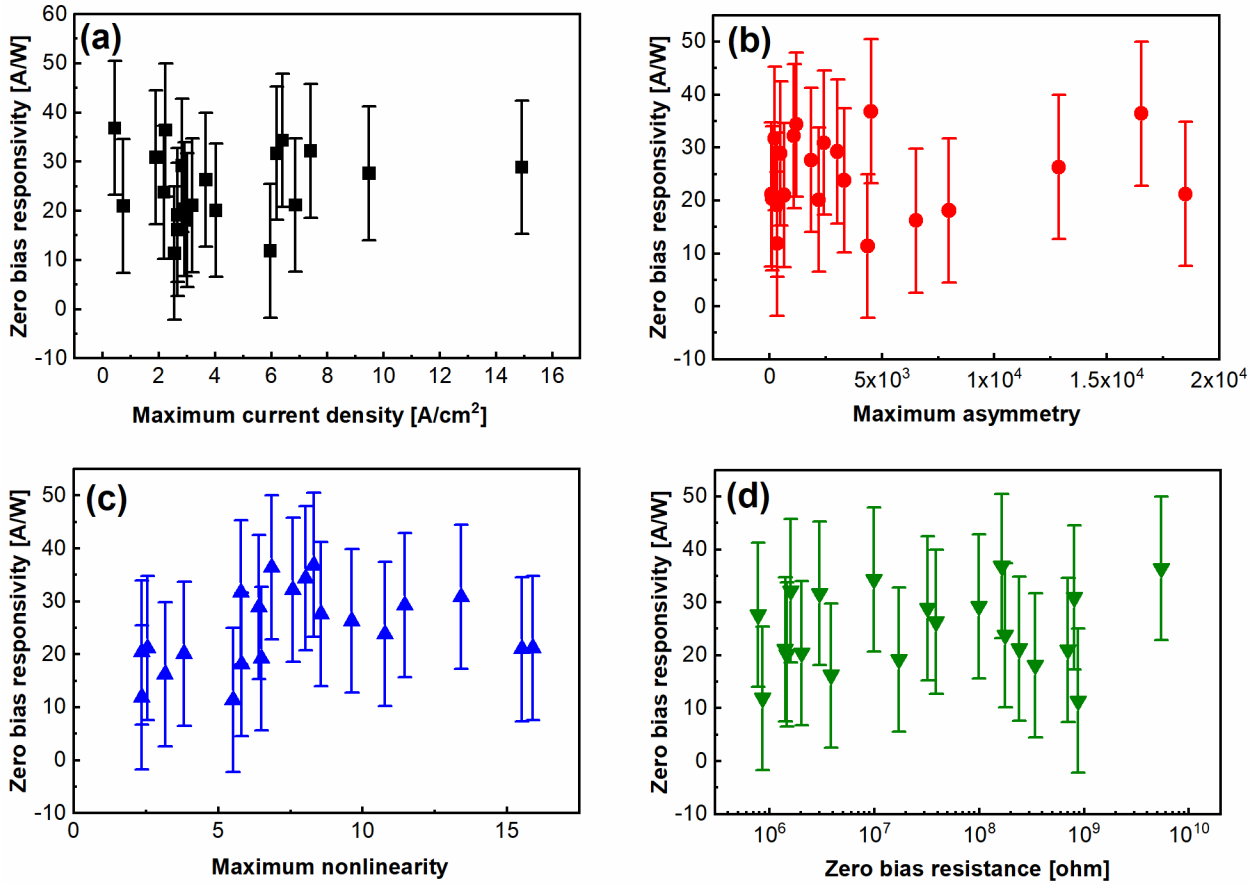

Figure 4.8. Scatter measurements of the figures of merit for 21 Pt/TiO_x-$NAlO_x$/Pt diodes on a single substrate. (a) The maximum current density at +1V bias, (b) maximum asymmetry, (c) maximum nonlinearity, and (d) zero-bias resistance versus the zero-bias responsivity of the diodes

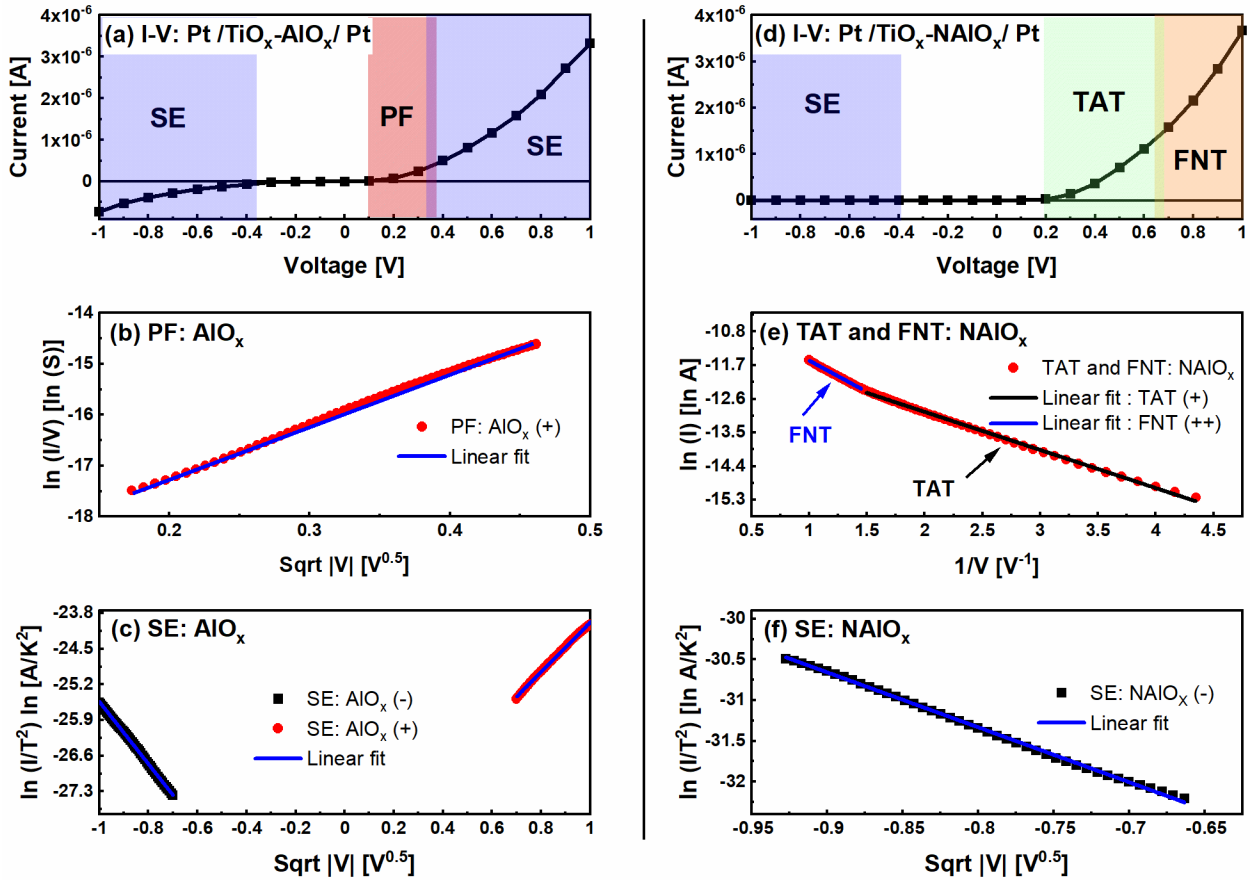

Figure 4.9. (a) I-V curve and dominant conduction mechanisms of Pt/TiO_x-AlO_x/Pt diode, (b) Poole-Frenkel fitting for AlO_x diode, (c) Schottky emission fitting for AlO_x diode, (d) I-V curve and dominant conduction mechanisms of Pt/TiO_x-$NAlO_x$/Pt diode, (e) trap-assisted tunneling and Fowler-Nordheim-like tunneling fitting for $NAlO_x$ diode, and (f) Schottky emission fitting for $NAlO_x$ diode.

Figure 4.9a and d show the dominant conduction mechanisms across the voltage range for the AlO_x and $NAlO_x$ diodes from Figure 4.7. Figure 4.9b shows that the *I–V* data for the undoped AlO_x diode in the range of 0.16 V to 0.4 V is well-fitted (R^2 = 0.999) by the PF equation (Equation 2.3), which corresponds to electron transport via shallow traps. Figure 4.9c indicates that SE is the dominant conduction mechanism for higher voltages of 0.4 V to 1 V. The SE mechanism has been observed previously at a Pt/AlO_x junction in Ref[15] and is the dominant

conduction mechanism at most forward and reverse voltages in the Pt/TiO_x-AlO_x/Pt diode. The Pt/TiO_x-$NAlO_x$/Pt diode shows an excellent fit (R^2 = 0.999) for the TAT relation at forward biases of 0.2 V to 0.7 V in Figure 4.9e. TAT conduction occurs when electrons use intermediate traps to assist the tunneling. The electrons do not need to cross the entire barrier, thus this mechanism is important at zero or near-zero bias[78]. The TAT conduction mechanism results in a slightly smaller current density in the 0.2 V to 0.7 V range compared to the PF and SE conduction mechanisms in the Pt/TiO_x-AlO_x/Pt diode, as shown in Figure 4.7a, which is attributed to trapping of electrons by the deep traps in the $NAlO_x$ film, from which the electrons cannot be efficiently de-trapped at small bias voltages. Figure 4.9e shows that, at higher voltages, the conduction mechanism changes from TAT to FNT-like tunneling where the electron can tunnel through the barrier from a trap state, as observed previously in Refs.[21,73,79,80]. The voltage is sufficiently high that the required tunneling width is reduced and can occur without the assistance of traps[81]. As shown in Figure 4.9f, SE is still the dominant conduction mechanism in reverse bias as the Pt/TiO_x junction remains unchanged.

The presence of differing conduction mechanisms in the undoped Pt/TiO_x-AlO_x/Pt MIIM diode at low forward (PF) and reverse (SE) biases results in asymmetric conduction and better figures of merit, as compared to the Pt/TiO_x/Pt diode. Even greater improvements in the figures of merit were observed for the N-doped Pt/TiO_x-$NAlO_x$/Pt devices with high asymmetry, nonlinearity, and responsivity at low voltage bias, which was attributed to the appearance of TAT and FNT for the forward voltage range of 0.2 V to 1 V.

The operation of the Pt/TiO_x-$NTiO_x$/Pt diode is summarized in Figure 4.10a-c. Figure 4.10a shows the unbiased diode, Figure 4.10b shows SE conduction under reverse bias, and

Figure 4.10c shows the PF conduction under forward bias, which is facilitated by the electron traps introduced by N-doping. The differing conduction mechanisms in the forward and reverse directions result in an enhanced asymmetry, as seen in Figure 4.5b, while the introduction of PF conduction results in a larger current density and lower zero-bias resistance, as seen in Figure 4.5a and e, respectively. The operation of the Pt/TiO_x-$NAlO_x$/Pt diode that demonstrates a record zero-bias responsivity is summarized in Figure 4.10d-f. Figure 4.10d shows the unbiased diode with the expected band bending and dipole layer between the different insulators. Figure 4.10e shows SE conduction under reverse bias, where the current is limited by the large barrier presented by the $NAlO_x$, as well as the band bending and dipole layer. Figure 4.10f shows the TAT conduction under forward bias, which is facilitated by the electron traps introduced by N-doping. As noted in Figure 4.4, nitrogen doping is expected to introduce N2p states above the valence band. The results suggest that, for this diode, the distance from the Pt electrode to the trap sites is small enough for TAT to occur. A similar consideration was observed in Refs.[82–84], where the authors observed the dominance of TAT when the trap density is very high in HfO_x and close to the Pt/HfO_x interface. The thermal activation energy is likely insufficient to excite the electrons from these deep trap states to the conduction band of $NAlO_x$, explaining why the PF mechanism is not dominant. The differing conduction mechanisms in the forward and reverse directions results in an enhanced asymmetry, as seen in Figure 4.7b. Importantly, by facilitating a tunneling conduction mechanism in the forward direction, the *q/2kT* responsivity limit is surpassed.

It is clearly seen that the introduction of defect-mediated conduction mechanisms can eliminate the trade-off between resistance and responsivity that was previously observed in

MIIM diodes[85]. Figure 5d and e show that N-doping in the Pt/TiO_x-$NTiO_x$/Pt diode reduces the resistance and improves responsivity, as compared to the undoped Pt/TiO_x/Pt diode. The Pt/TiO_x-$NAlO_x$/Pt diode shows a significant improvement in the responsivity (from 10 to 22.3 A/W) in Figure 4.7d, while the median zero-bias resistance of these diodes increased only slightly compared to the undoped Pt/TiO_x-AlO_x/Pt diodes.

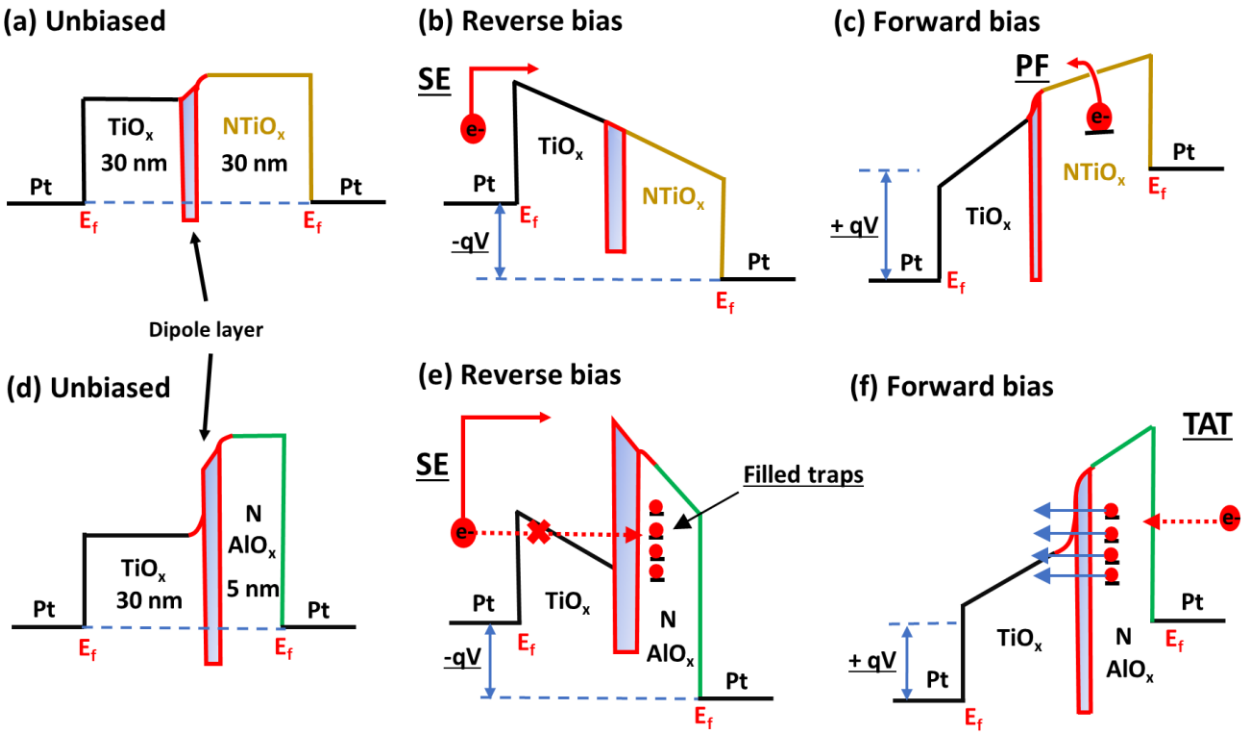

Figure 4.10. Dominant conduction mechanisms for Pt/TiO_x-$NTiO_x$/Pt and Pt/TiO_x-$NAlO_x$/Pt diodes when: (a), (d) unbiased, (b), (e) negatively biased, (c), (f) positively biased.

The effective barrier heights for the four metal/insulator interfaces (Pt/TiO_x, Pt/$NTiO_x$, Pt/AlO_x, Pt/$NAlO_x$) were examined above +2 V. Larger voltages were applied to induce Fowler-Nordheim tunneling, and the effective barriers were determined from the slopes of the FNT

plots[15,86] using the Equation 2.2. The effective electron mass in the oxide was taken as m_{ox}=0.2 m_0[87] for AlO_x and $NAlO_x$ and m_{ox}=6 m_0[88] for TiO_x and $NTiO_x$ films. The FNT plots are shown in Figure 4.11. A barrier of 2.6 eV was measured for the Pt/AlO_x interface in the Pt/TiO_x-AlO_x/Pt device, which was slightly reduced to 2.5 eV for Pt/$NAlO_x$. The Pt/TiO_x had an effective barrier of 1.9 eV, which was reduced to 1 eV for the Pt/$NTiO_x$. The clear reduction in effective barrier height for Pt/$NTiO_x$ may be due to the shift in the conduction band position of $NTiO_x$, as shown in Figure 4.3b for $NTiO_x$. The introduction of electric dipoles at the insulator/doped insulator interface can also lead to a reduction in the metal-insulator-doped insulator barrier height (Φ_{MII}). This can reduce the tunneling distance[89] through the undoped insulator, as shown in Figure 4.11, and enhance the tunneling probability. The smaller metal-insulator barrier heights are consistent with the increased current in the Pt/TiO_x-$NTiO_x$/Pt and Pt/TiO_x-$NAlO_x$/Pt diodes when FNT is dominant, as shown in Figure 4.12, and a previous report of barrier height reduction in nitrided oxide films[19].

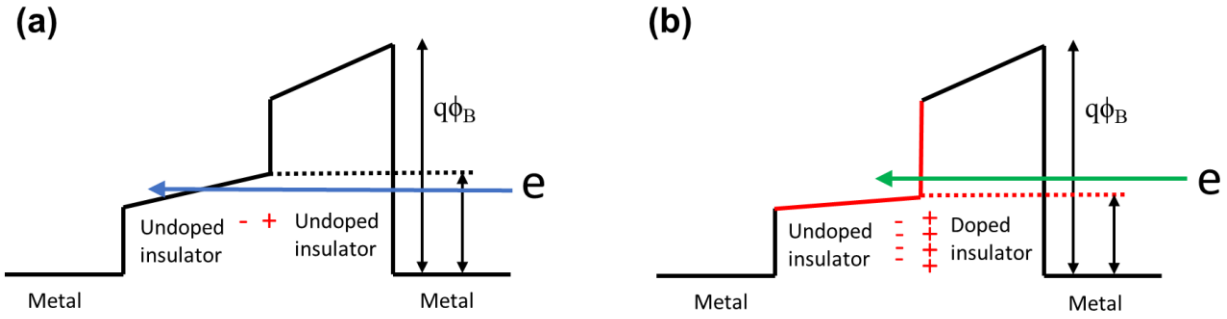

Figure 4.11. Band diagrams shows how interface charges at the insulator-insulator interface can affect the barrier hight Φ_{MII} and the tunneling distance. (a) Undoped diode (b) and doped diode with a larger interfacial dipole.

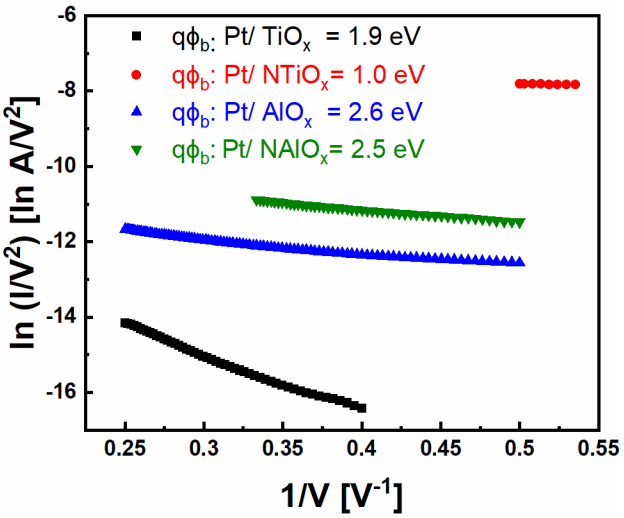

Figure 4.12. FNT plots at higher voltages for the Pt/TiO_x/Pt, Pt/TiO_x-$NTiO_x$/Pt, Pt/TiO_x-AlO_x/Pt, and Pt/TiO_x-$NAlO_x$/Pt diodes. Barrier heights are determined from the slopes of the plots.

II. Performance of diodes with thin insulators layers

Diodes for energy harvesting applications require a low resistance at low or zero bias voltages, ideally around 100 Ω to achieve efficient coupling with the antenna[75,90]. In order to demonstrate the applicability of the doped MIIM diodes produced in this work for energy harvesting applications, thinner doped Pt/$NTiO_x$-$NAlO_x$/Al diodes were fabricated, as shown in Figure 4.1e. Here, both the 7 nm $NTiO_x$ layer and 3 nm $NAlO_x$ layer were doped with nitrogen in an effort to introduce additional dipoles at the insulator/insulator and metal/insulator interfaces, as the presence of dipoles is expected to decrease the effective barrier height and increase the current[91]. The *I-V* data and figures of merit for a typical diode are shown in Figure 4.13. The asymmetry is 1, the nonlinearity reaches a value of 3.7, the zero-bias responsivity is 1.7 A/W, and a very low zero-bias resistance of 36 Ω is observed. These low-resistance diodes suffer from a low asymmetry of 1, however, the low resistance diodes are promising to operate at high

terahertz frequencies as reported previously[2,8,32,33,92]; by addressing other trade-offs, including resistance matching with the antenna, high nonlinearity at low bias, and a small RC time constant.

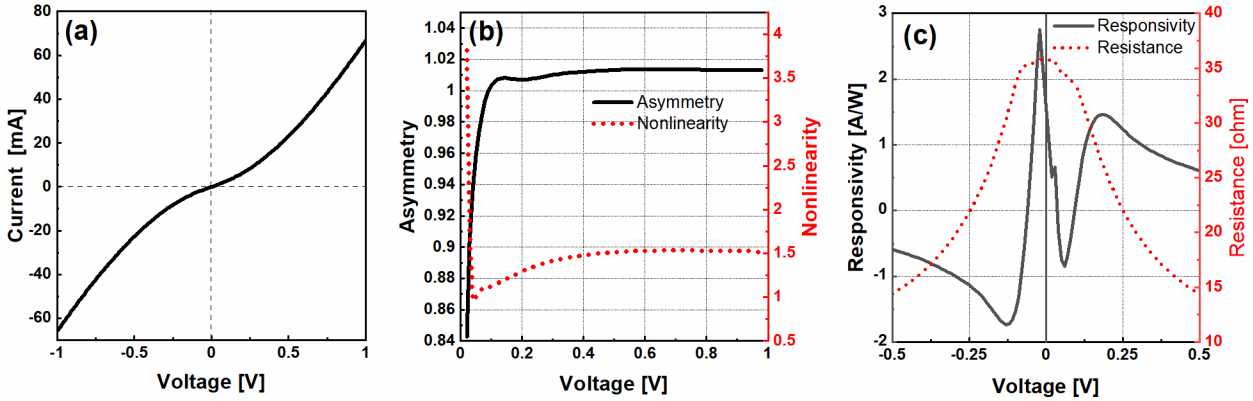

Figure 4.13. Performance of a typical Pt/$NTiO_x$-$NAlO_x$/Al diode with 7 nm and 3 nm $NTiO_x$ and $NAlO_x$ layers. (a) Current vs. voltage, (b) asymmetry and nonlinearity, (c) responsivity and differential resistance of the diodes.

4.3.2 Performance comparison

The N-doped $NTiO_x$ and $NAlO_x$ diodes produced here show significant improvements in the figures of merit compared with undoped double and quadra TiO_x-AlO_x diodes with the same contact area of 100 μm^2, as reported previously by Aydoying *et al.*[26] (fourth and fifth entries in Table 2.2 in Chapter 2). Asymmetry and current density are higher in the diodes produced here, even though, together with thicker insulators, the same metal (Pt) is used for both electrodes. The highest figures of merit at 0.5 V, as reported by Chin *et al.*[12] for Nb-NbO_2-Pt with an insulator thickness of 15 nm, are a current density of 10^{-2} A/cm^2, asymmetry of 7.74×10^3, nonlinearity of 4.7, and a zero-bias responsivity of 15 A/W. The Pt/TiO_x-$NAlO_x$/Pt diodes produced here

displayed superior figures of merit at +0.5 V or less with a larger current density of 0.7 A/cm^2 (and 3.6 A/cm^2 at +1V). The high asymmetry value of 8.76×10^3 for the Pt/TiO_x-NAlO_x/Pt diode is very encouraging, given that identical Pt contacts were used on both sides of the device (the asymmetry is expected to increase for metals with different work functions)[24]. Notably, the highest zero bias responsivity of 36.8 A/W that was observed in this work is, to our knowledge, the highest value reported to date for a MIM diode, and the first time that a MIM diode has outperformed the Schottky diode limit of 19.4 A/W.

A low diode resistance and capacitance are desired for high-frequency operation. The diode capacitance can be reduced by increasing the insulator thickness; however, this is expected to increase the diode resistance. This work suggests that doping strategies can facilitate the use of thicker insulator layers. The thick Pt/TiO_x-NTiO_x/Pt diodes had lower zero-bias resistances than the undoped Pt/TiO_x/Pt diodes and the thin Pt/NTiO_x-NAlO_x/Al diode showed a significantly lower resistance than diodes with undoped insulators, as shown in Table 2.2. Hence, doped MIIM diodes are promising for tackling the resistance-capacitance trade-off and for achieving high-frequency rectification.

Chapter 5
Quantum-Tunneling Metal-Insulator-Metal Diodes Made by Rapid Atmospheric Pressure Chemical Vapor Deposition

5.1 Overview

The growing "Internet of things (IoT)" is resulting in the integration of electronics, including electronics enabled by quantum-mechanical phenomena, into a wider variety of environments, such as plastics and textiles. This is stimulating the development of cost-effective, scalable techniques for manufacturing quantum devices. As discussed in Chapters 1 and 2, high-throughput fabrication of MIM diodes is limited by slow deposition rates, the need for a vacuum and high temperature, specific metal films for oxidation, and complex compound precursors, as well as challenges in reproducibility. To overcome these challenges, an AP-SALD system operated to produce AP-CVD conditions is utilized for the first time to fabricate Al_2O_3 insulating films for MIM diodes. The performance of the MIM diodes fabricated by AP-CVD is characterized and compared to MIM diodes fabricated by conventional, vacuum based PEALD.

5.2 Experimental

Figure 5.1a illustrates the fabricated Pt/Al_2O_3/Al MIM diodes. To deposit the bottom Pt contact for a Pt/Al_2O_3/Al MIM diode, the same processes that were presented in Chapter 3 were used. In the AP-

CVD process, N_2 gas was bubbled through the TMA liquid precursor at a flow of 15 mL min^{-1} and a N_2 carrier gas with a flow of 235 mL min^{-1} assisted the delivery of the TMA. The H_2O was bubbled at a flow of 100 mL min^{-1} and assisted by a 275 mL min^{-1} N_2 carrier flow. The resulting flow per outlet channel was 125 mL min^{-1}. An N_2 inert gas with a flow of 750 mL min^{-1} was used to partially separate the precursors and remove excess unreacted precursors or reaction by-products. The substrate was heated to 150 °C and oscillated underneath the precursor flows with reactor-substrate spacing of 100 µm as shown in Figure 5.1a, at a speed of 6 cm s^{-1}. Nine oscillations of the substrate, which corresponds to 36 sequential exposures to both the TMA and H_2O gas outlets, resulted in a 6 nm thick film, as measured by ellipsometry. This corresponds to a growth rate of ≈ 0.17 nm $cycle^{-1}$, higher than the 0.12 nm $cycle^{-1}$ rate obtained for PEALD of Al_2O_3 in this work and the 0.11 nm $cycle^{-1}$ ALD growth rate of Al_2O_3 reported in Ref.[93] confirming the CVD-nature of the deposition.

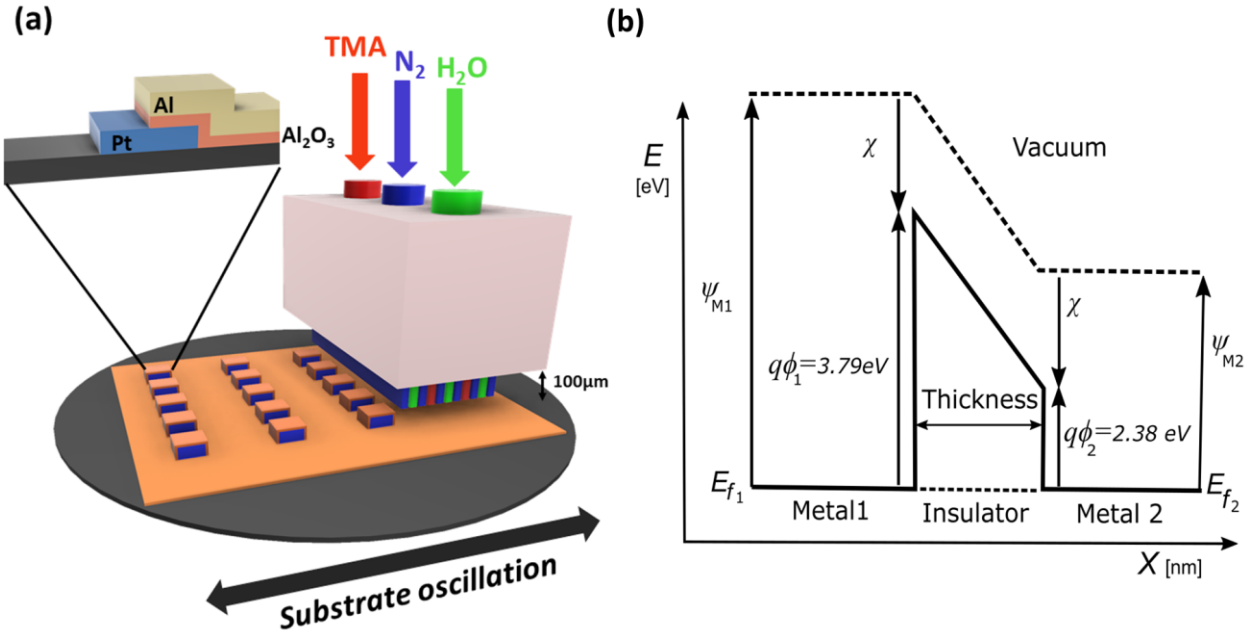

Figure 5.1. (a) Schematic illustration of AP-CVD of an Al_2O_3 film using an AP-SALD reactor and the resulting device architecture after deposition of the top Al electrode and patterning steps. (b) Energy diagram of the Pt/Al_2O_3/Al MIM diode.

The expected energy band diagram for the Pt/Al_2O_3/Al MIM diode is presented in Figure 5.1b. Potential barriers are formed at the interfaces of the metals and the insulator. The barrier height (Φ) is the difference between the work function of the metal (ψ) and the electron affinity of the insulator (χ). The electron affinity of Al_2O_3 fabricated by PEALD has been reported as 1.90 ± 0.2 eV[94] and the work function of Pt and Al are ≈ 5.69[95] and 4.28 eV[96], respectively. Therefore, the left barrier height at the Pt/Al_2O_3 interface is expected to be approximately Φ_L = 3.79 eV, and the right barrier height at the Al/Al_2O_3 interface is expected to be approximately Φ_R = 2.38 eV. The barrier width is defined by the insulator thickness.

Devices with PEALD films were fabricated with similar steps. TMA and O_2 plasma precursors were employed, and 52 cycles were used to deposit a film 6 nm thick. Diodes with insulator thicknesses of 9 and 3 nm were also fabricated and measured. These measurements, which are included in Figure 10.3 Chapter 10, indicate that the optimum diode figures of merit are found in the Pt/Al_2O_3/Al diodes with an insulator thickness of 6 nm. The Al_2O_3 film was deposited at the same temperature of 150 °C with a base pressure below 10^{-6} torr and the load lock pumped below 10^{-5} torr. First, the vacuum chamber was purged with Ar for 3 min to stabilize the chamber pressure and temperature. TMA bubbled with argon was used to dose the substrate for 20 ms at a pressure of 15 mtorr, and then the precursor line was purged with Ar for 1 s at a pressure of 15 mtorr. After that, a flow of O_2 was then stabilized for 500 ms before generating a plasma by radio frequency (RF) with a power of 300 W at a pressure of 15 mtorr, then the substrate was exposed to the O_2 plasma for 2 s and then purged with Ar for 1 s at a pressure of 15 mtorr. Aluminum was deposited as the top contact using the processes described in Chapter 3.

5.3 Results and discussion

The thicknesses of AP-CVD Al_2O_3 films deposited using these conditions were confirmed to be proportional to the number of cycles, as shown in Figure 5.2. Atomic force microscopy (AFM) and scanning electron microscopy (SEM) confirmed the pinhole-free nature of the film, as shown in Figure 5.3.

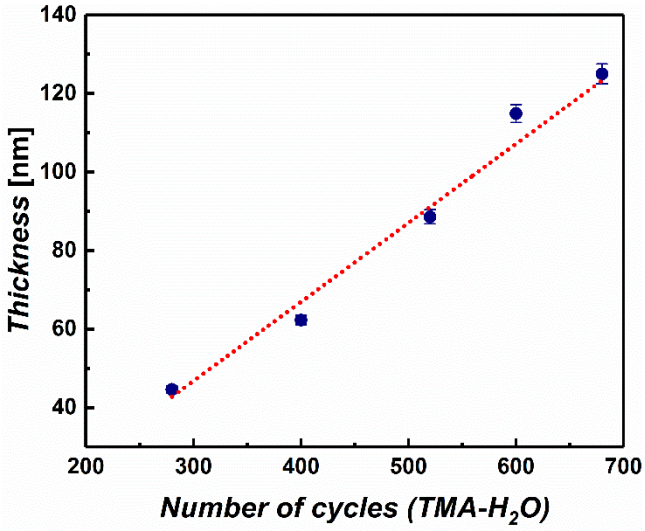

Figure 5.2. Thickness of Al_2O_3 films versus number of TMA-H_2O cycles at 150 °C, as measured by a Dektak 150 profilometer.

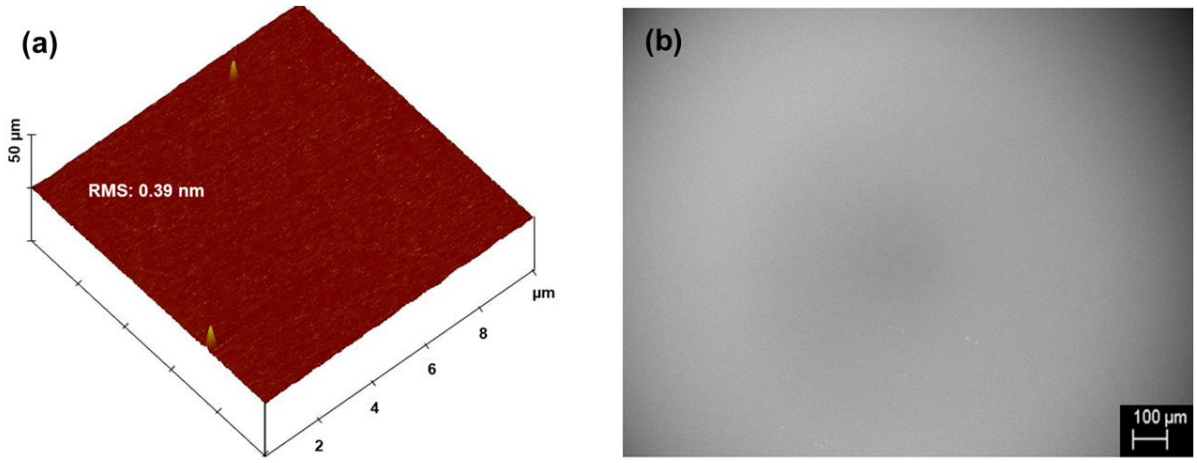

Figure 5.3. Surface morphology of 20 nm Al_2O_3film deposited at 150 °C by atmospheric pressure chemical vapor deposition (AP-CVD): (a) atomic force micrograph, (b) scanning electron micrograph.

The current-voltage (I–V) characteristics of 68 AP-CVD and PEALD MIM diodes were measured over a range of −2 to +2 V. Measurements of a typical device for each fabrication method are shown in Figure 5.4a. Approximately 90% of the fabricated devices were found to work and could be measured multiple times for the applied voltage range of −2 to +2 V.

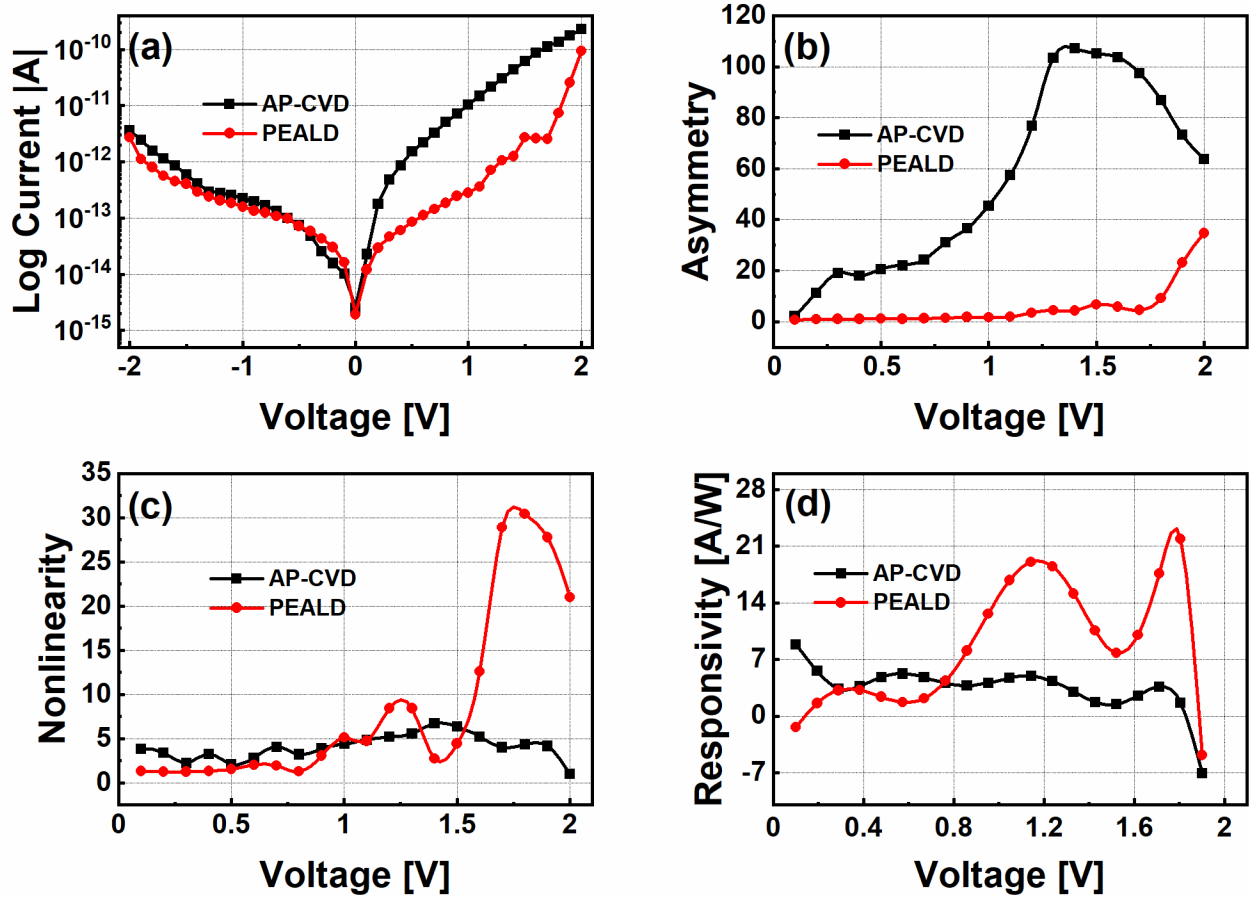

Figure 5.4. (a) The log current vs. voltage of typical Pt/Al_2O_3/Al diodes fabricated by AP-CVD and PEALD. (b) Asymmetry, (c) nonlinearity, and (d) responsivity of the AP-CVD and PEALD Pt-Al_2O_3-Al diodes.

The work function difference between the Pt and Al electrodes results in asymmetric tunneling and an asymmetry that reaches 107 at 1.4 V for the AP-CVD diode and 35 at 2.0 V for the PEALD diodes, as shown in Figure 5.4b. TOVs of 1.4 and 1.75 V were determined for the AP-CVD and PEALD diodes from Figure 5.4 by ELR method as shown in Figure 5.5. The maximum nonlinearities are approximately 6.8 for the AP-CVD diodes and 31 for the PEALD diodes at approximately 1.4 and 1.75 V, respectively, as shown in Figure 5.4c. The maximum responsivities are 8.5 A/W for the AP-CVD diodes and 21.6 A/W for the PEALD diodes, as

shown in Figure 5.4d. Thus, it is found that the diodes employing Al_2O_3 films deposited in open air by AP-CVD show an improvement in asymmetry and turn-on voltage, as compared to the diodes with Al_2O_3 films deposited by PEALD. The average figures of merit for each type of device have been included in Figure 5.6 and the same trend is observed. A similar improvement in asymmetry and TOV, accompanied by a reduced nonlinearity and responsivity, has been suggested previously[6] and was attributed to a reduced barrier height following from an increase in the electron affinity of the insulator. Table 2.2 in Chapter 2 shows that the AP-CVD diode performance compares well to previously reported diodes based on a single layer of Al_2O_3 [32,35–37] in terms of asymmetry, nonlinearity, and responsivity, but has a higher resistance. The increased thickness reduces the probability of electron tunneling, resulting in a low on state current. Thus, The AP-CVD diode has higher zero-bias resistance (5×10^{12} ohm) than previous reports because of the thicker insulator used; however, its resistance is smaller than that of the PEALD diode (7×10^{12} ohm) that has the same insulator thickness.

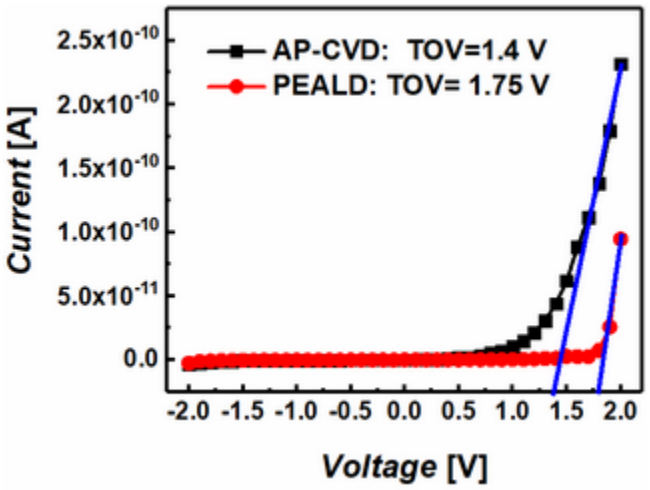

Figure 5.5. Turn-on voltages (TOV) obtained by the extrapolation in the linear region method for Pt/Al_2O_3/Al MIM diodes with 6 nm AP-CVD and PEALD Al_2O_3 layers.

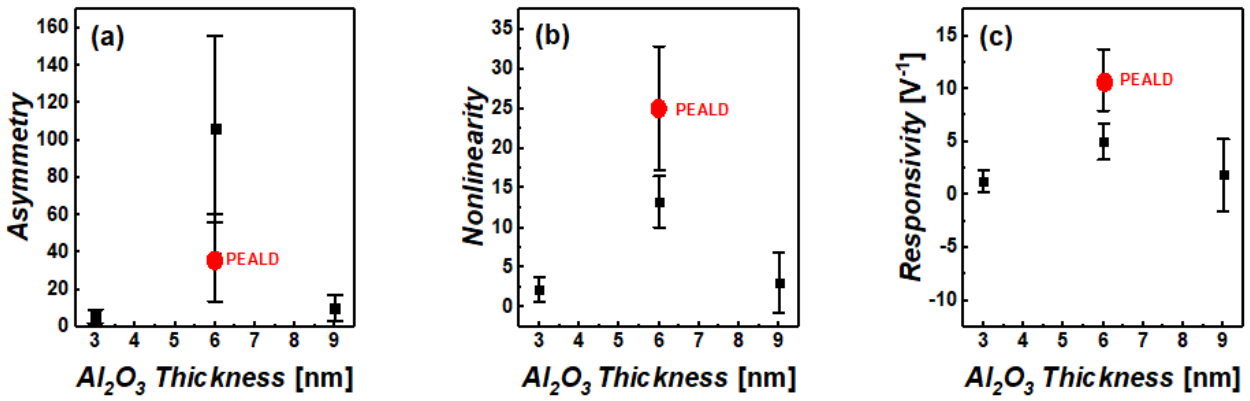

Figure 5.6. Average (a) asymmetry, (b) nonlinearity, and (c) responsivity figures of merit at 1.5 V are shown for the Pt/Al_2O_3/Al MIM diodes with 3 nm, 6 nm, and 9 nm thick AP-CVD Al_2O_3 layers or a 6 nm PEALD Al_2O_3 layer. 17 diodes were measured for each configuration.

The different performance observed for the AP-CVD diodes may result from many factors, such as the type of conduction mechanisms present, the barrier heights between the metals and insulator, as well as roughness and defects in the insulator[14]. Expected conduction processes in MIM diodes include PF, SE, and quantum electron tunneling. To understand the performance observed for the AP-CVD diodes, the I–V curves are fitted to three different conduction mechanisms: PF and SE for the low voltage range and FNT for the high voltage range, in-line with the appearance of these mechanisms in Al_2O_3 films in previous reports[64,97]. This allows the dominant conduction mechanisms for the AP-CVD and PEALD diodes to be identified. The PF and SE equations are fitted to the I–V data at low voltage biases (0.09–0.75 V). This voltage range is selected to investigate the reason for the larger current magnitude observed in the AP-CVD diodes prior to turn-on, compared to that observed in the PEALD

diodes, as shown in Figure 5.4a. The dominant conduction mechanisms were determined by evaluating the quality of fit of conduction mechanisms equations in Chapter 2 to the I–V data, and by comparing the dynamic dielectric constants (ε_r) extracted from the slopes of the PF and SE plots to the expected value.

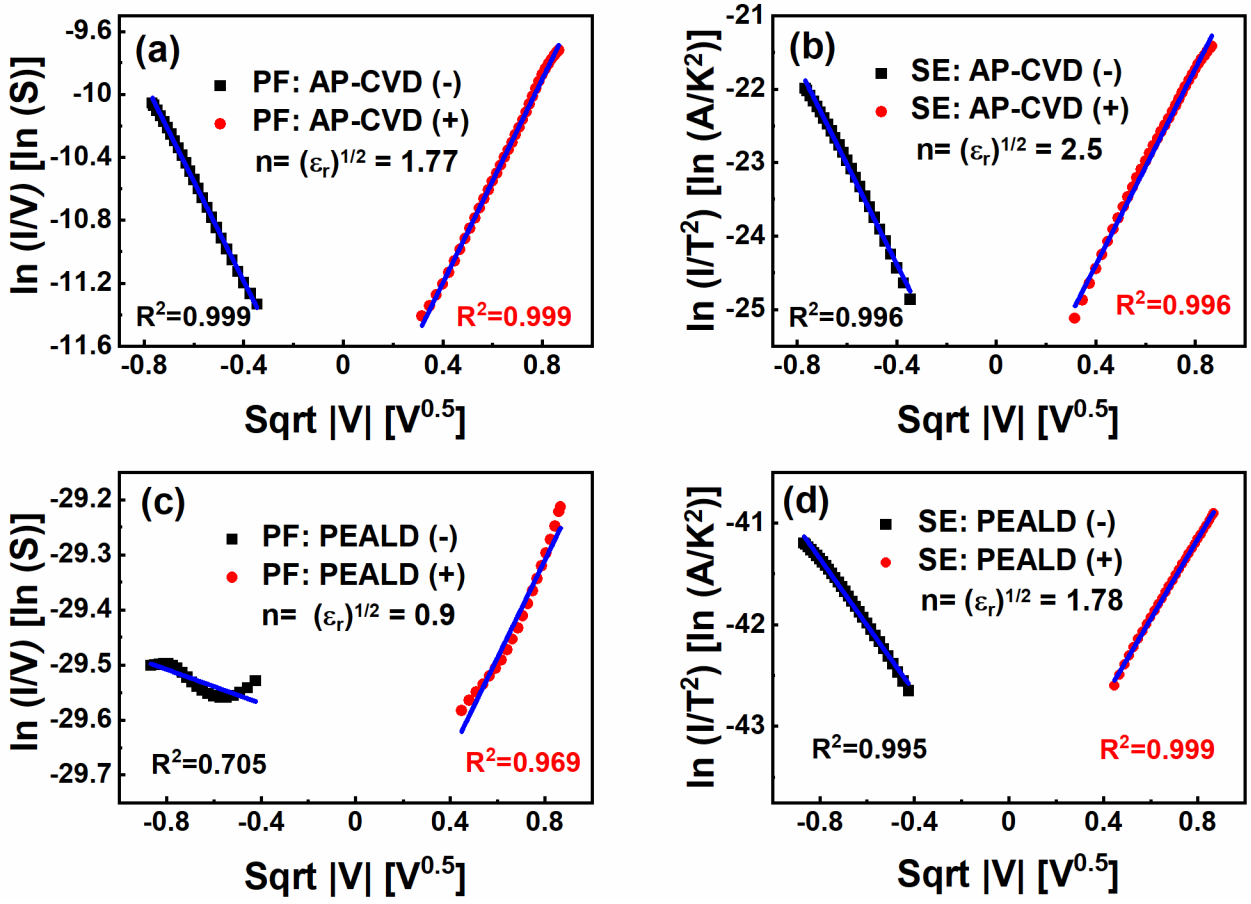

Figure 5.7. Identification of the conduction mechanisms of the diodes at low voltage range (0.09-0.75 V): (a) Poole-Frenkel and (b) Schottky emission of AP-CVD diodes. (c) Poole-Frenkel and (d) Schottky emission of PEALD diodes. Black squares and red circles represent negative and positive polarities, respectively. Plots with $R^2 > 0.99$ are considered to be highly linear and representative of the dominant conduction mechanism. Refractive indices obtained from the fits are indicated.

Figure 5.7a,b shows the I–V data for the AP-CVD diode fitted with the (a) PF and (b) SE relations at low voltage biases (0.09–0.75 V). Slightly better fits are obtained for the PF plots in Figure 5.7a ($R^2 = 0.999$ and $R^2 = 0.999$) than for the SE plots in Figure 5.7b ($R^2 = 0.996$ and $R^2 = 0.996$). Furthermore, the dielectric constants obtained from these fits differ. The ε_r of the AP-CVD diodes extracted from the PF fits in Figure 5.7a is 3.1, whereas the Schottky emission fits in Figure 5.7b indicate $\varepsilon_r = 6.2$. The dynamic dielectric constant is the square of the refractive index $\varepsilon_r = n^2$ which was measured by ellipsometry to be 1.53–1.78 for the AP-CVD Al_2O_3 and 1.60–1.84 for the PEALD Al_2O_3, as shown in Figure 5.8. The value of $\varepsilon_r = 3.1$ from the PF fitting corresponds to a refractive index $n = (\varepsilon_r)^{1/2} = 1.77$, which matches well with the 1.53–1.78 range measured by ellipsometry. This suggests that PF conduction is the dominant conduction mechanism in the AP-CVD diodes at low voltage biases. Figure 5.7c,d shows the I–V data for the PEALD diode fitted with the (c) PF and (d) SE relations at low voltage biases. In contrast to what was observed for the AP-CVD diodes, better fits are obtained for the SE plots in Figure 5.7d ($R^2 = 0.995$ and $R^2 = 0.999$) than for the PF plots in Figure 5.7c ($R^2 = 0.705$ and $R^2 = 0.969$). Furthermore, the refractive index of n = 1.78 obtained from the SE plots matches the 1.60–1.84 range measured by ellipsometry. This indicates that SE is the dominant mechanism in the PEALD diodes at low voltages.

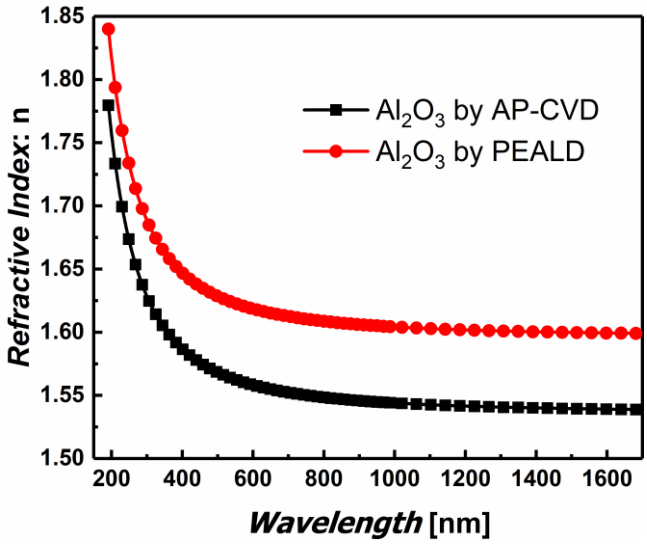

Figure 5.8. Refractive indices of Al_2O_3 measured by ellipsometry for AP-CVD and PEALD films.

In Figure 5.9, the diode I–V data for both Al_2O_3 deposition methods is fitted with the FNT expression from Equation 2.2 in Chapter 2. In both cases, excellent fitting is obtained ($R^2 > 0.999$), indicating that FNT is the dominant conduction mechanism at high voltage biases, regardless of the Al_2O_3 deposition method.

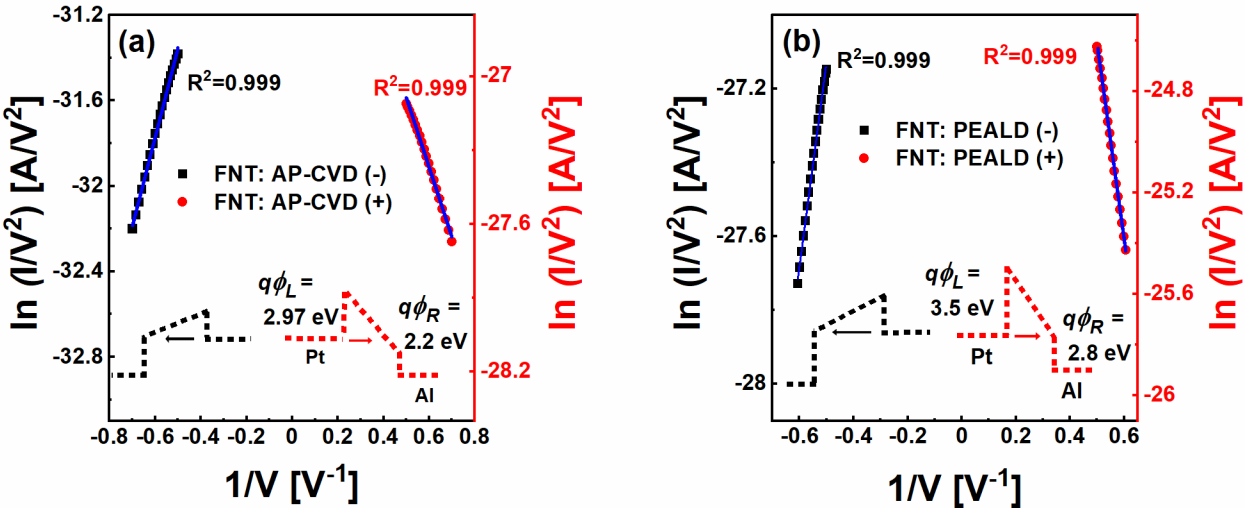

Figure 5.9. Fowler–Nordheim tunneling plots fitted from measured I–V curves of (a) AP-CVD and (b) PEALD diodes. Barrier heights are determined from the slopes of the plots and are shown in the insets.

The metal-insulator barrier heights can be calculated from the slopes of the FNT plots in Figure 5.9. A clear difference in barrier heights is observed between the AP-CVD and PEALD diodes. For the AP-CVD diodes, the left barrier height Φ_L (Pt/Al_2O_3), which is the barrier height in the reverse current direction, is found to be 2.97 eV and the right barrier height Φ_R (Al_2O_3/Al), which is the barrier height in the forward current direction, is found to be 2.20 eV. For the PEALD diodes, larger barriers of Φ_L = 3.50 eV and Φ_R = 2.80 eV are obtained. These barriers are illustrated schematically in the insets of Figure 5.9 The forward Al_2O_3–Al barrier heights of 2.20 and 2.80 eV observed in the AP-CVD and PEALD diodes, respectively, are consistent with previously reported values of 2.25[98] and 2.47 ± 0.36 eV[64] that were obtained theoretically and a value of 2.0 ± 0.2 eV obtained from photoemission studies[99]. The lower barrier height observed for the AP-CVD diodes in this work is consistent with a previous study that indicated that thermal ALD of Al_2O_3, which is similar to the AP-CVD process used here, resulted in a

barrier two times smaller than that obtained with PEALD[64]. The surface chemistry is expected to influence the barrier height. Ref.[100] for example, studied ZrCuNiAl/Al_2O_3/Al MIM diodes and found that their barrier heights varied with the method used to deposit the Al electrode. They attributed this to modulation of the chemistry associated with barrier formation, resulting from energetic interactions between the impinging Al and the Al_2O_3. In particular, more energetic DC sputtering of Al resulted in larger barriers than evaporation.

The difference in barrier height observed in this work may similarly be due to different surface chemistries. AP-CVD is a less energetic deposition process than PEALD and it will be shown that it results in a larger concentration of OH^- on the surface of the Al_2O_3. MIM diodes are known to exhibit good performance when the forward barrier height is smaller[6]. A low barrier height is expected to minimize the turn-on voltage and promote higher asymmetry[35]. This is consistent with the results observed in this work. The smaller barrier heights observed in Figure 5.9 for the MIM diodes with AP-CVD Al_2O_3 resulted in a lower turn-on voltage of 1.4 V in Figure 5.4a. In the AP-CVD diodes, the turn-on voltage of 1.4 V results in a transition from PF to FNT-dominated conduction, whereas in the PEALD diodes that have a larger barrier, a larger TOV of 1.75 V is required for the conduction to transition from SE-dominated to FNT-dominated. Correspondingly, the AP-CVD diodes demonstrated superior asymmetry and nonlinearity at 1.4 V in Figure 5.4b,c when the conduction mechanism changed from PF to FNT at the TOV. These results indicate that the insulator deposition method has an impact on the barrier height and MIM diode properties, consistent with previous reports[64].

To understand the reason for the different conduction mechanisms in the AP-CVD and PEALD diodes at small voltage biases, XPS was performed on the Al_2O_3 films deposited by AP-

CVD and PEALD to clarify the chemical composition and bonding. Deconvolution of the O1s peaks by Gaussian fitting in Figure 5.10a,b reveals peaks at 531 and 532.3 eV, which correspond to the O^{-2} in Al_2O_3 and hydroxyl OH^- groups[64,65]. The fraction of the O1s signal attributable to these two components is calculated for the AP-CVD and PEALD Al_2O_3 films based on the area under the corresponding XPS peaks. A larger contribution from the OH^- groups is observed for the AP-CVD Al_2O_3 in Figure 5.10a, which is attributed to the use of H_2O as the oxygen precursor in this deposition method, consistent with Ref.[64,65]. The XPS data represents a surface measurement and it is known that thermal deposition at low temperatures using H_2O as the oxidant usually results in a large amount of OH^- on the film surface[65,66]. The large OH^- signal may be due to incomplete reaction of the precursors and the high desorption energy of water at low temperatures[66]. The hydroxyl groups are expected to act as electron traps in the films, enabling PF conduction at low voltages[64], consistent with the PF-dominated conduction observed for the AP-CVD diodes in Figure 5.7a. The Al_2O_3 fraction of the O1s peak is much higher for the PEALD film in Figure 5.10b, which is attributed to the high reactivity in this deposition method that utilizes an O_2 plasma and produces more dense films, as reported previously[101]. This is consistent with a higher Al at% observed for the PEALD film, as reported in Table 5.1. The Al 2p spectra in Figure 5.10c show a peak located at 74 eV for both the AP-CVD and PEALD Al_2O_3, which is attributed to Al_2O_3[102]. Carbon is observed in both the AP-CVD and PEALD Al_2O_3 films and may result from incomplete removal of $-CH_3$ groups under the modest deposition temperature. Also, air contamination is expected when transporting the samples to the XPS equipment.

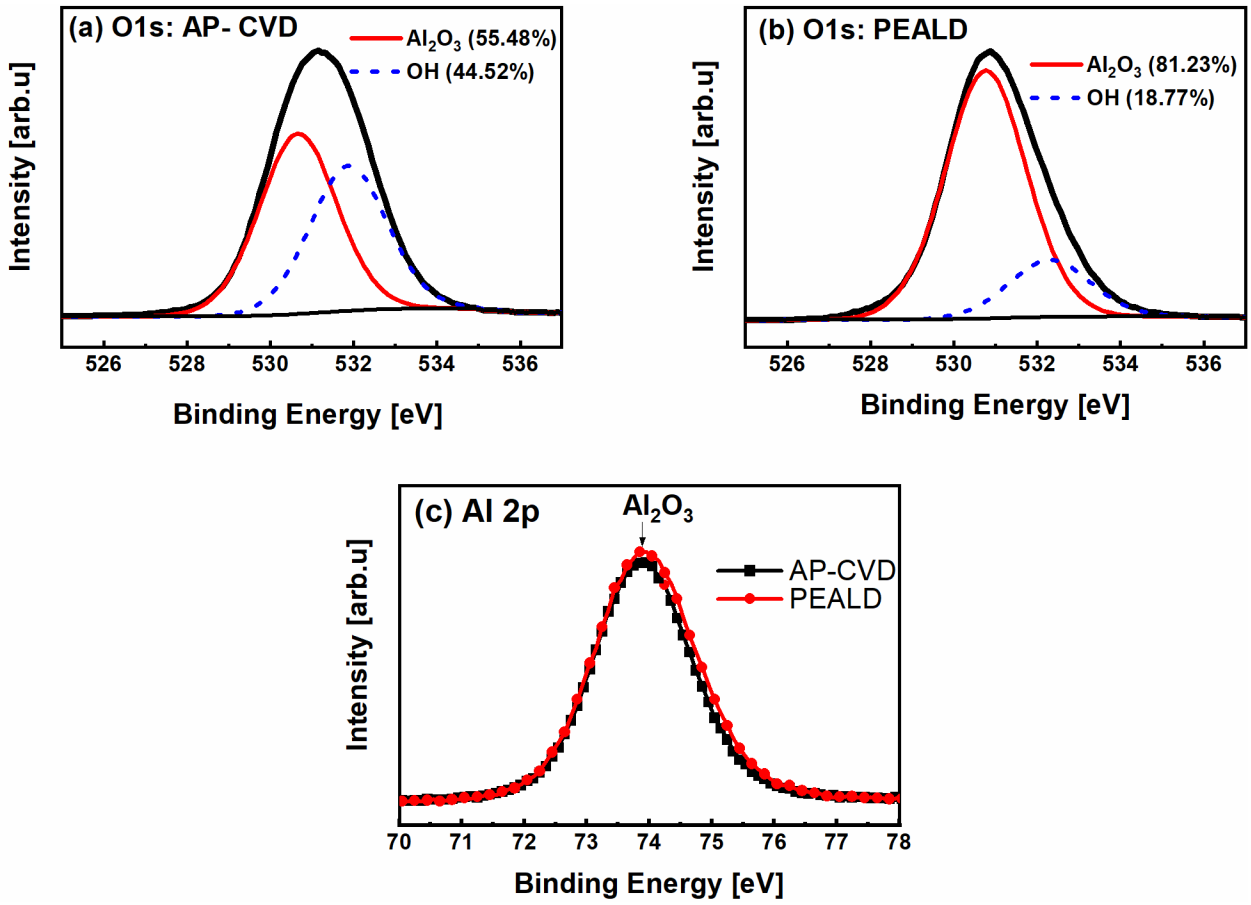

Figure 5.10. O 1s and Al 2p XPS spectra of Al_2O_3 films: (a) O1s: AP-CVD (b) O1s: PEALD (c) Al 2p.

Table 5.1. Film compositions of AP-CVD and PEALD Al_2O_3 films, as determined by x-ray photoelectron spectroscopy.

Technique	Film Compositions (at%)			
	O	Al	C	O/Al
AP-CVD	47.1	31.3	21.6	1.50
PEALD	44.6	33.7	21.7	1.32

Chapter 6
Nanoscale Film Thickness Gradients Printed in Open Air by Spatially Varying Chemical Vapor Deposition

6.1 Overview

Nanoscale coatings are integral components of all modern electronics, including display technologies, diodes, solar cells, batteries, and smart windows. In R&D settings, researchers must vary the thickness of thin films to optimize device performance. This typically involves making several batches of devices, each with a different film thickness, and this process must be repeated for each film present in the device. In addition to being time-consuming, this iteration of material synthesis and device fabrication results in experimental artifacts due to uncontrolled differences in experimental conditions. These challenges can be addressed by using combinatorial and high-throughput (CHT) techniques[13]. In CHT approaches, a thin film is produced whose properties (in this case, thickness) vary across its surface. Multiple devices can then be produced at different locations on the film surface and compared without batch-to-batch variation, making the technique faster and more reliable. This approach also significantly reduces

the time and material costs during experimentation. In addition to CHT analysis, films with thickness gradients present an opportunity for novel functionality.

Nanoscale films with thickness gradients have been produced using vacuum-based techniques. Physical vapor deposition has been used to produce thickness gradients[103], and gas flows have been controlled in chamber-based ALD and CVD systems to produce nanoscale thickness gradients[104–106]. While useful in some cases, these vacuum-synthesized films are not suitable for cost-effective and high-throughput nanomanufacturing in atmosphere. In contrast, atmospherically processed films with nanoscale thickness gradients are less developed. This is despite the fact that atmospheric processing is desired for many emerging technologies (flexible electronics, low-cost solar cells, wearable electronics, smart windows, etc.). Combinatorial atmospheric chemical vapor deposition and spray pyrolysis have been used to achieve composition and thickness gradients[107,108]; however, the thicknesses were in the range of several hundreds of nanometers and reproducibility is an issue with spray pyrolysis, as the film quality depends on the droplet size and spray nozzle.[109] A flow coating technique has been shown to produce a thickness gradient on the order of 10 nm for polymer films in atmosphere[110,111], but for most materials there are no demonstrations of nanometer-scale thin film thickness gradients. A summary of some reported combinatorial thickness-gradient films and methods are presented in Table 6.1.

Table 6.1. Summary of some previously reported combinatorial thickness-gradient methods.

Pressure types	Fabrication Method	Thickness gradient film [nm]	Application	Ref
Vacuum-based synthesis	Physical vapor deposition	$La0.8Sr_{0.2}(Mn_{1-x}Co_x)_{0.85}O_{3\pm\delta}$ (80-175)		[103]
	HV-CVD	TiO_2 (50-400)		[104]
	Sputtering	Cu (200-900)		[112]
	Electron beam evaporation	Pd (0-50)	IR imaging	[113]
	ALD	W (0-50)		[105]
Atmospheric pressure synthesis (no vacuum)	AP-CVD	Mixed vanadium oxide and vanadium oxynitride (90- 775).		[114]
	Spray pyrolysis	TiO_2 (100-300) Cu_2O (200-600)	Solar cells	[108]
	Flow coating	Polymer (90 to 140), sub 10 nm		[110],[111]
	Horizontal dip coating	3 different polymers (200-350) deposited on tilted stage	DFB laser	[115]

This chapter introduces large-area thin films with thickness gradients on the nanometer scale that are manufactured using spatially varying AP-CVD techniques. Metal oxide films (Al_2O_3, ZnO) with nanoscale thickness gradients are rapidly printed in atmosphere and their use in CHT studies of MIM diodes is demonstrated.[116]

6.2 Atmospherically printed films with nanoscale thickness gradients

Figure 6.1 illustrates the working principle of the dual atmospheric pressure spatial atomic layer deposition/chemical vapor deposition (AP-SALD/CVD) system. Precursor and

reactant vapors flow to a reactor head, which has parallel gas outlet channels along its bottom surface. The flows of the precursor and reactant vapors are isolated from each other by a curtain of inert nitrogen gas and exhaust channels (not shown in Figure 6.1a) located between the precursor and reactant channels: see Ref.[43]. The substrate is placed under the atmospheric reactor with a small vertical separation (typically d~ 50 μm) and is oscillated back and forth to expose the substrate to alternating reactant flows. Each point on the substrate moves underneath the precursor and adsorbs a molecular layer, after which the flow of inert gas removes any excess precursor. When the substrate moves under the reactant gas, which reacts with the layer of precursor on the substrate, a monolayer of the desired film is formed. By oscillating the substrate back and forth, pinhole-free films with nanoscale thickness control can be deposited. Spatial atomic layer deposition has been demonstrated for a variety of materials, substrates, and applications[47,117–119]. When operating as an AP-CVD system, experimental conditions are selected such that the inert gas flow and exhaust strength are insufficient to prevent mixing of the precursor and reactant vapors during the oscillation of the substrate. Notably, this can be achieved by using a large reactor-substrate spacing[15,120]. In AP-CVD, the reactions are no longer surface self-limited. Higher growth per cycle values are obtained for AP-CVD (typically on the order of 1 nm/cycle), but conformal pinhole-free films are still produced[46]. This AP-CVD approach has been used to incorporate films into a variety of devices[46], and has sometimes been referred to as spatial CVD[121].

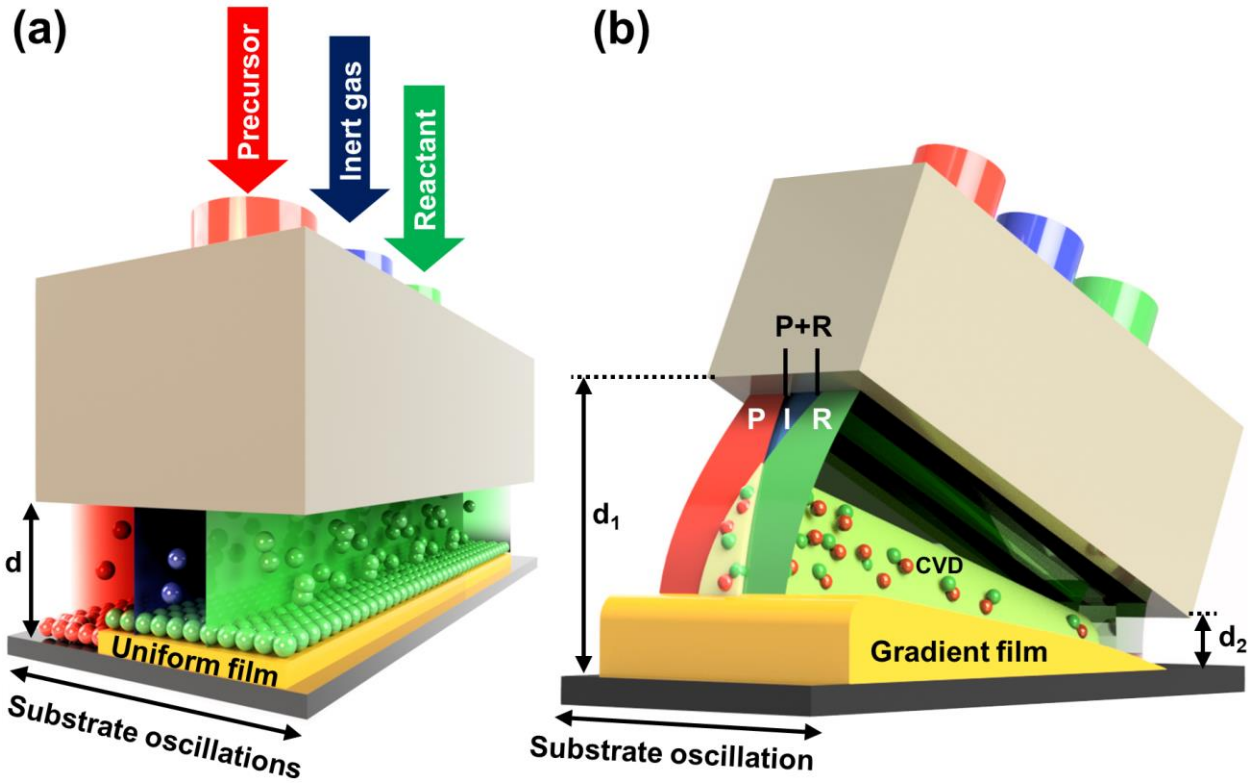

Figure 6.1. Variable reactor-substrate spacing approach to produce nanoscale film thickness gradients. (a) Close-proximity AP-SALD approach with uniform reactor-substrate spacing d isolates the precursor and reactant gases, resulting in surface self-limited ALD and uniform film thickness. (b) By inclining the reactor head, a variable reactor-substrate spacing d_1,d_2 were produced, causing mixing of the precursor and reactant to a varying extent, which results in a spatially varying chemical vapor deposition rate and a film with a thickness gradient.

The fact that the AP-CVD deposition rate is influenced by the reactor-substrate spacing was leveraged here to produce nanoscale thickness gradients in ZnO and Al_2O_3 films. The distance between the reactor head and the substrate was varied along the length of the reactor resulting in a reactor-substrate spacing of 90 to 150 µm (d_1) on one side and a larger spacing of 150 to 250 µm (d_2) on the other side, as shown in Figure 6.1b. More gas-phase mixing of the

precursors occurs where the reactor-substrate spacing is larger, as shown on the left side of Figure 6.1b, resulting in an enhanced AP-CVD mode, which in turn yields a higher deposition rate. By varying the reactor-substrate spacing continuously across the substrate, a spatially varying deposition rate is expected that will result in a thickness gradient. Computational Fluid Dynamics (CFD) analysis were performed by collaborator Viet Huong Nguyen to simulate the phenomenon (see Figure 10.4-10.7 and Table 10.1 in Chapter 10).

6.3 Experimental

Zinc oxide films were deposited in this manner on 7×7 cm borosilicate glass substrates and 1.6×1.6 cm indium-tin-oxide/glass (ITO) substrates using diethylzinc (DEZ) and water. For the deposition of ZnO films, N_2 was bubbled through the DEZ precursor at 15 sccm and combined with an 85 sccm N_2 carrier gas. The H_2O was bubbled at 30 sccm and combined with a 170 sccm N_2 carrier flow. The resulting flow per outlet channel was 100 sccm. A 600 sccm flow of N_2 inert gas was used to partially separate the precursors and remove excess unreacted precursors or reaction by-products. The substrate was heated to 150 °C.

For the deposition of Al_2O_3 gradient films on the Si substrate and the MIM diodes, N_2 was bubbled through the TMA precursor at 15 sccm and combined with a 235 sccm N_2 carrier gas. The H_2O was bubbled at 100 sccm and combined with a 275 sccm N_2 carrier flow. The resulting flow per outlet channel was 125 sccm. A 750 sccm flow of N_2 inert gas was used. The substrate was heated to 150 °C.

6.4 Results and discussion

6.4.1 Characterization of thickness gradient film

Figure 6.2a shows a 95 nm thick uniform ZnO film deposited on glass using a uniform reactor-substrate spacing of 100 μm and 75 substrate oscillations at an oscillation speed of 15 mm/s. The final thickness indicated a growth per cycle (GPC) of approximately 0.63 nm/cycle (~0.28 nm/s) (the DEZ precursor was flowed through one channel so one oscillation of the substrate back and forth was the equivalent of two precursor-reactant cycles). This GPC is consistent with AP-CVD growth rates reported previously[122]. The properties of uniform ZnO films produced using similar conditions on this AP-SALD/CVD system have also been reported previously[122]. Figure 6.2b shows a thickness gradient film obtained by setting the reactor-substrate spacing to 150 μm on the left side and 90 μm on the right side, after 40 substrate oscillations at a speed of 15 mm/s. A clear gradient in the film thickness is observed, which was measured by ellipsometry to be 70 nm thick on the left of the film and 35 nm on the right, indicating GPCs of approximately 0.87 nm/cycle and 0.43 nm/cycle, respectively. When depositions were repeated with the reactor-substrate spacing set to 200 and 250 μm on the left side and 100 μm on the right side, with 100 and 75 substrate oscillations at a speed of 15mm/s, the resulting thickness ranges increased to 200-160 nm (Figure 6.2c) and 180-100 nm (Figure 6.2d), respectively, indicating GPCs from approximately 0.7 to 1.2 nm/cycle, all consistent with AP-CVD. Figure 6.2e shows a 200-160 nm gradient produced on four ITO substrates using the same 200-100 μm reactor-substrate spacing, 75 substrate oscillations and an oscillation speed of 10 mm/s. This demonstrates the ability of the technique to produce thickness gradient films on

typical substrate sizes used for device studies (e.g., solar cells and LEDs). Figure 6.2f shows thickness profiles for the ZnO films in Figure 6.2c-d, as measured by ellipsometry. The film thicknesses are observed to decrease continuously across the glass substrates. This agrees with the CFD simulation results in Chapter 10.

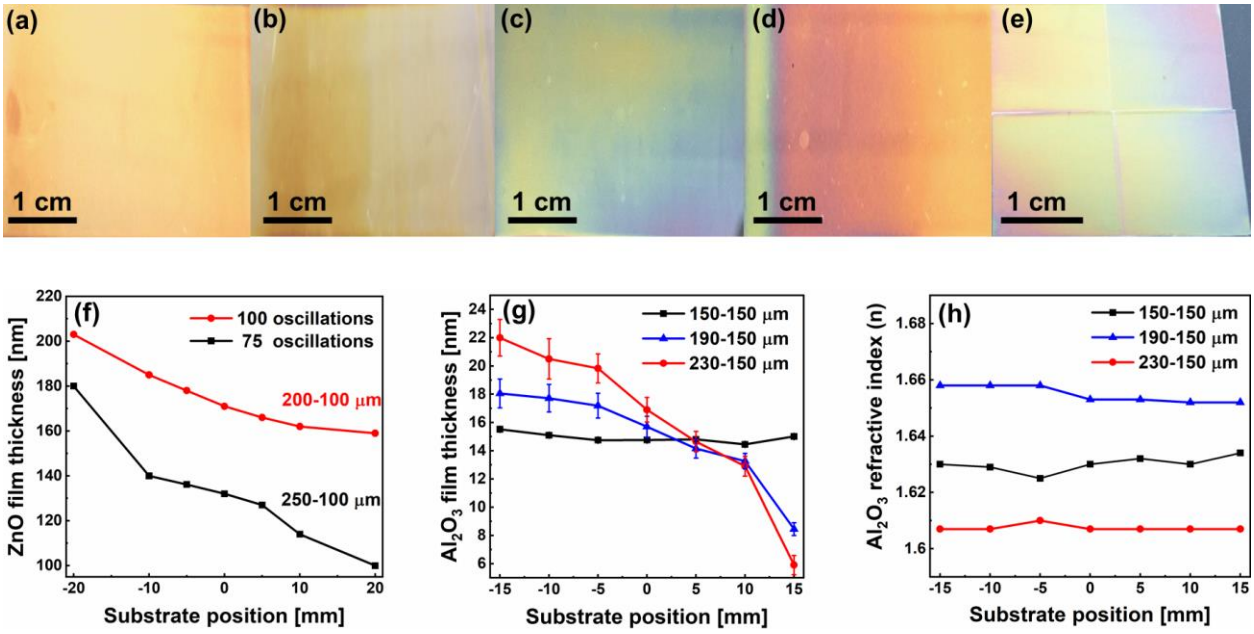

Figure 6.2. ZnO and Al_2O_3 thickness gradient films deposited with a variable reactor-substrate spacing. (a) 95 nm uniform ZnO film deposited on glass using a uniform 100 μm reactor-substrate spacing and 75 substrate oscillations. (b) 70-30 nm gradient ZnO film deposited on glass using a variable 150-90 μm reactor-substrate spacing and 40 substrate oscillations. (c) 200-160 nm gradient ZnO film deposited on glass using a variable 200-100 μm reactor-substrate spacing and 100 substrate oscillations. (d) 180-100 nm gradient ZnO film deposited on glass using a variable 250-100 μm reactor-substrate spacing and 75 oscillations. (e) Four ITO substrates coated together with a 200-160 nm thickness gradient. (f) Thickness of gradient ZnO films shown in (c) and (d). (g) Thickness of gradient Al_2O_3 films produced on Si substrates by different reactor-substrate spacings. (h) Refractive indices of the gradient Al_2O_3 films, measured along the gradient.

The properties of uniform Al_2O_3 films produced on this AP-SALD/CVD system have been reported previously[15,122]. A reactor-substrate spacing of 150 μm was maintained on the right side and 150, 190, or 230 μm on the left side. In all cases, the substrate was oscillated 20 times at a speed of 10 mm/s. Thicknesses determined from ellipsometry measurements at various locations across the Al_2O_3 films are shown in Figure 6.2g. A uniform film thickness of 15 nm was observed when the reactor-substrate spacing was a constant 150 μm. When the left side of the reactor was raised to 190 μm, a thickness gradient ranging from 18-8 nm thick was produced. The gradient further increased to approximately 22-6 nm when the left side was raised to 230 μm. Three thickness measurements were performed perpendicular to the intended gradient for each substrate position and the standard deviation is indicated by the error bars in Figure 6.2g. There is some thickness variability in the perpendicular direction. This is expected as the reactor-substrate spacing may not stay perfectly constant throughout the travel distance due to how the substrate sits on the stage, non-uniformity in the substrate thickness, and/or levelling of the stage relative to the travel distance. But Figure 6.2g shows that the overall gradient is still consistent. For Al_2O_3 depositions, the TMA precursor was flowed through two channels, thus one oscillation is the equivalent of 4 precursor-reactant cycles. These depositions took approximately 300 s, had GPCs that varied from approximately 0.37 to 0.51 nm/cycle (0.1 to 0.14 nm/s) across the substrate, and demonstrate the ability of this approach to produce films with thickness gradients at the scale of nanometers in open-air in very short deposition times. In Figure 6.2h, refractive indices at 630 nm measured along the gradient films by ellipsometry are shown. These matched well with the 1.53–1.78 range reported previously for Al_2O_3[15] and were constant along the thickness gradient. An Al_2O_3 gradient film with a larger thickness variation

(86-7 nm) that was deposited using a variable 400-100 μm reactor-substrate spacing, 20 oscillations, and a speed of 30 mm/s was also characterized by ellipsometry and is shown in Figure 10.8 in Chapter 10. For the larger thickness range, the refractive index decreases slightly with increasing thickness, consistent with previous reports for Al_2O_3 made by thermal ALD[123].

XPS was performed on one of the Al_2O_3 thickness gradient films from Figure 6.2g (230-150 μm reactor-substrate spacing) to clarify the film composition and bonding. The XPS data is presented in Table 6.2.

Table 6.2. Film composition of an Al_2O_3 thickness gradient film by x-ray photoelectron spectroscopy.

Thickness	Al_2O_3 Film compositions (at%)			
[nm]	O	Al	C	O/Al
6	42.15	30.8	27.05	1.37
12	42.66	31.16	26.17	1.37
18	45.82	33.48	20.7	1.37
22	46.77	31.56	21.67	1.48

The O/Al ratio is fairly constant across the Al_2O_3 thickness gradient film, with a slight increase at the thicker end. A carbon signal is present across the gradient and may be due to incomplete reaction of the TMA or adventitious carbon on the surface of the sample, resulting from storage in air and/or the XPS instrument[15,57,124]. It is known that OH^- defects in Al_2O_3 can act as electron traps that facilitate the transport of electrons[15,64]. The O1s spectra was deconvoluted for the different film thicknesses, as shown in Figure 6.3. The peaks at 531 and 532.3 eV correspond to Al-O and hydroxyl OH^- groups[15], respectively. The contribution of the

OH^- peak is high, as expected, as H_2O was used as the oxidant[15]. Notably, the contribution of the OH^- peak was similar across the gradient film.

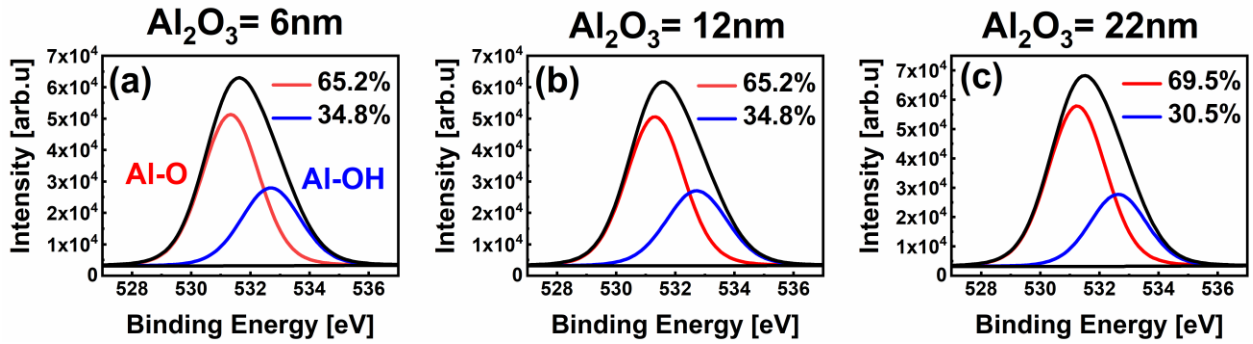

Figure 6.3. O1s XPS spectra of an Al_2O_3 thickness gradient film measured at different thicknesses: (a) 6 nm, (b) 12 nm, (c) 22 nm.

ZnO gradient film (180-70 nm) was characterized to identify any property variations across the gradient. Absorbance measurements and bandgap calculations are shown in Figure 6.4. The absorbance shows a slight increase with thickness, as expected, and the bandgap remains constant at ~3.4 eV, indicating minimal variation in the position of the energy levels.

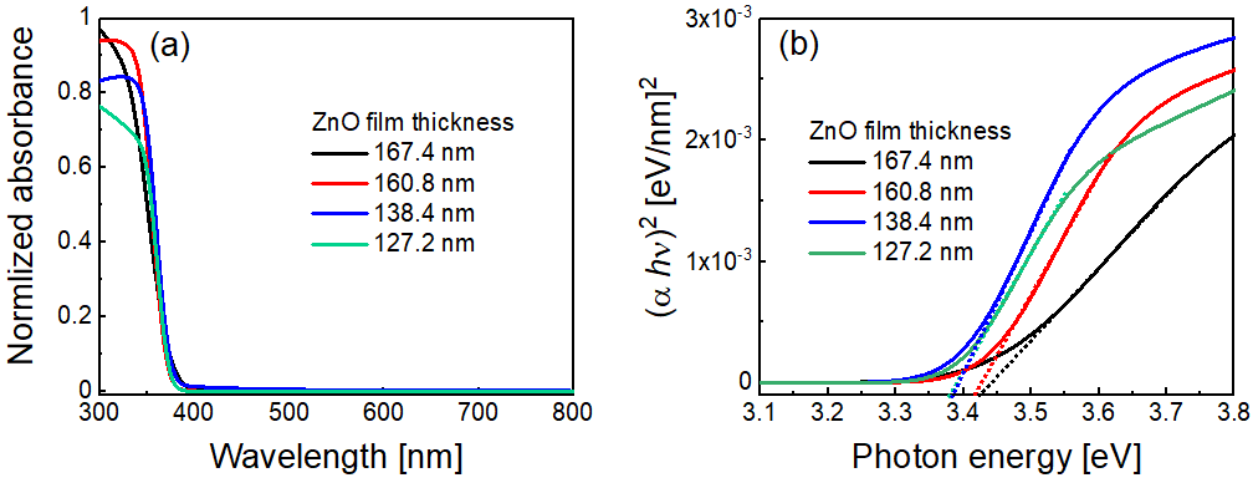

Figure 6.4 (a) Absorbance and (b) Tauc plots of a ZnO gradient film.

X-ray diffraction (XRD) was performed to investigate the growth orientation and crystallinity. Figure 6.5 shows that the ZnO grew in the [100], [002], [101], [102], [110], [103], and [112] directions, and that the relative height of the peaks remained similar across the gradient. The full-width-at-half-maximum (FWHM) of the 100 peaks was determined, and the crystallite size was calculated using the Scherrer equation[125]:

$$L = \frac{k\lambda}{\gamma cos\theta} \tag{6.1}$$

where L is crystallite size, k is a constant = 0.9, λ is the X-ray wavelength=0.154 nm, γ is the peak width at half the maximum intensity (FWHM), and θ is the Bragg angle. The FWHM has a larger value at the thickness of 70 nm (Figure 6.5b), which may be due to mismatch strain between the ZnO film and the glass substrate, and then decreases with increasing film thickness, in agreement with Ref.[126]. As a result, the crystallite size increases with increasing film thickness.

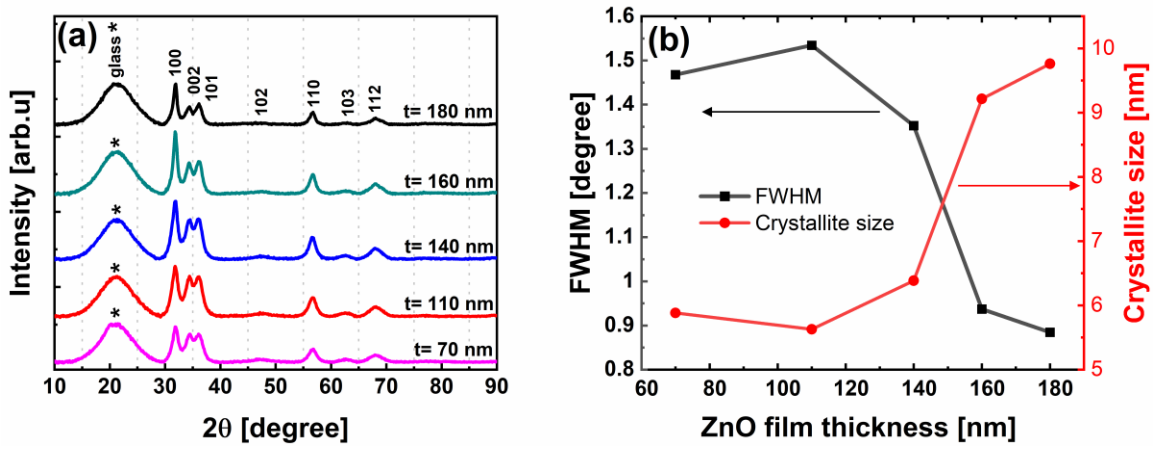

Figure 6.5. (a) XRD measurements of the thickness gradient ZnO film. (b) FWHM and crystallite size values measured for the 100 diffraction peaks in (a).

6.4.2 CHT study of metal-insulator-metal diodes

In this work, Pt/Al_2O_3/Al MIM diodes with an Al_2O_3 thickness gradient film were fabricated, as illustrated in Figure 6.6a, to optimize the diode performance more rapidly and systematically. The variable reactor-substrate spacing approach was implemented to deposit the insulating Al_2O_3 film, with a spacing of 150 μm on one side of the reactor and 100 μm on the other. Six substrate oscillations (24 cycles) were used to deposit the gradient film. This deposition took about 45 s and had GPCs that varied from approximately 0.11 to 0.41 nm/cycle (0.05 to 0.22 nm/s) across the substrate. Aqueous sodium hydroxide was used to etch a step edge in the Al_2O_3 film before depositing the second metal (Al), in order to measure the film thickness at various locations along the substrate using atomic force microscopy (AFM). The AFM images in Figure 6.6f show that the Al_2O_3 thickness varied from approximately 10 nm on one side to 2.5

nm on the other side of the substrate, clearly showing the ability of this technique to produce sub-10 nm thickness gradients. Finally, the top Al electrode was deposited using electron beam evaporation and lithography. There were 18 columns of diodes on the wafer such that the combinatorial approach allowed for the study of 18 different insulator thicknesses on a single substrate. Each column contained 20 diodes, enabling statistical analysis for each insulator thickness.

Current density-voltage (J-V) measurements on the MIM diodes were performed to determine their figures of merit. The J-V curves were asymmetrical and nonlinear for the thicker diodes, as shown in Figure 6.6b for the diodes with insulator thicknesses of 8.5±1.9 nm and 6.5±1.9 nm. In contrast, the J-V curve for a thinner insulator layer (2.5±0.2 nm) in Figure 6.6b shows low asymmetry. The TOV was determined by extrapolation in the linear region[76] and it is seen to decrease from approximately 3.1 V to 1.0 V in Figure 6.6b as the insulator becomes thinner. Figures 6.6c, d, and e show the dependence of the figures of merit (asymmetry, nonlinearity, and responsivity) on the Al_2O_3 thickness. The asymmetry was calculated at the TOV for each diode and it is seen to increase with Al_2O_3 thickness in Figure 6.6c, reaching a maximum value of 78 at an Al_2O_3 thickness of 6.5 nm and 1.8 V. The asymmetry decreases for insulator thicknesses larger than 6.5 nm. This is attributed to an increase in the reverse current with increasing voltage for thicker insulators, which decreases the asymmetry ratio. The nonlinearity and responsivity were calculated at the TOV and showed maximum values of 11.0 and 5.5 A/W, respectively, for an Al_2O_3 thickness of 7 nm. Therefore, this CHT study indicates

that the optimum figures of merit for the Pt/Al_2O_3/Al MIM diode can be obtained with an insulator thickness of 6.5 to 7.0 nm.

For the thin Al_2O_3 gradient films, little variation in refractive index (Figure 6.2h), composition (Figure 6.3, Table 6.2), and surface roughness (Figure 6.6f) were observed across the gradient. Therefore, it is expected that the behavior of the MIM diodes depends mostly on the thickness of the Al_2O_3. To confirm this, the J–V curves of the MIM diodes with different insulator thickness were fitted to an expected conduction mechanism, FNT, as shown in Figure 6.6g. Figure 6.6g shows that as the Al_2O_3 thickness increased, the applied bias required to make FNT the dominant conduction mechanism increased and the forward current was reduced, as the thicker insulator results in a reduction in the tunneling probability.

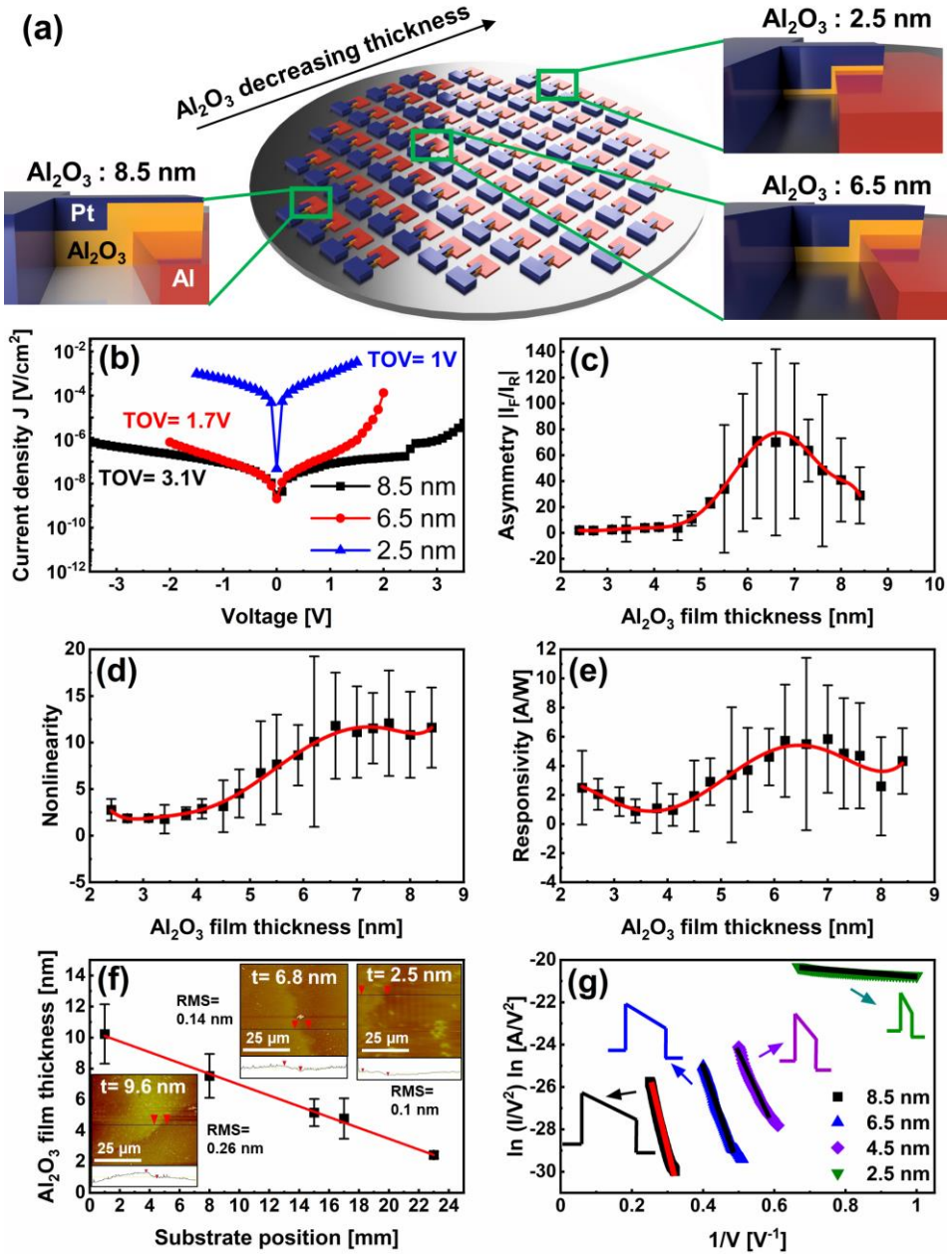

Figure 6.6. CHT study of MIM diodes. (a) Pt/Al_2O_3/Al MIM diode architecture with Al_2O_3 thickness gradient film. Diodes with 18 different Al_2O_3 thicknesses were tested. (b) J-V curves for 3 of the Pt/Al_2O_3/Al diodes. (c) Asymmetry, (d) nonlinearity and (e) responsivity of the diodes for the 18 different Al_2O_3 thicknesses (measured at the TOV). (f) AFM measurements indicated that the Al_2O_3 film thickness varied from 10 nm to 2.5 nm and the RMS surface roughness increased slightly from 0.1 nm to 0.26 nm. (g) FNT plots at forward bias for Pt/Al_2O_3/Al MIM diodes with Al_2O_3 thickness gradient film. The legend indicates the Al_2O_3 thickness.

6.4.3 Performance comparison

The optimized figures of merit reported here are comparable to or better than those of previously reported diodes with a single Al_2O_3 layer[15,32,35–37,40,127], as summarized in Table 2.2 in Chapter 2. The use of this thickness gradient Al_2O_3 film has enabled the identification of a slightly larger optimal Al_2O_3 thickness (6.5 to 7.0 nm) than what reported previously for $Pt/Al_2O_3/Al$ diodes deposited by AP-CVD (6 nm) in Chapter 5. The greater Al_2O_3 thickness (~7 nm) that was identified in this CHT study does result in a lower current density compared to some of the previous reports (a decrease in current density with insulator thickness is seen in Figure 6.6b). Hence this thickness-dependence study experimentally demonstrates a fundamental trade-off between the figures of merit and current density (diode resistance) in $Pt/Al_2O_3/Al$ diodes. One promising strategy to tackle this trade-off may be the use of multiple AP-CVD insulator layers, as discussed in Chapter 4. The CHT approach demonstrated here will be particularly useful for optimizing the figures of merit in diodes with multiple insulator layers.

Chapter 7
Double-Insulator Thickness-Gradient Films for MIIM Diodes

7.1 Overview

A simple MIM structure where the insulator was fabricated by AP-CVD was studied in Chapters 5 and 6, but this approach can be extended to MIIM diodes. Multi-insulator diodes can help overcome the issue of large diode resistance, while improving the figures of merit, by decreasing the effective tunneling distance or enabling resonant tunneling of electrons[128]. Furthermore, investigating new insulator combinations for MIM diodes is promising to improve their FOMs. The AP-SALD system is capable of forming multi-insulators with thickness gradients. These can be investigated to identify the optimal multi-insulators thicknesses for high-FOM diodes.

In this work, double insulator thickness gradient films were introduced to enhance the figures of merit and lower the resistance over the single insulator MIM diodes, which was attributed to the difference in electron affinity of the insulators. To achieve this, aluminum oxide (Al_2O_3) and zinc oxide (ZnO) film combinations were fabricated for the first time using AP-CVD and integrated into MIIM diodes.

7.2 Experimental

This study involved the fabrication and characterization of more than 414 Pt/Al_2O_3-ZnO/Al devices, each with different Al_2O_3/ZnO thickness combinations, on one Si wafer, by employing two thickness-gradient films. The metal electrodes were deposited with the process described in Chapter 3. For the deposition of Al_2O_3 thickness gradient films, both TMA and DEZ precursors were employed. The DEZ was bubbled throughout the deposition to facilitate film nucleation at 130 °C. N_2 was bubbled through the TMA and DEZ precursors at 38 and 10 sccm, respectively, and combined with a 235 sccm N_2 carrier gas. Ammonia water (30% NH_3) was bubbled at 100 sccm and combined with a 275 sccm N_2 carrier flow. The resulting flow per outlet channel was 125 sccm. A 750 sccm flow of N_2 inert gas was used. The substrate was oscillated 20 times (40 ALD cycles) at a speed of 30 mm/s with a reactor-substrate spacing of 400-100 μm. For the deposition of ZnO thickness gradient films, the same process used in Chapter 6 was employed. 20 oscillations were applied and a 200-100 μm reactor-substrate spacing was used.

7.3 Results and discussion

Figure 7.1a illustrates the fabricated combinatorial Pt/Al_2O_3-ZnO/Al MIIM diodes. The expected energy band diagram for the Pt/Al_2O_3-ZnO/Al diode is presented in Figure 7.1b. The barrier width (insulator thickness) varies across the substrate (Al_2O_3: 2.5-12 nm, ZnO: 2.8-9.3 nm), as measured by ellipsometry.

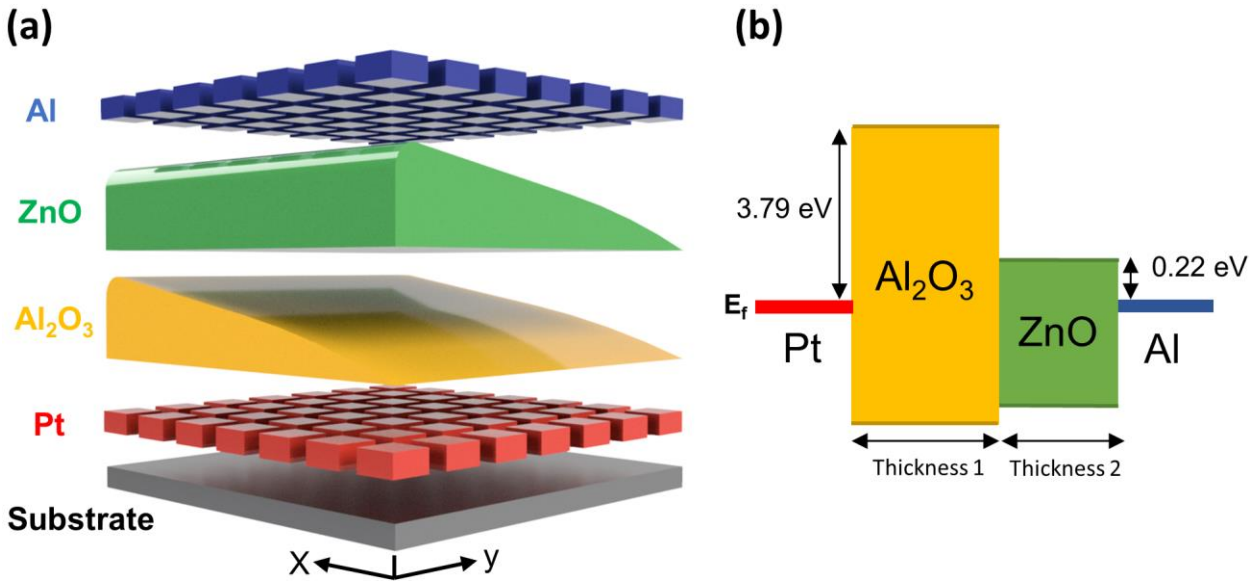

Figure 7.1. (a) Device architecture and (b) band structure of double-insulator thickness-gradient Pt/Al_2O_3-ZnO/Al diodes.

Current density-voltage (J-V) measurements were performed on the MIIM diodes to determine their figures of merit. Figure 7.2 show 3D color maps of the performance of Pt/Al_2O_3-ZnO/Al diodes. The diode results were divided into three regions according to their performance (*R_1*: Thin Al_2O_3, varying ZnO; *R_2*: Medium Al_2O_3 and ZnO; *R_3*: Varying Al_2O_3, thick ZnO). The J-V curves were asymmetrical and nonlinear for the medium-thickness diodes in region two (R_2), as shown in Figure 7.2a. These diodes had insulator thicknesses of Al_2O_3: 6.5 to 12 nm and ZnO: 4 to 7.5 nm.

In contrast, the J-V curve for diodes in R_1 and R_3 in Figure 7.2a showed low asymmetry. Figures 7.2a, b, and c show the dependence of the asymmetry, nonlinearity, and responsivity on the Al_2O_3 and ZnO thicknesses. The maximum asymmetry ratio at +1V for each diode was

calculated. A maximum asymmetry of 2580 was observed for an Al_2O_3 thickness of 7.4 nm and ZnO thickness of 4.4 nm. The maximum nonlinearity was 13.1 for an Al_2O_3 thickness of 7.4 nm and ZnO thickness of 4.4 nm. The maximum zero-bias responsivity was 12 A/W for an Al_2O_3 thickness of 7.4 nm and ZnO thickness of 3.4 nm. Therefore, this CHT study indicates that the optimum figures of merit for the Pt/Al_2O_3-ZnO/Al MIIM diode can be obtained with insulator thicknesses of 7.4 nm for Al_2O_3 and 3.4 to 4.4 nm for ZnO.

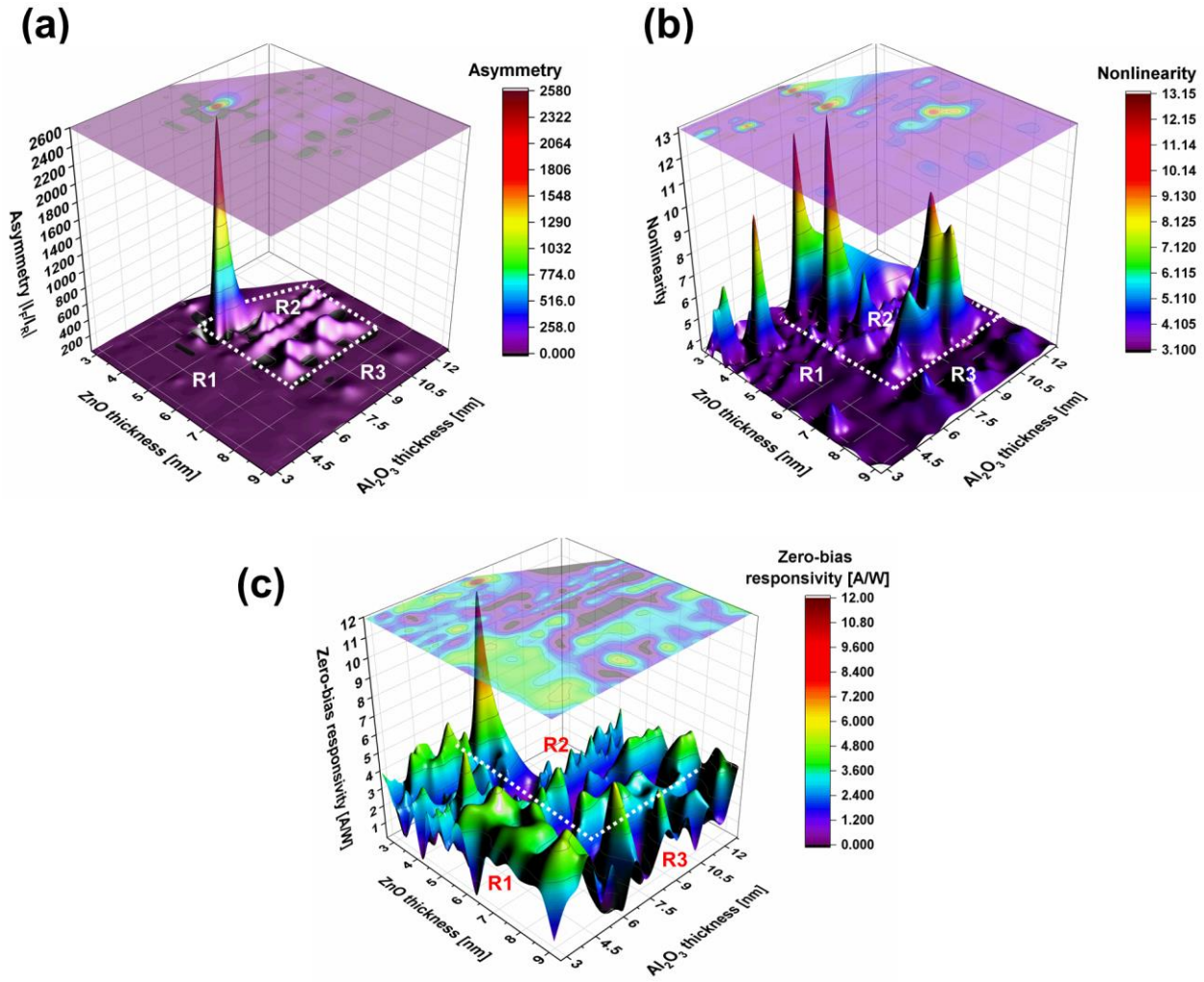

Figure 7.2. Performance of CHT Pt/Al_2O_3-ZnO/Al diodes. (a) Asymmetry, (b) nonlinearity, and (c) responsivity.

7.3.1 Conduction mechanisms

As observed in previous chapters, the types of conduction mechanisms present in a diode are expected to play an important role in the different performances of the diodes. Barrier height and insulator thickness are two of the parameters responsible for the dominance of different conduction mechanisms[5]. Here, different conduction mechanisms under forward biasing were

examined, including FNT, SE and PF, for diodes located at different positions across the substrate.

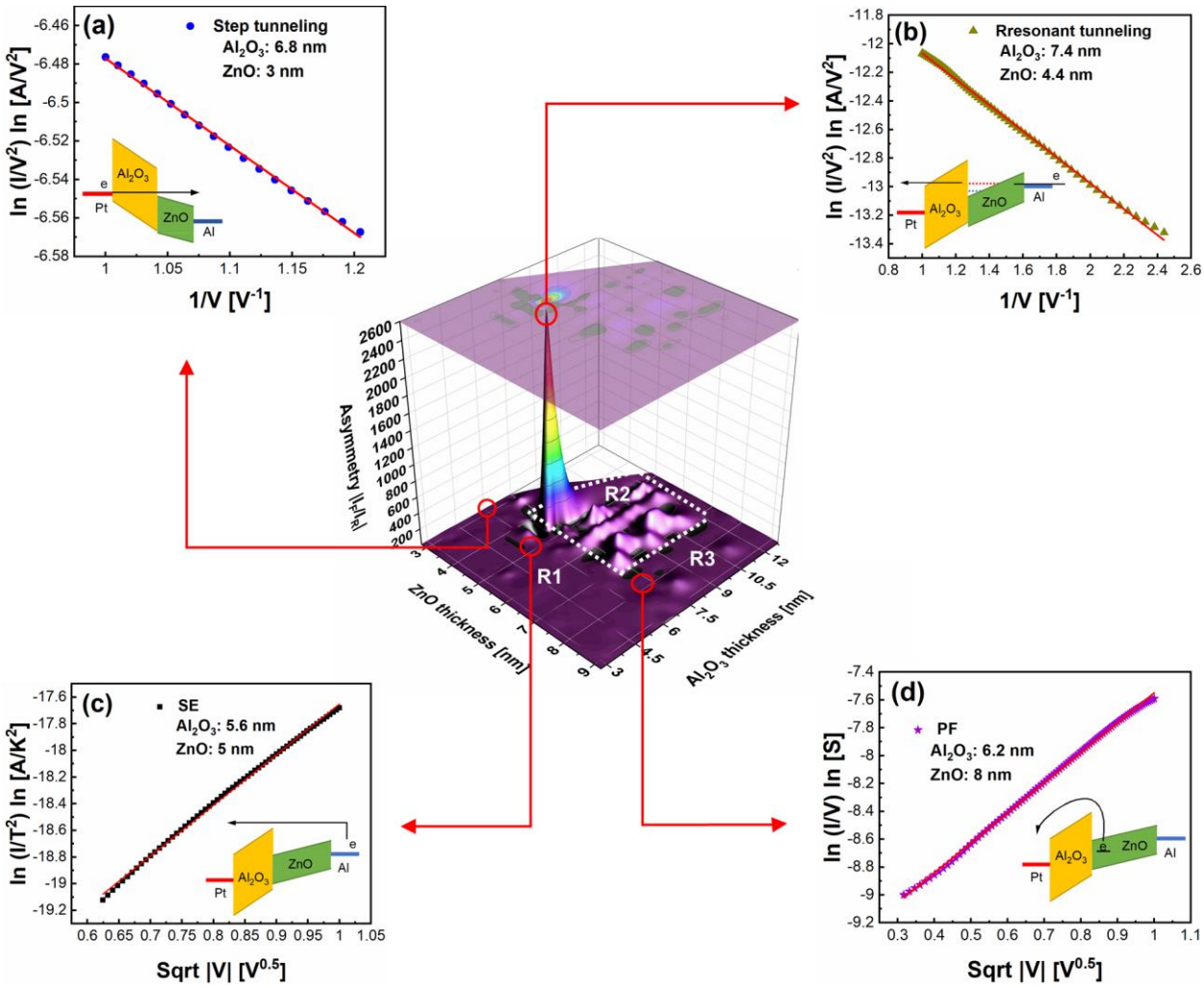

Figure 7.3. Conduction mechanisms for Pt/Al_2O_3-ZnO/Al MIIM diodes with Al_2O_3/ZnO thickness gradient films at different position across the substrate.

Figure 7.3 shows the conduction mechanisms at different locations across the substrate. The different mechanisms are attributed to the different shapes of the energy bands that result

from the different insulators thicknesses. In Figure 7.3a, the electron tunnelling occurs by step tunneling (ST). In this diode, electrons from the Pt only tunnel through the Al_2O_3 (6.8 nm thickness) then overcome the ZnO (3 nm) to reach the Al, resulting in a high electron tunneling probability and a high current density as shown in Figure 7.4a. In contrast, the forward bias current in the diode with thicknesses of Al_2O_3: 7.4 nm, ZnO: 4.4 nm, which is shown in Figure 7.3b, occurs by resonant tunneling (RT). The electrons tunnel through both of the insulators with assistance from the energy state present in the triangular quantum well formed between the two insulators. Hence this conduction mechanisms study indicates that the dominant conduction mechanism in the diodes with high figures of merit (region 2) is resonant tunneling. The domination of resonant tunneling is observed as the thickness of the higher electron affinity layer (χ of ZnO= 4.5 eV) increased, as this thickness increase leads to the formation of a wider and deeper quantum well. This is similar to the behavior observed in a Ni/NiO-Al_2O_3/Cr-Au diode when the thickness of the NiO (χ= 4.7 eV) was increased[128]. Thermal conduction mechanisms were observed to dominate for other insulator thickness combinations. The SE mechanism was dominant for a diode with thicknesses of Al_2O_3: 5.6 nm, ZnO: 5 nm, and PF was dominant for a diode with thicknesses of Al_2O_3: 6.2 nm, ZnO: 8nm. Inferior figures of merit were observed for these diodes.

In contrast to the single thickness gradient Al_2O_3 diodes presented in Chapter 6, this combinatorial MIIM diode study shows that the variation in the insulator thickness ratio (Al_2O_3: ZnO) allows altering the shape of the barriers, resulting in different conduction mechanisms. Adding a ZnO layer results in significant improvement in the FOMs by increasing the electron tunneling probability, especially for resonant tunneling.

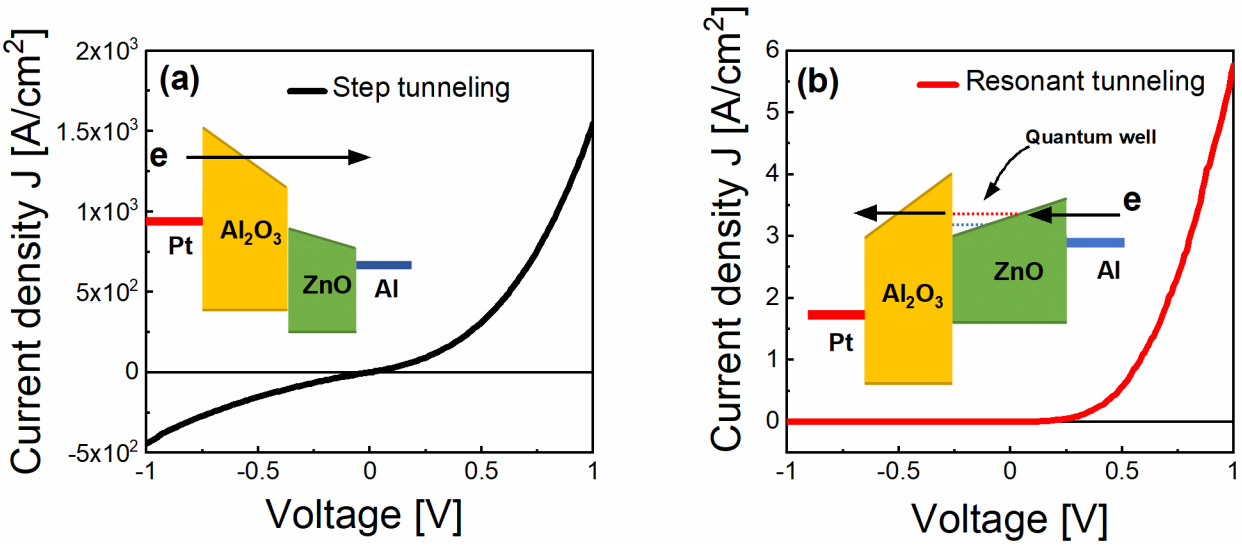

Figure 7.4. Energy band diagram of Pt/Al_2O_3-ZnO/Al diode in forward bias state: (a) step tunneling, (b) resonant tunneling.

7.3.2 Time savings provided by AP-SALD and CHT techniques

Table 7.1 compares the MIM and MIIM diodes made by PEALD and AP-SALD techniques used in this thesis, including the temperature and deposition time. In vacuum-based methods such as PEALD, it can take several hours to attain a suitable vacuum, deposit a film, and then vent the vacuum chamber to retrieve the sample. Using AP-SALD, a substrate is placed on a heated stage and a thickness gradient film is quickly deposited (e.g., in 45s for the Al_2O_3 and 2 min for Al_2O_3/ZnO gradient films). Thus, eliminating the vacuum can make the film deposition process an order of magnitude faster or more (minutes vs. hours).

The combinatorial approach affords significant gains when fabricating diodes. For example, the fabrication process used to fabricate a MIM diode takes approximately 9 hrs or 7hrs for each wafer by PEALD or AP-SALD respectively. Hence via a traditional one-thickness-at-a-

time approach, approximately 414 × 9 hrs = 3728 hrs would be required to produce 414 different MIM diodes by PAALD and 2898 hrs by AP-SALD. By utilizing thickness gradient films, the fabrication time is reduced to 161 hrs or 7 hrs for single and double thickness gradients, respectively, since 414 different thickness combinations were examined on a single wafer.

Table 7.1. Summary of fabrication processes of MIM and MIIM diodes fabricated by PEALD and AP-SALD/CVD.

Insulator deposition process	Deposition temperature	Number of diodes / batch	Number of thicknesses / batch	Deposition time				
				1st Metal Deposition	Insulator Deposition	2nd metal Deposition	Time/batch	Time for 414 thicknesses
PEALD (Chapter4) (Pt-TiO_2-NAl_2O_3-Al)	250-300	414	1	3 h	2h	4h	9 h	3728 h (5.2 months)
AP-SALD/CVD (Chapter 5) Single layer (Pt-Al_2O_3-Al)	150	414	1	3h	2 min	4h	7h and 2 min	2898 h (4 months)
AP-SALD/CVD (Chapter 6) Single thickness gradient (Pt-Al_2O_3-Al)	150	414	18	3h	45 s	4h	7h	161 h (7 days)
AP-SALD/CVD (Chapter 7) Double thickness gradient Pt/Al_2O_3-ZnO/Al	**130-150**	**414**	**414**	**3h**	**2 min**	**4h**	**7h and 2 min**	**7h and 2 min**

Time decreasing

Chapter 8
Combinatorial and High-throughput Analysis of Thin Film Encapsulation for Perovskite Solar Cells

8.1 Overview

Organic–inorganic halide perovskite solar cells (PSCs) have attracted a great deal of attention due to their excellent absorption and charge transport properties as well as their low-cost and convenient fabrication techniques[129]. These properties led to an incredible device power conversion efficiency improvement from 3.8% to over 25.2% in only a few years[130,131]. However, the most challenging issue in perovskite solar cells is the long-term stability[132,133]. Research indicates that the most significant source of external degradation in these cells is the decomposition of the perovskite after exposure to moisture and oxygen[134]. External encapsulation materials (e.g., epoxies, laminated plastics) and thin-film encapsulation (TFE) materials deposited directly onto the device stack are being investigated, as detailed in several excellent review articles, including some specific to ALD and CVD[135–137]. A PSC encapsulation layer should be pinhole- and crack-free, and dense to avoid the ingress of water. The encapsulation layer should be deposited at low temperatures to avoid damaging the PSC. ALD encapsulation is attractive since it provides conformal, pinhole-free barrier layers, but its slow speed hinders its practicality and prolonged heating and precursor exposure can damage the

underlying layers[135,138]. As a result, most TFE implementations have used ALD film thicknesses on the order of 20 nm or less and efforts have been made to use lower processing temperatures (e.g., 60°C)[135,138]. However, for prototypical encapsulation films, such as Al_2O_3, lower processing temperatures have been reported to decrease the film density, increase undesirable hydroxyl content, and increase the water vapor transmission rate (WVTR)[139,140]. AP-SALD and AP-CVD are promising alternatives to PECVD and conventional ALD. They are capable of providing pinhole-free gas barrier layers at atmospheric pressure, and the rapid nature of AP-SALD and AP-CVD (can be more than 100 times faster than conventional ALD) limits the required heating time of the perovskite and potential damage. It has been shown that TiO_2, SnO_x, and CuO_x charge-transport layers can be deposited on top of perovskite films by AP-SALD/AP-CVD at temperatures as high as 180°C[141,142]. Hence, the higher deposition rate of AP-SALD and AP-CVD enables a larger TFE processing window (temperature and thickness range) to be explored for PSCs. In this chapter, it is shown that the AP-CVD gradient thickness films developed in Chapter 6 can be used for CHT analysis of thin-film encapsulation layers for PSCs.

8.2 Experimental

Fluorine doped tin oxide (FTO) glass substrates (5 × 5 cm) were washed in a 2% aqueous extran 300 detergent, deionized water, and 2-propanol (20 min each), then, dried using a hotplate at 150 °C for 0.5 h, after which they were allowed to cool. A titanium dioxide (TiO_2) layer was prepared by dissolving a 0.1 M solution of titanium diisopropoxide bis(acetylacetonate) in 1-butanol and then spin coating three times at 4000 rpm for 10 s in a fume hood. In between each spin-coating, the samples were annealed at 125 °C for 5-10 min then allowed them to cool down

for 1 min. Organic residues were eliminated by increasing the temperature (from 125 to 450 °C), holding at 450 °C for 0.5 h, and then decreasing the temperature from 450 °C to room temperature, using ramp rates of ~15 ºC/min. The perovskite layer was made by preparing an anhydrous stock solution of 1.4 M PbI_2, 1.25 M formamidinium iodide (FAI), 0.0987 M CsI, and 0.0833 M GAI in 76:24 ratio (v/v) in DMF/DMSO solvent in a nitrogen glovebox. Then, it was passed through a 0.45 μm polytetrafluoroethylene syringe filter and stirred for 30 mins. The solution was deposited on the substrates by spin-coating at 1000 rpm for 10 s followed by 6000 rpm for 20 s in the glovebox. In the last 5 s of spin-coating, 200 μL of a 50/50 (v/v) anhydrous solution of chlorobenzene and chloroform was dispensed as an antisolvent. Immediately after spinning, the samples were annealed at 140 °C for about 0.5 h in the glovebox and allowed to slowly cool down to room temperature. For the hole transport layer, a solution of 70.0 mM Spiro-OMeTAD in chlorobenzene was prepared in the glovebox by adding 18 μL of 4-tert-butyl pyridine and chlorobenzene (60:40 v/v) and 18 μL of a 1.0 M Li-TFSI solution in acetonitrile to 1000 μL of the Spiro-OMeTAD solution. After filtering the solution through a 0.45 um polytetrafluoroethylene syringe filter, it was spin-coated at 4000 rpm for 15 s. For the deposition of Al_2O_3 films for PSCs, both TMA and DEZ precursors were employed. The DEZ was bubbled throughout the deposition to facilitate film nucleation at a lower substrate temperature of 130 °C, to prevent damage to the perovskite film. N_2 was bubbled through the TMA and DEZ precursors at 38 and 10 sccm, respectively, and combined with a 235 sccm N_2 carrier gas. The H_2O and N_2 inert gas flows were the same as for the Al_2O_3 deposited for the MIM diodes in Chapter 6.

8.3 Results and discussion

AP-CVD of an Al_2O_3 TFE, which is a prototypical TFE material,[135,136,139,143] was demonstrated on top of a perovskite solar cell stack for the first time. Spatial ALD Al_2O_3 has been reported to have a WVTR on the order of 10^{-6} g m^{-2} d^{-1} at room temperature[45]. A gradient film of Al_2O_3, was used to study TFE thicknesses up to 70 nm, a larger range than has typically been tested with conventional ALD. Thicker Al_2O_3 layers may be expected to provide better encapsulation; however, practical considerations (deposition time and cost) favor thinner layers for commercialization. Furthermore, it has been demonstrated for ALD films that the improvement in barrier properties with thickness can be sub-linear[144,145] and can show low thickness dependence[146]. Klumbies *et al*.[144] showed fast degradation for devices encapsulated with 100 nm of Al_2O_3 because of the formation of the large cracks resulting from increased film stress with thicker films[144,147]. Hence thickness-dependent studies are essential to identify optimal thicknesses. PSCs often display significant performance variability, and the combinatorial approach used here allows the influence of the TFE thickness to be studied in a single device, avoiding batch-to-batch comparisons. The variable reactor-substrate spacing method was used to deposit an Al_2O_3 film with a thickness gradient (70-40 nm) as an encapsulation layer on top of a 5×5 cm formamidinium-cesium lead iodide PSC. 60 substrate oscillations (120 cycles) and a spacing of 200-100 µm were used to deposit the gradient film. The deposition took only 5 minutes, such that no degradation of the perovskite was observed when heating the device to 130 °C for the deposition. The perovskite solar cell architecture is shown in Figure 8.1a and consisted of glass/FTO/TiO_2 (55 nm)/perovskite (315 nm)/Spiro-OMeTAD (370 nm)/Al_2O_3 (70-40 nm). The top metal electrode was omitted to avoid known

issues with iodine migration to the metal electrode[148] and to facilitate the absorbance as well as the neural network characterization discussed hereafter.

To study the effect of the larger Al_2O_3 TFE thickness on perovskite stability, PSCs with and without the Al_2O_3 TFE were placed in a humidity chamber with 60% RH at room temperature. The absorbance of the PSC was measured at different positions across the device (corresponding to different TFE thicknesses) after various durations in the humidity chamber. Figures 8.1b and c show the absorbance versus H_2O exposure time at wavelengths of 500 and 630 nm, respectively. A clear trend is seen after 25 h, where the absorbance drops more significantly for locations where the TFE is thinner, indicating more perovskite degradation. The reduction in absorbance (and hence degradation of the perovskite) is greatest for the device with no Al_2O_3 TFE. The photoluminescence (PL) of the PSC (excitation at 680 nm) was also measured after 28 h at various locations across the device with the Al_2O_3 thickness gradient TFE and for the device without a TFE, as shown in Figure 8.1d. As expected, the PL measurements show that the PL intensity of the perovskite peak at 825 nm decreases with decreasing Al_2O_3 TFE thickness, indicating that the perovskite degrades faster when the TFE is thinner. This is consistent with a previous study of ALD Al_2O_3 barrier films for OLEDs[144]. The smaller peak at 835 nm is attributed to the TiO_2 film[149,150] in the device stack.

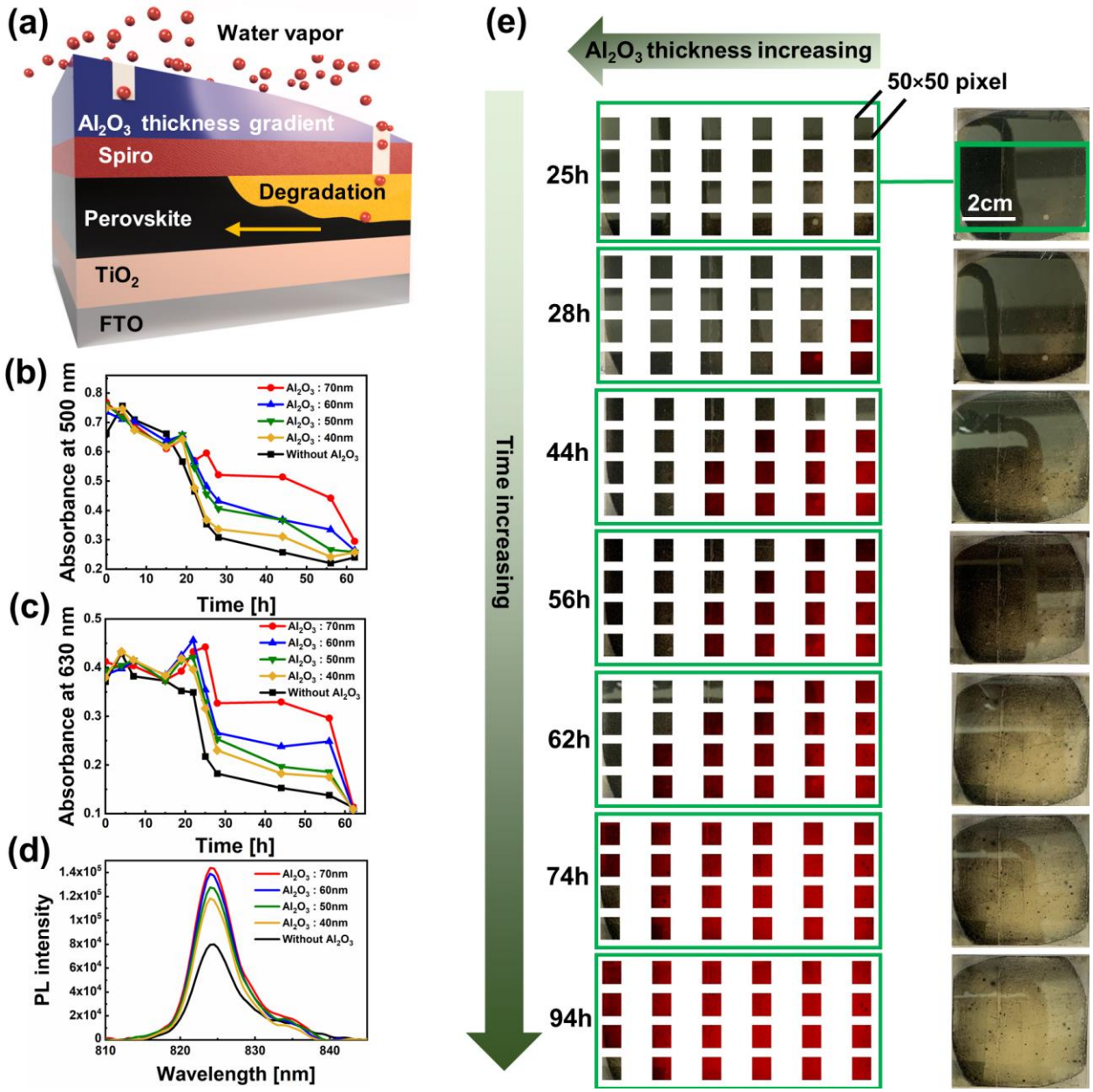

Figure 8.1. CHT study of perovskite solar cell thin film encapsulation. (a) Perovskite solar cell architecture with Al_2O_3 gradient TFE. (b), (c) Plots of PSC absorbance vs time at different positions across the PSC (corresponding to different TFE thicknesses) and for a PSC with no TFE at wavelengths of 500 nm and 630 nm. (d) PL spectra of the PSCs at 28h. (e) Spatially resolved classification of the PSC degradation by a convolutional neural network. Red coloration indicates perovskite degradation. The onset of PSC degradation is observed to occur at different times for different TFE thicknesses.

For CHT study of the PSCs, a simple convolutional neural network (CNN) was developed by collaborator Alexander Jones to determine the effectiveness of the Al_2O_3 TFE. CNNs have been used to perform many image processing tasks in materials science, such as detecting 2D materials in microscope images[151], improving X-ray diffraction test speed[152], and predicting chemical properties[153]. CNNs are designed to mimic the human eye in function, recognizing how colors, shapes and edges build to form a complete picture[154], which makes them robust to changes in lighting or image orientation when well trained. In our work, the effectiveness of the TFE is directly correlated with the rate of decay of the perovskite layer. As per Figure 8.1a, as the perovskite reacts with water, lead iodide is formed, turning the perovskite from black to translucent yellow. In this case, the CNN need only to identify the color of the input image, and identify any abrupt edges, such as cracks or holes in the film in order to classify the image as either “degraded”, “intact”, or “no film” present.

Images of the PSCs were taken at various intervals, from various angles and under different light conditions over the ~100 hours it took for the films to degrade in the humidity chamber. These were then subdivided into smaller 50×50-pixel images, as can be seen in Figure 8.1e, which serve as the input to the CNN. This subdivision serves three purposes, firstly it boosts the training data size by several orders of magnitude, secondly it simplifies each input sample so a smaller and faster CNN can be used, and thirdly it spatially resolves the degradation of the perovskite layer. It is the third advantage that allows us to compare and evaluate the various Al_2O_3 TFE thicknesses. The colors are coded according to the three possible predictions provided by the neural network. A red overlay is placed on a 50×50-pixel image if the

probability that the sub-section is degraded is greater than the other two possibilities (there is no correlation to the degree of degradation). In Figure 8.1e, the Al_2O_3 TFE thickness increases from right to left. After 25 h H_2O exposure time, a clear hole appeared in the area with thinner Al_2O_3, indicating that water had penetrated through the TFE and Spiro-OMeTAD into the perovskite layer. After 28 h the CNN identified that the perovskite started to degrade wherever the Al_2O_3 was thinnest, as indicated by the red coloration in the pixelated images. This is consistent with the lower absorbances and PL intensity for Al_2O_3:40 nm in Figure 8.1b,c, and d. The degradation, which is indicated in red, progresses from parts of the device with thinner TFE to thicker TFE with increasing H_2O exposure time, as shown from 28 h to 94 h. The insets in Figure 8.1e shows the PSC at different H_2O exposure times. It is seen that the degradation begins earlier for the bottom row of pixels than the top row. This is attributed to the presence of some thickness variation in the perpencidular direction, which was shown in Figure 6.2g in Chapter 6. The thickness gradient across the top of the sample appears to be slightly thicker than the gradient across the bottom.

The superior performance of the thicker TFE suggests that the thicker AP-CVD Al_2O_3 maintains its compactness and is free of stress-induced cracking[144], at least up to the 70 nm thickness examined here. This is consistent with the uniform refractive index (1.78-1.8) measured for the 70-40 nm thickness range (Figure 10.8) in Chapter 10, as well as microscope images of a 75-45 nm Al_2O_3 thickness gradient film in Figure 8.2, which showed no cracks for thicknesses up to 75 nm. In contrast, the micrographs indicated the presence of some film

regions with pinholes at the 45 nm gradient thickness and to a lesser extent at 55 nm, consistent with the faster degradation observed.

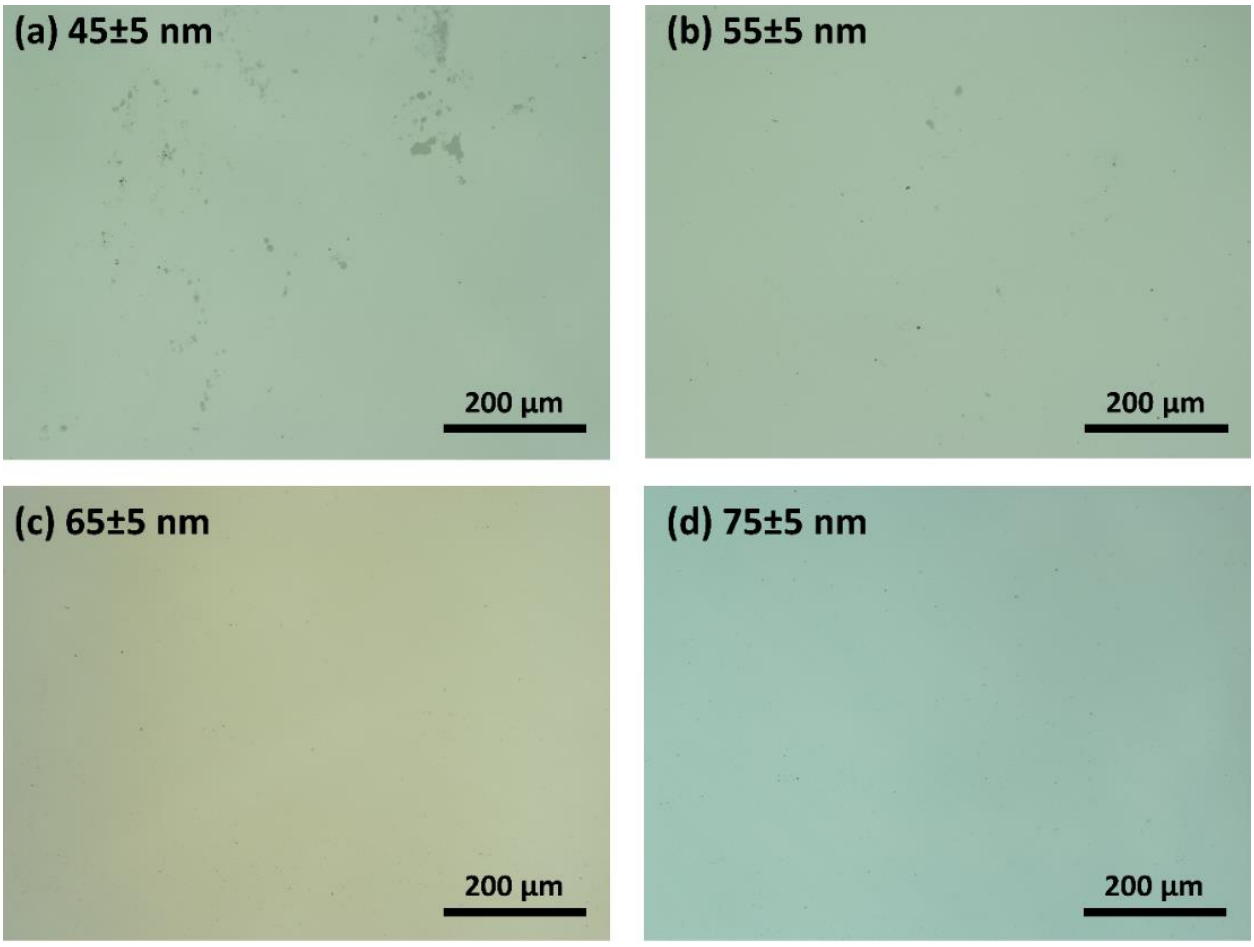

Figure 8.2. Microscope images of a 75-45 nm Al_2O_3 thickness gradient film taken at thickness locations of (a) 45 nm, (b) 55 nm, (c) 65 nm, and (d) 75 nm. No cracks are observed in the film.

Table 8.1 details some previous AlO_x TFE studies for PSCs[138,139,155–157], including the deposition time, temperature, TFE thickness, and degradation time. While these studies reported longer degradation times for similar humidity conditions to those examined here, they make use

of conventional ALD to deposit the TFE. As shown in Table 8.1, the deposition rates and deposition times (e.g., >100 minutes) associated with ALD are impractical for manufacturing TFE for PSCs. Here AP-CVD of an Al_2O_3 TFE was demonstrated on top of a PSC stack for the first time. While stability optimization of the AP-CVD Al_2O_3 films is needed in the future, the short deposition time (5 min) avoids damage to the perovskite layer and is compatible with large-scale manufacturing.

These nanoscale film thickness gradients will provide a useful platform to further optimize the thicker TFE layers that are practical with AP-SALD/CVD. Al_2O_3 has also been a key component in TFEs based on oxide[143] and organic-inorganic[136,139,158] multilayers/nanolaminates. The gradient films will be particularly useful for optimizing the thicknesses of multiple oxide films simultaneously, although the complexity, cost, and industrial practicality of the nanolaminate films should be kept in mind.

Table 8.1. Summary of some previously reported ALD AlO_x encapsulation films.

ALD Oxidant	GPC [A/cycle]	Deposition rate [nm/s]	Deposition time [min]	Deposition temperature [°C]	Final thickness [nm]	Humidity condition RH (%)	Degradation time [h]	Ref
H_2O	0.64	0.002	120	60	16	80	2256	[138]
H_2O	4	0.005	167	100	50	20-60	500	[159]
H_2O	NA	NA	NA	75	NA	50	7200	[160]
H_2O	1	0.008	100	100	50	65	960	[157]
H_2O	1.1	0.0035	100	90	21.5	50	300	[139]
APCVD: H_2O	**3.3-5.8**	**0.13-0.23**	**5**	**130**	**40-70**	**60**	**28-94**	**This work**

Chapter 9
Conclusions and Future work

This thesis has presented several novel dielectric film fabrication strategies to improve the manufacturability, optimization, and performance of MIM diodes.

In Chapter 4, a new PEALD method for doping AlO_x with nitrogen, which uses a nitrogen plasma, was demonstrated and resulted in films with high N content (11.5 at%). The $NAlO_x$ films, as well as $NTiO_x$ films deposited in a similar manner, were employed in Pt/TiO_x-$NTiO_x$/Pt and Pt/TiO_x-$NAlO_x$/Pt MIIM diodes and compared to undoped Pt/TiO_x/Pt and Pt/TiO_x-AlO_x/Pt diodes. While doping the insulator layers is expected to induce both defects in the insulators and affect the barriers at the insulator interfaces, a study of the conduction mechanisms suggests that changes to the diode performance are mainly due to the introduction of defects that facilitate alternate conduction mechanisms, including PF and TAT. A Pt/TiO_x-$NTiO_x$/Pt diode showed dominant PF conduction at the majority of forward biases and SE at reverse bias, resulting in an asymmetry of 28.6, nonlinearity of 3, and zero-bias responsivity of 13.5 A/W. One of the advantages of fabricating TiO_x-$NTiO_x$ diodes is their simplicity compared to previous multi-insulator diodes that contain different insulator materials. There is no need for chamber purging and cleaning before depositing the second doped insulator layer. The best performance was obtained with a Pt/TiO_x-$NAlO_x$/Pt diode. TAT and FNT mechanisms were dominant at forward bias while SE remained dominant in the reverse direction at the Pt/TiOx interface. This asymmetry in conduction mechanisms resulted in a higher asymmetry (8.76×10^3), nonlinearity of 4, and higher zero-bias responsivity (up to 36.8 A/W) than has been previously

reported. Notably, these improvements in the figures of merit were obtained without an undesirable increase in the diode resistance. The very low diode resistance of 36 Ω that was achieved for the thinner Pt/NTiO$_x$-NAlO$_x$/Al diode, along with a nonlinearity of 3.5 and zero bias responsivity of the 1.7 A/W, is promising for energy harvesting application. Thus, this work demonstrates the use of defect engineering to improve the performance of MIIM diodes. The capacitance may be further reduced in the future by doping lower dielectric insulators such as ZnO, HfO$_x$, and TaO$_x$ instead of the TiO$_x$ used in this work. Different dopants, dopant concentrations, and insulator thicknesses also warrant investigation.

In Chapter 5, Pt/Al_2O_3/Al MIM diodes were fabricated where the 6 nm thick insulating Al_2O_3 films were deposited by a rapid, scalable, open-air technique. An AP-SALD system operated in CVD conditions was used to produce MIM diodes with high-quality, pinhole-free insulator films more rapidly than by conventional PEALD. For MIM diodes fabricated by AP-CVD, the dominant conduction mechanisms were found to be PF at low bias voltages and FNT at high voltage biases. For MIM diodes fabricated with PEALD Al_2O_3 films, SE and FNT were the dominant conduction mechanisms at low and high bias voltages respectively. The dominance of PF conduction in the AP-CVD diodes is attributed to a higher concentration of hydroxyl groups in the films, which can act as electron traps. The AP-CVD diodes were found to have lower barrier heights, which is attributed to the use of a thermal rather than plasma process, as observed previously. The lower barrier heights result in different diode performance, namely a lower turn on voltage, as well as better asymmetry, combined with a reduction in the maximum nonlinearity and responsivity figures of merit. A simple MIM structure was studied, but this approach can be extended in the future to diodes with multiple insulator layers as studied in

Chapter 7. Additional related applications to which this scalable AP-CVD technique should be applied in the future include resistive switching memories[161] and metal-insulator-semiconductor diodes[162–164]. While vacuum and lithography techniques were still used to deposit the metal electrodes and pattern the devices, by depositing the crucial insulator layer using a rapid, scalable, open-air method, this work represents an important step towards cost-effective, scalable manufacturing of quantum devices.

Chapter 6 reported on the production of thin films with nanoscale thickness gradients in the open-air by spatially varying the CVD rate across a substrate. ZnO and Al_2O_3 films were deposited with nm-scale thickness gradients (including sub-10 nm films) in as little as 45 s. The GPCs were observed to vary from as little as 0.23 nm/cycle to as much as 1.2 nm/cycle across the substrate, providing precise control over film thickness at different substrate locations. The achievable GPC range can be increased in the future and the technique can be applied to deposit a range of semiconductors, insulators, and metals that are compatible with similar ALD and CVD methods. Rapidly printed Al_2O_3 films with thickness gradients were used to perform CHT studies of quantum-tunneling MIM diodes. An Al_2O_3 film with thickness varying from 10 to 2.5 nm was used to test 360 diodes with 18 different insulator thicknesses on a single substrate. No other open-air technique currently exists to produce a sub-10 nm gradient Al_2O_3 film such as this, and this work represents a significant advancement compared to previous studies that examined a limited number of insulator thicknesses. The diode figures of merit were strongly influenced by the Al_2O_3 thickness and the best diode performance was found for a larger thickness than reported previously (6.5 to 7 nm), for which the asymmetry, nonlinearity, and

responsivity were 78, 11, and 5.5 A/W respectively. This CHT study also experimentally highlighted the fundamental trade-off between the figures of merit and diode resistance in a Pt/Al_2O_3/Al diode.

In Chapter 7, the thickness gradient work was extended by fabricating double-insulator Pt/Al_2O_3-ZnO/Al diodes where Al_2O_3 and ZnO gradient films were rapidly printed using the AP-SALD system. An Al_2O_3 film with thickness varying from 2.5-12 nm and ZnO film with thickness varying from 2.8-9.3 nm were used to test 414 diodes with 414 different insulator thicknesses on a single substrate. To our knowledge, more Al_2O_3/ZnO thickness-dependence data is obtained from this single CHT wafer than all previous experimental reports combined. The diode figures of merit were strongly influenced by the Al_2O_3/ZnO thickness, and the best diode performance was found for a thickness of Al_2O_3: 7.4 nm and ZnO: 3.4-4.4 nm, for which the asymmetry, nonlinearity, and responsivity were 2580, 13.1, and 12 A/W respectively. The dominant conduction mechanisms were found to vary across the substrate and depend on the Al_2O_3/ZnO thickness. Both thermal activation mechanisms and electron tunneling mechanisms were observed in the devices. The highest figures of merit were observed when resonant tunneling was dominant. This work represents a significant advancement compared to previous double-insulator MIIM diode studies, as different conduction mechanisms are observed at once. This CHT study is promising to be applied to different materials combinations for rapid investigation of the optimal thickness ratio required for electron tunneling-based devices.

In Chapter 8, the CHT approach was applied to another device to demonstrate its usefulness. An Al_2O_3 encapsulation film was deposited by AP-CVD on a PSC stack for the first

time. A 70-40 nm thickness gradient was employed on top of a 5×5 cm PSC. Deposition of these thicknesses would be prohibitively slow with conventional ALD. In contrast, AP-CVD is roll-to-roll compatible and the rapid nature of the spatially varying CVD technique enabled deposition of the TFE without causing degradation of the underlying perovskite film. The degradation timescale of the PSC in a humid environment, as characterized by spatially resolved absorbance and PL measurements, was observed for multiple TFE thicknesses on a single substrate. A high-throughput method using CNNs was used to analyze the Al_2O_3 TFE, which identified the areas of the perovskite that had degraded, and therefore the efficacy of the protective layer. By constantly analyzing the visual characteristics of the film, the point at which the film degrades was identified at various locations on the device. From this CHT study it can be concluded that Al_2O_3 TFEs deposited by rapid, open-air AP-CVD slow water-induced degradation, and that the effectiveness of the TFE increases with thickness, at least up to 70 nm, as no stress-induced film cracking was observed. Thicker Al_2O_3 TFEs, both single and multilayer, can be optimized in the future, but the impact of a longer TFE deposition on the cost and perovskite stability would need to be considered. The nanoscale thickness gradient films introduced in this work can be used to optimize different device architectures (e.g., different perovskite materials and TFEs) and measure different device properties (e.g., TFE water vapor transmission rates) in the future. More generally, the nanoscale film thickness gradients can be used for CHT studies of a wide range of devices, such as solar cells, LEDs, flexible electronics, and batteries, among others.

Chapter 10

Appendix

10.1 Appendix A: Metal-insulator-insulator-metal diodes with responsivities greater than 30 A/W based on ditrogen-doped TiO_x and AlO_x insulator layers.

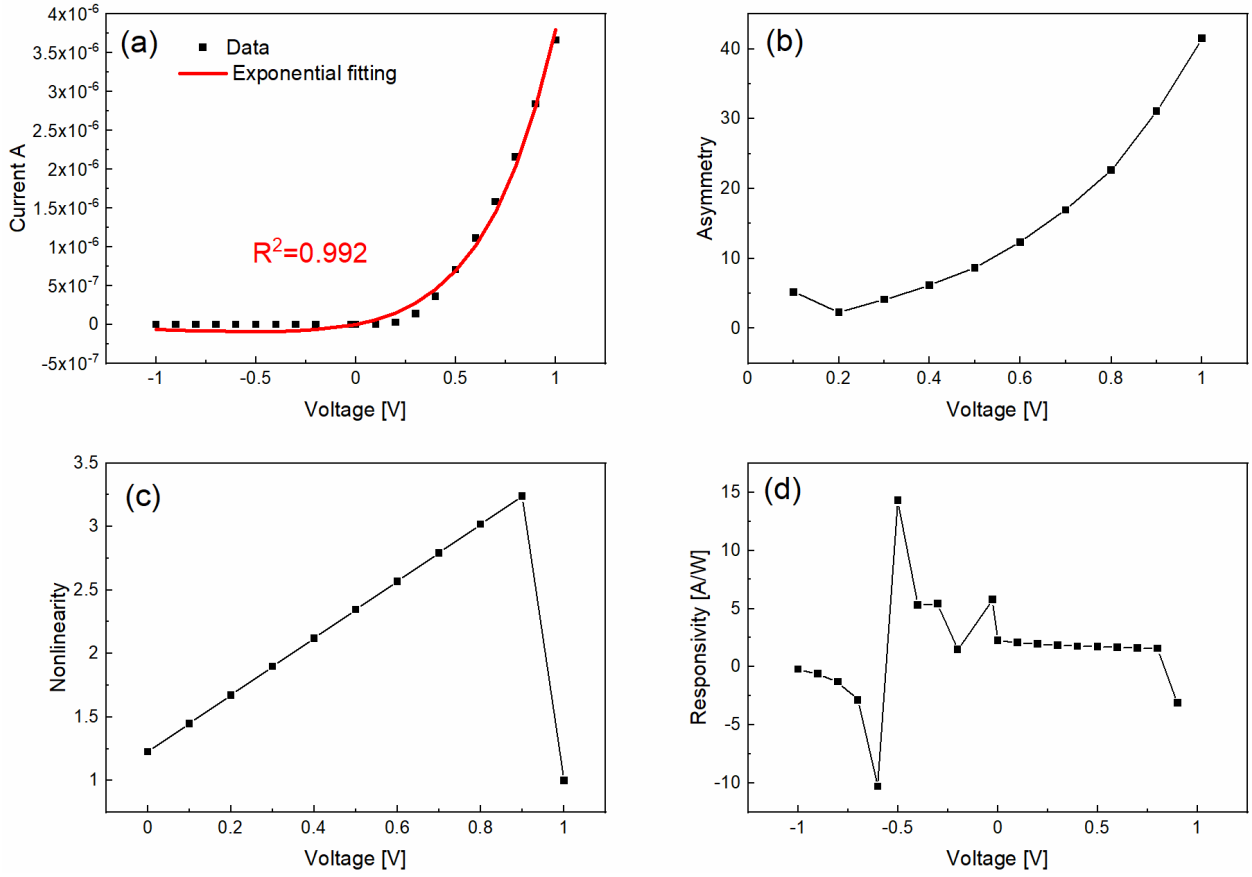

Figure 10.1. (a) Exponential fitting of I-V data for a Pt/TiO_x-NAlO_x/Pt diode, as reported in Ref[75], with R^2=0.992. (b) Asymmetry, (c) nonlinearity, and (d) responsivity calculated from the fitted data.

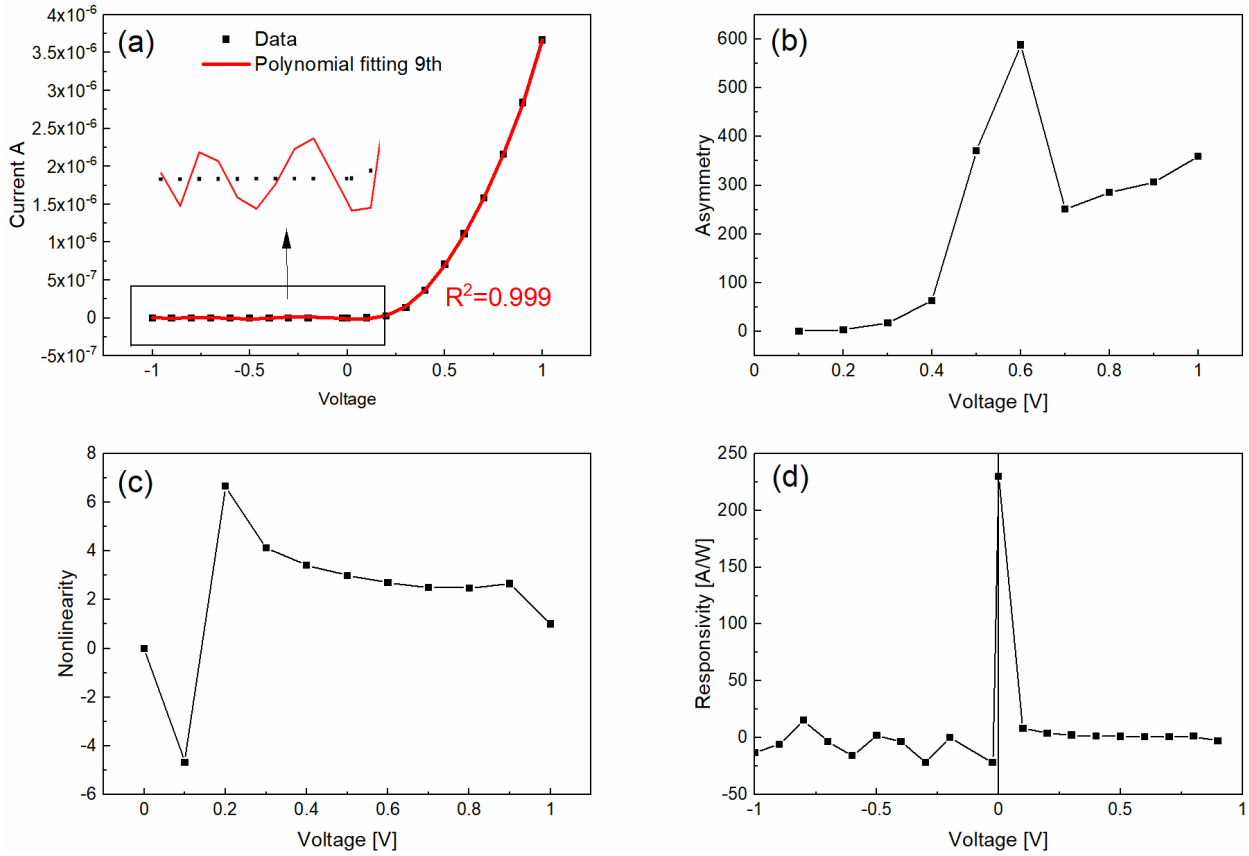

Figure 10.2. (a) 9th order polynomial fitting of I-V data for a Pt/TiO_x-$NAlO_x$/Pt diode, with R^2=0.999. Poor fitting of the data is observed for negative bias voltages. (b) Asymmetry, (c) nonlinearity, and (d) responsivity calculated from the fitted data.

10.2 Appendix B: Quantum-tunneling metal-insulator-metal diodes made by rapid atmospheric pressure chemical vapor deposition

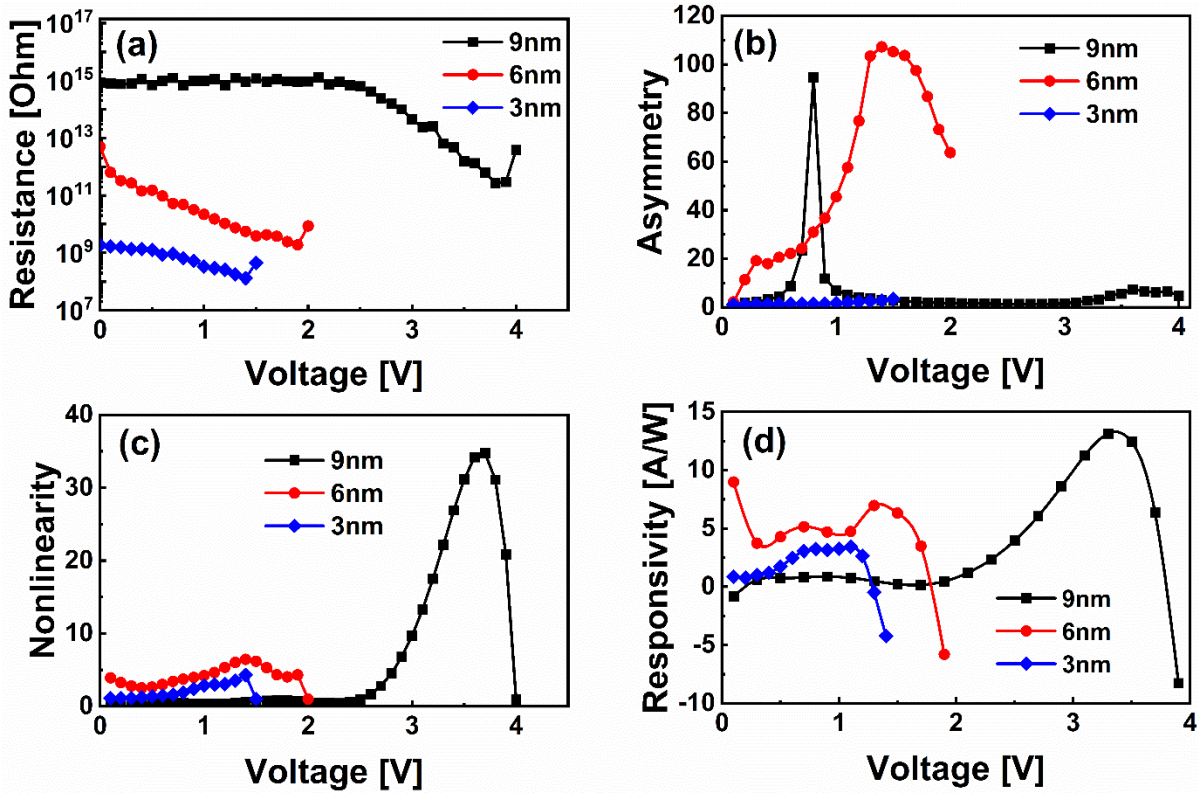

Figure 10.3. Figures of merit for Pt/Al_2O_3/Al MIM diodes with different Al_2O_3 thicknesses, including the (a) resistance, (b) asymmetry, (c) nonlinearity, and (d) responsivity.

The zero-bias resistance of the diode increases as the insulator thickness is increased, as shown in Figure 10.3a. The I-V curves show asymmetrical and nonlinear behavior for the thicker diodes with insulator thicknesses of 6 and 9 nm, as shown in Figures 10.3b,c. In contrast, the I-V curve for the diode with the 3 nm Al_2O_3 layer shows little asymmetry and nonlinearity. The turn-on voltage (TOV) increases from 0.7 V and 1.4V for the 3 nm and 6 nm diodes, respectively, to

3.6 V for the 9 nm diode. A voltage of 1.5 V is used to compare the figures of merit of the diodes because it was the maximum voltage at which the 3 nm diodes could be safely operated. The 6 nm diode shows the highest asymmetry at 1.5 V in Figure 10.3b, reaching a value of 106, compared to an asymmetry of approximately 4 for the 9 nm and 3 nm diodes. The nonlinearity at 1.5 V in Figure 10.3c is 2, 6, and 1.1 for the diodes with 3 nm, 6 nm, and 9 nm of Al_2O_3 respectively. The responsivity at 1.5 V is also highest for the 6nm diode. It shows a responsivity of 6.3 A/W, compared to values of 0.04 A/W and -4 A/W for the 9 nm and 3 nm diodes, respectively.

10.3 Appendix C: Nanoscale film thickness gradients printed in open air by spatially varying chemical vapor deposition

Figure 10.4. Schematic representation of a tilted AP-CVD reactor head placed above a substrate. By adjusting the reactor-substrate spacing along the length of the head, a film thickness gradient can be obtained.

Here, a simulation study of the variable reactor-substrate spacing approach was presented using Comsol Multiphysics. Figure 10.4 shows a tilted AP-CVD reactor head, in which the x- and y-axis are placed along the width and the length of the head, respectively. In order to treat the system in a 2D configuration, different cross-sections of the AP-CVD reactor head that are perpendicular to the y-axis were considered. Such planes can be schematically represented in Figure 10.5, with the reactor-substrate gap (h_{gap}) continuously varying along the y-axis.

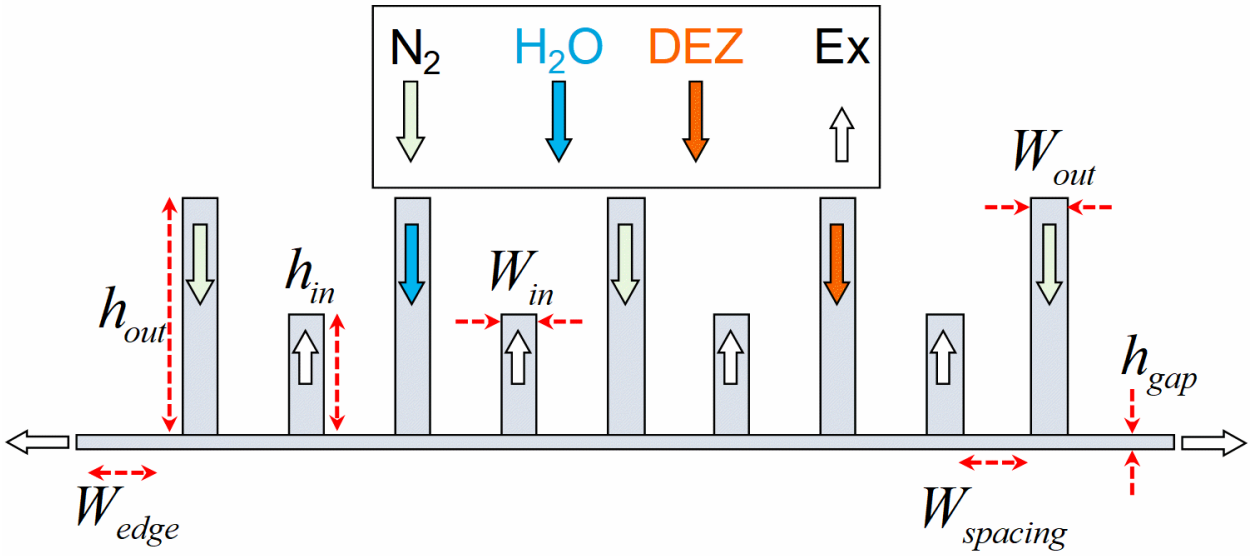

Figure 10.5. Geometry of the gas flows in the AP-CVD reactor head used in this work. The descriptions and values of the parameters indicated here are shown in Table 10.1 below. The inset rectangle with arrows explains the color code used to describe the directions of different gas flows.

Table 10.1. Parameters used for the 2D Comsol Multiphysics simulation.

Symbols	Description	Value (unit)
h_{gap}	Distance between the injection head and the substrate	50 – 270 (μm)
W_{out}	Width of the precursors and nitrogen outlets	0.5 (mm)
W_{in}	Width of the exhaust inlets	0.5 (mm)
h_{out}	Height of the precursors and nitrogen outlets	3.0 (mm)
h_{in}	Height of the exhaust inlets	1.5 (mm)
$W_{spacing}$	Distance between gas channels	0.8 (mm)
W_{edge}	Distance from the last nitrogen inlets to the edges	2.0 (mm)
T_{sub}	Substrate temperature	200 (°C)
[DEZ]	Concentration of DEZ at the top of the DEZ outlets	0.1 (mol/m^3)
[H_2O]	Concentration of H_2O at the top of the H_2O outlets	0.1 (mol/m^3)
M_{H_2O}	Molar Mass of H_2O	18.0153 (g/mol)
M_{DEZ}	Molar Mass of DEZ	123.5 (g/mol)
$f_{H_2O}^{outlet}$	Flow rate of H_2O containing gas at each H_2O outlet	150 (sccm)
f_{DEZ}^{outlet}	Flow rate of DEZ containing gas at each DEZ outlet	150 (sccm)
$f_{N_2}^{outlet}$	Flow rate of N_2 at each N_2 outlet	150 (sccm)
D	Diffusion coefficient of precursors in N_2	2×10^{-5} (m^2/s)

In practice, AP-CVD involves several gases including nitrogen, water vapor, precursor (e.g., diethylzinc, DEZ) vapor, as well as by-product gases. It is thus quite complex to access the exact physical properties of the gas mixtures in different regions. Nevertheless, the precursors

and by-product gases are largely diluted in nitrogen. Therefore, for the sake of simplicity, the physical properties of the mixtures such as viscosity were assumed, mass density, specific heat, thermal conductivity are identical to that of nitrogen, which is the carrier gas and thus the most abundant species. Information related to the diffusion coefficient of DEZ in N_2 is lacking, therefore this value is approximated in the range of the diffusion coefficient of H_2O in N_2. Figure 10.6a,b show the concentration profiles of DEZ and H_2O at the substrate surface, as well as the corresponding 2D graphs of DEZ and H_2O in the gas phase inside of the reactor head, for two values of the AP-CVD reactor head/substrate gap: 100 µm and 230 µm. In the case of a small gap, i.e. 100 µm, the DEZ and H_2O are effectively separated. In contrast, they are not well separated in the case of the larger gap in Figure 10.6b. The DEZ and H_2O concentration profiles are broader and overlap in the middle part, consistent with a CVD reaction between the precursor and reactant.

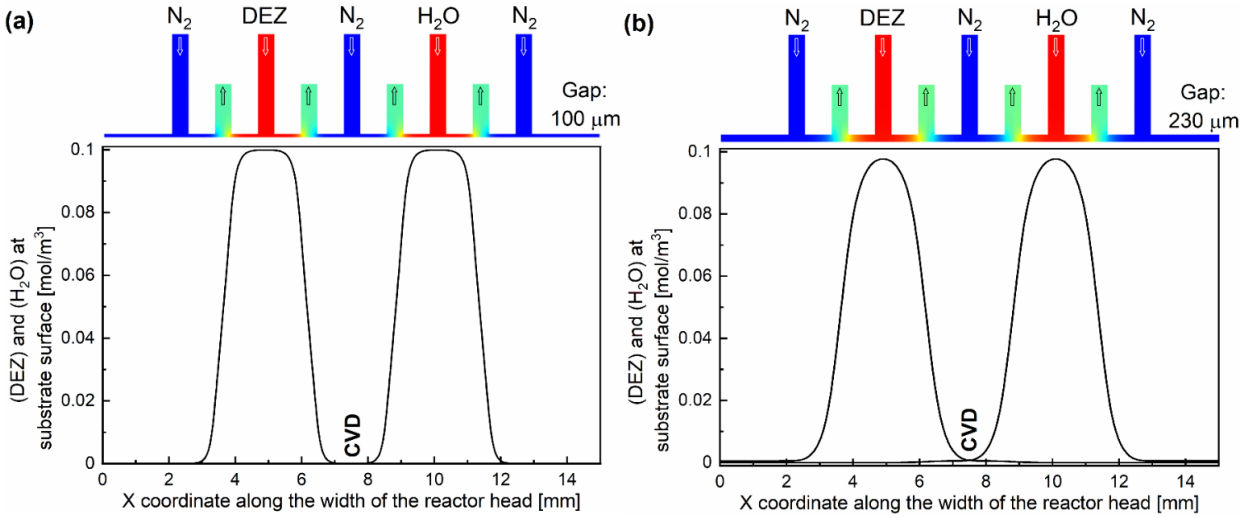

Figure 10.6. DEZ and H_2O concentration profiles at the substrate surface for two values of the AP-CVD reactor-substrate gap: (a) 100 μm and (b) 230 μm, respectively. The corresponding 2D graphs represent DEZ and H_2O in the gas phase inside of the reactor head.

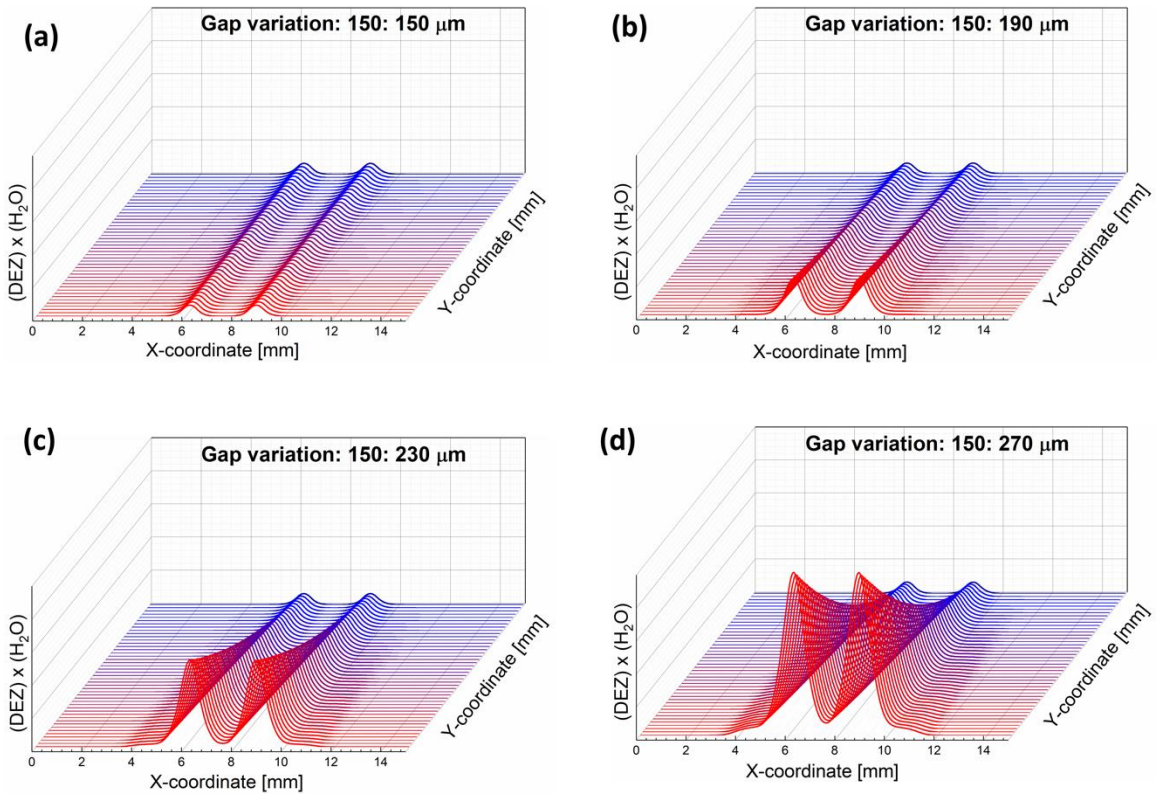

Figure 10.7. Product of DEZ and H_2O concentration at the substrate surface (15 mm×50 mm) for four cases: (a) non-tilted AP-CVD reactor head with a constant gap of 150 μm, and tilted heads with the gap variations of: (b) 150-190 μm, (c) 150-230 μm and (d) 150-270 μm. The scale of the z-axis corresponding to the intensity of the product is kept constant for all cases.

Now if consider a continuous variation of the reactor-substrate gap along the y-axis, as shown in Figure 10.4, the extent of the AP-CVD reaction can be qualitatively represented by the product of the DEZ and H_2O concentrations co-existing at the substrate surface. Figure 10.7 shows the simulation result of the [DEZ]× [H_2O] product for the case of a constant gap (150 μm) and different gap tilts (150-190, 150-230 and 150-270 μm). It can be clearly seen that the mixing

continuously increases from the side with the small reactor-substrate spacing to the side with the large gap, and that the intensity of the mixing is greater when the reactor head is more tilted.

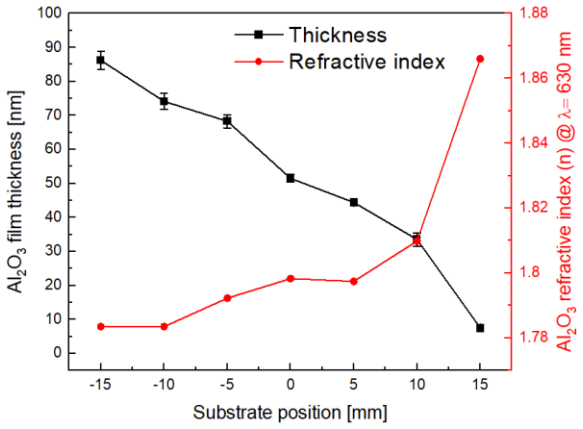

Figure 10.8. Refractive indices of a gradient Al_2O_3 film with an 86-7 nm thickness variation measured along the gradient.

10.4 Appendix D: MATLAB codes for conduction mechanisms calculations

```
%script gets I-V data and produces FOMS
clear
close all
clc
%
% directory=dir ('file name.xlsx');
% files=extractfield(directory,'name')';
files=1;

for i=1:1
 data=xlsread('kissan.xlsx');
 I=data(:,1)'; %Current
 V=data(:,2)'; %Voltage

 diodeIV{i}=[V;I]';

end


save('data.mat','diodeIV')


% CURVE FITTING
close all
clc

load('data.mat')
for i=1:length(files)
 %
 % i=68
 V=diodeIV{i}(:,1);
 I=diodeIV{i}(:,2);


 % % % smoothing Spline
 ft = fittype( 'smoothingspline' );
 % % ft = fittype( 'exp2' );
 opts = fitoptions( 'Method', 'SmoothingSpline' );
 opts.SmoothingParam = 0.9999;
 [f,gof,output]=fit(V,I,ft,opts);

 vstep=0.01;
%  vstep=V(2)-V(1);

 Vfit=(-1:vstep:1);
 Vzero=find(Vfit==0); %find 0 point
```

```
 Vfit=[Vfit(1:Vzero-5) Vfit(Vzero+5:end)];


 Ifit=f(Vfit)';

 % % % plot IV curve
 fig1=figure;
 hold on
 plot(Vfit,Ifit,'LineWidth',2) %fitted data
 plot(V,I,'*') %actual data
 title('I-V Curve')
 ylabel('Current [A]')
 xlabel('Voltage [V]')
 legend('Fitted curve','Measurement','Location','Northwest')
 hold off

 fitIV{i}=[Vfit',Ifit'];

end
save('fitIV.mat','fitIV')

% close all
% clear
% clc
%


% % % %CONDUCTION MECHANISM
load('fitIV.mat')
T=300^2;
for i=1:1

 halfway=length(fitIV{i})/2;

 Vrev=flip(fitIV{i}(1:halfway,1));
 Irev=flip(fitIV{i}(1:halfway,2));

 Vfor=(fitIV{i}(halfway+1:end,1));
 Ifor=fitIV{i}(halfway+1:end,2);


 FN{i}(:,1)=((1./Vrev));
 FN{i}(:,2)=real(log(Irev./(Vrev.^2)));
 FN{i}(:,3)=((1./Vfor));
 FN{i}(:,4)=real(log(Ifor./(Vfor.^2)));

 SE{i}(:,1)=-sqrt(abs(Vrev));
 SE{i}(:,2)=real(log(Irev/T));
 SE{i}(:,3)=sqrt(abs(Vfor));
 SE{i}(:,4)=real(log(Ifor/T));
```

```
 PF{i}(:,1)=-sqrt(abs(Vrev));
 PF{i}(:,2)=real(log(Irev./Vrev));
 PF{i}(:,3)=sqrt(abs(Vfor));
 PF{i}(:,4)=real(log(Ifor./Vfor));

 %trap assisted tunneling
 TAT{i}(:,1)=(1./(Vrev));
 TAT{i}(:,2)=real(log(Irev));
 TAT{i}(:,3)=(1./Vfor);
 TAT{i}(:,4)=real(log(Ifor));
end

save('conductiondata.mat','fitIV','SE','PF','FN','TAT')
%


%PLOT
for i=1:length(fitIV)
 close all

 %ploting of IV curve
 subplot(3,2,1)
 plot(fitIV{i}(:,1),fitIV{i}(:,2))
 ylabel('Current [A]')
 xlabel('V')
 title(['IV diode #',num2str(i)])
 hold on
 plot(diodeIV{i}(:,1),diodeIV{i}(:,2),'rx');
 legend('fitted','measured')


 %%%plotting of FN curve
 subplot(3,2,2)
 plot(FN{i}(:,1),FN{i}(:,2))
 hold on
 plot(FN{i}(:,3),FN{i}(:,4))
 ylabel('ln[I/V^2]')
 xlabel('1/V')
 title('FNT')
 legend('Reverse','Forward','Location','Southeast')
 xlim([-20 20])


 %ploting of Schottky
 subplot(3,2,3)
 plot(SE{i}(:,1),SE{i}(:,2))
 hold on
 plot(SE{i}(:,3),SE{i}(:,4))
 ylabel('ln[I/T^2]')
```

```
 xlabel('$\sqrt{V}$','Interpreter','Latex')
 title('Schottky')
 legend('Reverse','Forward','Location','Southeast')


 %plotting of PF
 subplot(3,2,4)
 plot(PF{i}(:,1),PF{i}(:,2))
 hold on
 plot(PF{i}(:,3),PF{i}(:,4))
 xlabel('$\sqrt{V}$','Interpreter','Latex')
 ylabel('ln[I/V]')
 title('Poole-Frenkel')
 legend('Reverse','Forward','Location','Southeast')

 %plotting TAT
 subplot(3,2,5)
 plot(TAT{i}(:,1),TAT{i}(:,2))
 hold on
 plot(TAT{i}(:,3),TAT{i}(:,4))
 ylabel('ln[I]')
 xlabel('1/V')
 title('Trap Assisted Tunneling')
 legend('Reverse','Forward','Location','Southeast')

 set(gcf,'PaperUnits','inches','PaperPosition',[0 0 16 12])







 testtype =num2str(i);
 print (testtype,'-dpng');
end


%GET Turn on Voltage TOV
TOV=[];

for i=1:length(fitIV)


 I=fitIV{i}(:,2);
 V=fitIV{i}(:,1);


 %take x1=3 and x2=3.2
```

```
 x1=V(end-20);
 x2=V(end);
 y1=I(end-20);
 y2=I(end);

 P=polyfit([x1,x2],[y1,y2],1);
 a=P(1);
 b=P(2);

 xint=-1*b/a;


 %  x=linspace(0,100,100);
 %  y=P(1).*x+P(2);
 %  plot(x,y)
 %
 TOV(i)=xint;

end
save('tov.mat','TOV')
```

Bibliography

[1] E. Donchev, J. S. Pang, P. M. Gammon, A. Centeno, F. Xie, P. K. Petrov, J. D. Breeze, M. P. Ryan, D. J. Riley, N. M. Alford, *MRS Energy Sustain.* **2014**, *1*, E1.

[2] M. N. Gadalla, M. Abdel-Rahman, A. Shamim, *Sci. Rep.* **2014**, *4*, 4270.

[3] K. Bhatt, C. C. Tripathi, *Indian J. Pure Appl. Phys.* **2015**, *53*, 827.

[4] I. E. Hashem, N. H. Rafat, E. A. Soliman, *IEEE J. Quantum Electron.* **2013**, *49*, 72.

[5] S. Grover, G. Moddel, *Solid. State. Electron.* **2012**, *67*, 94.

[6] K. Mistry, M. Yavuz, K. P. Musselman, *J. Appl. Phys.* **2017**, *121*, 184504.

[7] M. F. Zia, M. R. Abdel-Rahman, N. F. Al-Khalli, N. A. Debbar, In *Acta Physica Polonica A*; **2015**, *127*, 1289.

[8] A. Y. Elsharabasy, A. H. Alshehri, M. H. Bakr, M. J. Deen, K. P. Musselman, M. Yavuz, *AIP Adv.* **2019**, *9*.

[9] K. Choi, G. Ryu, F. Yesilkoy, A. Chryssis, N. Goldsman, M. Dagenais, M. Peckerar, *J. Vac. Sci. Technol. B, Nanotechnol. Microelectron. Mater. Process. Meas. Phenom.* **2010,** *28*, C6O50.

[10] S. Grover, G. Moddel, in *Rectenna Sol. Cells*, Springer, New York, USA **2013**.

[11] S. Krishnan, E. Stefanakos, S. Bhansali, *Thin Solid Films* **2008**, *516*, 2244.

[12] M. L. Chin, P. Periasamy, T. P. O'Regan, M. Amani, C. Tan, R. P. O'Hayre, J. J. Berry, R. M. Osgood, P. A. Parilla, D. S. Ginley, M. Dubey, *J. Vac. Sci. Technol. B Microelectron. Nanom. Struct.* **2013**, *31*, 051204.

[13] H. Koinuma, I. Takeuchi, *Nat. Mater.* **2004**, *3*, 429.

[14] N. Alimardani, J. M. McGlone, J. F. Wager, J. F. Conley, *J. Vac. Sci. Technol. A Vacuum, Surfaces, Film.* **2014**, *32*, 01A122.

[15] A. H. Alshehri, K. Mistry, V. H. Nguyen, K. H. Ibrahim, D. Muñoz-Rojas, M. Yavuz, K. P. Musselman, *Adv. Funct. Mater.* **2019**, *29*, 1805533.

[16] N. Alimardani, S. W. King, B. L. French, C. Tan, B. P. Lampert, J. F. Conley, *J. Appl. Phys.* **2014**,

116, 024508.

[17] M. Akram, S. Bashir, S. A. Jalil, M. S. Rafique, A. Hayat, K. Mahmood, *Appl. Phys. A Mater. Sci. Process.* **2018**, *124*, 180.

[18] S. Y. No, D. Eom, C. S. Hwang, H. J. Kim, *J. Electrochem. Soc.* **2006**, *100*, 024111.

[19] E. Suzuki, D. K. Schroder, Y. Hayashi, *J. Appl. Phys.* **1986**, *60*, 3616.

[20] J. Racko, M. Mikolášek, R. Granzner, J. Breza, D. Donoval, A. Grmanová, L. Harmatha, F. Schwierz, K. Fröhlich, *Cent. Eur. J. Phys.* **2011**, *9*, 230.

[21] W. J. Chang, M. P. Houng, Y. H. Wang, *J. Appl. Phys.* **2001**, *90*, 5171.

[22] B. Pelz, G. Moddel, *J. Appl. Phys.* **2019**, *125*, 234502.

[23] M. Abdel-Rahman, M. Syaryadhi, N. Debbar, *Electron. Lett.* **2013,** *49***,** 363.

[24] P. Periasamy, J. J. Berry, A. A. Dameron, J. D. Bergeson, D. S. Ginley, R. P. O'Hayre, P. A. Parilla, *Adv. Mater.* **2011**, *23*, 3080.

[25] M. Inac, A. Shafique, M. Ozcan, Y. Gurbuz, In *Thin Films for Solar and Energy Technology VII*; **2015**, *95610*, 95610M.

[26] F. Aydinoglu, M. Alhazmi, B. Cui, O. M. Ramahi, M. Irannejad, M. Yavuz, *Austin J. Nanomed. Nanotechnol* **2013**, *1*, 3.

[27] A. Mircea, A. Ougazzaden, G. Primot, C. Kazmierski, *J. Cryst. Growth* **1992**.

[28] A. Behnam, B. Hekmatshoar, S. Mohajerzadeh, B. Arvan, F. Karbassian, A. Khakifirooz, In *Materials Research Society Symposium Proceedings*; **2004**.

[29] Sharma, S.; Khawaja, M.; Ram, M. K.; Goswami, D. Y.; Stefanakos, E. *Beilstein J. Nanotechnol.* **2014,** *5*, 2240.

[30] I. Azad, M. K. Ram, D. Y. Goswami, E. Stefanakos, *Langmuir* **2016**, *32*, 8307.

[31] N. Debbar, M. Syaryadhi, M. Abdel-Rahman, *EPJAppl. Phys.* **2014**, 68, 30302.

[32] E. C. Kinzel, R. L. Brown, J. C. Ginn, B. A. Lail, B. A. Slovick, G. D. Boreman, *Microw. Opt. Technol. Lett.* **2013**, *55*, 489.

[33] I. Wilke, Y. Oppliger, W. Herrmann, F. K. Kneubühl, *Appl. Phys. A Solids Surfaces* **1994**, *58*, 329.

[34] E. W. Cowell, N. Alimardani, C. C. Knutson, J. F. Conley, D. A. Keszler, B. J. Gibbons, J. F. Wager, *Adv. Mater.* **2011**, *23*, 74.

[35] P. Periasamy, H. L. Guthrey, A. I. Abdulagatov, P. F. Ndione, J. J. Berry, D. S. Ginley, S. M. George, P. A. Parilla, R. P. O'Hayre, *Adv. Mater.* **2013**, *25*, 1301.

[36] J. A. Bean, B. Tiwari, G. H. Bernstein, P. Fay, W. Porod, *J. Vac. Sci. Technol. B Microelectron. Nanom. Struct.* **2009**, *27*, 11.

[37] B. Tiwari, J. A. Bean, G. Szakmány, G. H. Bernstein, P. Fay, W. Porod, *J. Vac. Sci. Technol. B Microelectron. Nanom. Struct.* **2009**, *27*, 2153.

[38] P. Maraghechi, A. Foroughi-Abari, K. Cadien, A. Y. Elezzabi, *Appl. Phys. Lett.* **2011**, *99*, 253503.

[39] S. B. Herner, A. D. Weerakkody, A. Belkadi, G. Moddel, *Appl. Phys. Lett.* **2017**, *110*, 223901.

[40] K. Bhatt, S. Kumar, C. C. Tripathi, *AEU - Int. J. Electron. Commun.* **2019**, *111*, 152925.

[41] P. Esfandiari, G. Bernstein, P. Fay, W. Porod, B. Rakos, A. Zarandy, B. Berland, L. Boloni, G. Boreman, B. Lail, B. Monacelli, A. Weeks, *Proc. SPIE* **2005**, *5783*, 471.

[42] A. Singh, R. Ratnadurai, R. Kumar, S. Krishnan, Y. Emirov, S. Bhansali, *Appl. Surf. Sci.* **2015**, *334*, 197.

[43] V. H. Nguyen, J. Resende, C. Jiménez, J. L. Deschanvres, P. Carroy, D. Muñoz, D. Bellet, D. Muñoz-Rojas, *J. Renew. Sustain. Energy* **2017**, *9*, 021203.

[44] D. H. Levy, S. F. Nelson, D. Freeman, *IEEE/OSA J. Disp. Technol.* **2009**.

[45] R. L. Z. Hoye, K. P. Musselman, M. R. Chua, A. Sadhanala, R. D. Raninga, J. L. MacManus-Driscoll, R. H. Friend, D. Credgington, *J. Mater. Chem. C* **2015**, *3*, 9327.

[46] K. P. Musselman, D. Muñoz-Rojas, R. L. Z. Hoye, H. Sun, S. L. Sahonta, E. Croft, M. L. Böhm, C. Ducati, J. L. MacManus-Driscoll, *Nanoscale Horizons* **2017**, *2*, 110.

[47] D. Muñoz-Rojas, V. Huong Nguyen, C. Masse de la Huerta, C. Jiménez, D. Bellet, In *Chemical Vapor Deposition for Nanotechnology*; IntechOpen, 2019.

[48] R. L. Z. Hoye, M. R. Chua, K. P. Musselman, G. Li, M. L. Lai, Z. K. Tan, N. C. Greenham, J. L. MacManus-Driscoll, R. H. Friend, D. Credgington, *Adv. Mater.* **2015**, *27*, 1414.

[49] N. Miura, T. Nanjo, M. Suita, T. Oishi, Y. Abe, T. Ozeki, H. Ishikawa, T. Egawa, T. Jimbo, *Solid.*

State. Electron. **2004**, *48*, 689.

[50] H. B. Michaelson, *J. Appl. Phys.* **1977**, *48*, 4729.

[51] F. C. Marques, J. J. Jasieniak, *Appl. Surf. Sci.* **2017**, *422*, 504.

[52] V. V. Afanas'Ev, M. Houssa, A. Stesmans, C. Merckling, T. Schram, J. A. Kittl, *Appl. Phys. Lett.* **2011**, *99*, 1785.

[53] K. B. Sundaram, A. Khan, In *Conference Proceedings - IEEE SOUTHEASTCON*; IEEE, **1996**, *15*, 674.

[54] S. Hemour, K. Wu, *Proc. IEEE* **2014**, *112*, 1667.

[55] Z. Zhang, R. Rajavel, P. Deelman, P. Fay, *IEEE Microw. Wirel. Components Lett.* **2011,** *21*, 267.

[56] A. H. Alshehri, A. Shahin, K. Mistry, K. H. Ibrahim, M. Yavuz, K. P. Musselman, *Adv. Electron. Mater.* **2021**, 2100467.

[57] A. H. Alshehri, N. Nelson-Fitzpatrick, K. H. Ibrahim, K. Mistry, M. Yavuz, K. P. Musselman, *J. Vac. Sci. Technol. A Vacuum, Surfaces, Film.* **2018**, *36*, 031602.

[58] M. Kim, K. M. Kang, Y. Wang, H. H. Park, *Thin Solid Films.* **2018**, *660*, 657.

[59] Y. J. Cho, H. Cha, H. S. Chang, *Surf. Coatings Technol.* **2016**, *307*, 1096.

[60] H. Y. Chen, H. L. Lu, J. X. Chen, F. Zhang, X. M. Ji, W. J. Liu, X. F. Yang, D. W. Zhang, *ACS Appl. Mater. Interfaces* **2017**, *9*, 44.

[61] J. Gangwar, B. K. Gupta, S. K. Tripathi, A. K. Srivastava, *Nanoscale* **2015**, *7*, 13313.

[62] K. Xu, H. Sio, O. A. Kirillov, L. Dong, M. Xu, P. D. Ye, D. Gundlach, N. V. Nguyen, *J. Appl. Phys.* **2013**, *113*.

[63] S. A. Ansari, M. M. Khan, M. O. Ansari, M. H. Cho, *New J. Chem.* **2016**, *40*, 3000.

[64] K. B. Jinesh, J. L. van Hemmen, M. C. M. van de Sanden, F. Roozeboom, J. H. Klootwijk, W. F. A. Besling, W. M. M. Kessels, *J. Electrochem. Soc.* **2011**, *158*, G21.

[65] P. K. Nayak, J. A. Caraveo-Frescas, Z. Wang, M. N. Hedhili, Q. X. Wang, H. N. Alshareef, *Sci. Rep.* **2014**, *4*, 4672.

[66] R-C. Fang, Q-Q. Sun, P. Zhou, W. Yang, P-F. Wang, D. W. Zhang, *Nanoscale Res. Lett.* **2013**, *8*,

92.

[67] C. Sun, R. Zeng, J. Zhang, Z. J. Qiu, D. Wu, *Materials.* **2017**, *10*, 1432.

[68] F. Zou, Z. Jiang, X. Qin, Y. Zhao, L. Jiang, J. Zhi, T. Xiao, P. P. Edwards, *Chem. Commun.* **2012**, *285*, 559.

[69] B. Viswanathan, K. R. Krishanmurthy, *Int. J. Photoenergy* **2012**, *2012*, 10.

[70] G. Yang, T. Wang, B. Yang, Z. Yan, S. Ding, T. Xiao, *Appl. Surf. Sci.* **2013**, *287*, 135.

[71] W. Orellana, A. J. R. Da Silva, A. Fazzio, *Phys. Rev. B* **2004**, *70*, 125206.

[72] H. M. Kwon, W. H. Choi, I. S. Han, S. U. Park, B. S. Park, Y. Y. Zhang, C. Y. Kang, B. H. Lee, R. Jammy, H. D. Lee, *Microelectron. Eng.* **2011**, *88*, 3415.

[73] H. M. Kwon, W. H. Choi, I. S. Han, M. K. Na, S. U. Park, J. D. Bok, C. Y. Kang, B. H. Lee, R. Jammy, H. D. Lee, *Microelectron. Eng.* **2011**, *88*, 3399.

[74] A. P. Huang, X. H. Zheng, Z. S. Xiao, M. Wang, Z. F. Di, P. K. Chu, *Chinese Sci. Bull.* **2012**, *57*, 2872.

[75] B. Pelz, A. Belkadi, G. Moddel, *Meas. J. Int. Meas. Confed.* **2018**, *120*, 28.

[76] A. Ortiz-Conde, F. J. García Sánchez, J. J. Liou, A. Cerdeira, M. Estrada, Y. Yue, *Microelectron. Reliab.* **2002**, *42*, 583.

[77] H. W. Chen, Y. Ku, Y. L. Kuo, *Water Res.* **2007**, *41*, 2069.

[78] R. A. Wood, in *Infrared Detectors and Emitters: Materials and Devices* (Eds: P. Capper, C. T. Elliot) Kluwer Academic Publishers, Norwell, USA **2001**.

[79] M. P. Houng, Y. H. Wang, W. J. Chang, *J. Appl. Phys.* **1999**, *86*, 1488.

[80] Y. Tian, L. Jiang, X. Zhang, G. Zhang, Q. Zhu, *AIP Adv.* **2018**, *8*, 035105.

[81] S. Kasap, P. Capper, *Springer Handbook of Electronic and Photonic Materials*, Springer Science & Business Media, Berlin **2017**.

[82] D. S. Jeong, H. B. Park, C. S. Hwang, *Appl. Phys. Lett.* **2005**, *86*, 072903.

[83] D. S. Jeong, C. S. Hwang, *J. Appl. Phys.* **2005**, *98*, 113701.

[84] S. Yu, X. Guan, H. S. P. Wong, *Appl. Phys. Lett.* **2011**, *99*, 063507.

[85] S. Brad Herner, A. Belkadi, A. Weerakkody, B. Pelz, G. Moddel, *IEEE J. Photovoltaics* **2018**, *8*, 499.

[86] F. C. Chiu, *Adv. Mater. Sci. Eng.* **2014**, *2014*, 578168.

[87] K. Yoshitsugu, M. Horita, Y. Ishikawa, Y. Uraoka, *Phys. Status Solidi Curr. Top. Solid State Phys.* **2013**, *10*, 1426.

[88] C. A. Schmuttenmaer, *Terahertz Sci. Technol.*, **2008**, *1*, 1.

[89] J. Hu, A. Nainani, Y. Sun, K. C. Saraswat, H. S. Philip Wong, *Appl. Phys. Lett.* **2011**, *99*, 252104.

[90] A. Sanchez, C. F. Davis, K. C. Liu, A. Javan, *J. Appl. Phys.* **1978**, *49*, 5270.

[91] J. Hu, K. C. Saraswat, H. S. Philip Wong, *Appl. Phys. Lett.* **2011**, *99*, 092107.

[92] M. Aldrigo, M. Dragoman, M. Modreanu, I. Povey, S. Iordanescu, D. Vasilache, A. Dinescu, M. Shanawani, D. Masotti, *IEEE Trans. Electron Devices* **2018**, *65*, 2973.

[93] S. M. Prokes, M. B. Katz, M. E. Twigg, *APL Mater.* **2014**, *2*, 032105.

[94] J. Yang, B. S. Eller, R. J. Nemanich, *J. Appl. Phys.* **2014**, *116*, 123702.

[95] A. M. Rana, T. Akbar, M. Ismail, E. Ahmad, F. Hussain, I. Talib, M. Imran, K. Mehmood, K. Iqbal, M. Y. Nadeem, *Sci. Rep.* **2017**, *7*, 1.

[96] R. M. Eastment, C. H. B. Mee, *J. Phys. F Met. Phys.* **1973**, *3*, 1738.

[97] H. Spahr, S. Montzka, J. Reinker, F. Hirschberg, W. Kowalsky, H. H. Johannes, *J. Appl. Phys.* **2013**, *114*, 183714.

[98] S. Miyazaki, *J. Vac. Sci. Technol. B Microelectron. Nanom. Struct.* **2001**, *19*, 2212.

[99] A. M. Goodman, *J. Appl. Phys.* **1970**, *41*, 2176.

[100] E. W. Cowell, S. W. Muir, D. A. Keszler, J. F. Wager, *J. Appl. Phys.* **2013**, *114*, 213703.

[101] J. L. van Hemmen, S. B. S. Heil, J. H. Klootwijk, F. Roozeboom, C. J. Hodson, M. C. M. van de Sanden, W. M. M. Kessels, *J. Electrochem. Soc.* **2007**, *154*, G165.

[102] I. N. Reddy, V. R. Reddy, A. Dey, N. Sridhara, S. Basavaraja, P. Bera, C. Anandan, A. K. Sharma, *Surf. Eng.* **2014**, *40*, 11099.

[103] A. M. Saranya, A. Morata, D. Pla, M. Burriel, F. Chiabrera, I. Garbayo, A. Hornés, J. A. Kilner,

A. Tarancón, *Chem. Mater.* **2018**, *30*, 5621.

[104] M. Reinke, Y. Kuzminykh, P. Hoffmann, *Chem. Mater.* **2015**, *27*, 1604.

[105] W. Lei, L. Henn-Lecordier, M. Anderle, G. W. Rubloff, M. Barozzi, M. Bersani, *J. Vac. Sci. Technol. B Microelectron. Nanom. Struct.* **2006**, *24*, 780.

[106] H. Salami, A. Poissant, R. A. Adomaitis, *J. Vac. Sci. Technol. A Vacuum, Surfaces, Film.* **2017**, *35*, 01B101.

[107] A. Kafizas, C. Crick, I. P. Parkin, *J. Photochem. Photobiol. A Chem.* **2010**, *216*, 156.

[108] M. Pavan, S. Rühle, A. Ginsburg, D. A. Keller, H. N. Barad, P. M. Sberna, D. Nunes, R. Martins, A. Y. Anderson, A. Zaban, E. Fortunato, *Sol. Energy Mater. Sol. Cells* **2015**, *132*, 549.

[109] Dedova, *PhD Thesis*, Tallinn University of Technology, October, **2007**.

[110] C. M. Stafford, K. E. Roskov, T. H. Epps, M. J. Fasolka, *Rev. Sci. Instrum.* **2006**, *77*, 023908.

[111] R. L. Davis, S. Jayaraman, P. M. Chaikin, R. A. Register, *Langmuir* **2014**, *30*, 5637.

[112] Y. W. Lai, M. Krause, A. Savan, S. Thienhaus, N. Koukourakis, M. R. Hofmann, A. Ludwig, *Sci. Technol. Adv. Mater.* **2011**, *12*, 054201.

[113] H. Oguchi, J. Hattrick-Simpers, I. Takeuchi, E. J. Heilweil, L. A. Bendersky, *Rev. Sci. Instrum.* **2009**, *80*, 073707.

[114] A. Kafizas, G. Hyett, I. P. Parkin, *J. Mater. Chem.* **2009**, *9*, 1399.

[115] S. Klinkhammer, X. Liu, K. Huska, Y. Shen, S. Vanderheiden, S. Valouch, C. Vannahme, S. Bräse, T. Mappes, U. Lemmer, *Opt. Express* **2012**, *20*, 6357.

[116] A. H. Alshehri, J. Y. Loke, V. H. Nguyen, A. Jones, H. Asgarimoghaddam, L. V. Delumeau, A. Shahin, K. H. Ibrahim, K. Mistry, M. Yavuz, D. Muñoz-Rojas, K. P. Musselman, *Adv. Funct. Mater.* **2021**, *31*, 2103271.

[117] P. Poodt, D. C. Cameron, E. Dickey, S. M. George, V. Kuznetsov, G. N. Parsons, F. Roozeboom, G. Sundaram, A. Vermeer, *J. Vac. Sci. Technol. A* **2012**, *30*, 010802.

[118] K. P. Musselman, C. F. Uzoma, M. S. Miller, *Chem. Mater.* **2016**, *28*, 8443.

[119] Alshehri, *Master thesis*, University of Waterloo, July, **2017**.

[120] C. M. de la Huerta, V. H. Nguyen, J. M. Dedulle, D. Bellet, C. Jiménez, D. Muñoz-Rojas, *Coatings* **2019**, *9*, 5.

[121] V. H. Nguyen, A. Sekkat, C. A. Masse de la Huerta, F. Zoubian, C. Crivello, J. Rubio-Zuazo, M. Jaffal, M. Bonvalot, C. Vallée, O. Aubry, H. Rabat, D. Hong, D. Muñoz-Rojas, *Chem. Mater.* **2020**, *32*, 5153.

[122] K. Mistry, A. Jones, M. Kao, T. W.-K. Yeow, M. Yavuz, K. P. Musselman, *Nano Express* **2020**, *1*, 010045.

[123] C. Barbos, D. Blanc-Pelissier, A. Fave, E. Blanquet, A. Crisci, E. Fourmond, D. Albertini, A. Sabac, K. Ayadi, P. Girard, M. Lemiti, in *Energy Procedia*, **2015**, *77*, 558.

[124] Y. Zhang, M. Creatore, Q. B. Ma, A. El Boukili, L. Gao, M. A. Verheijen, M. W. G. M. T. Verhoeven, E. J. M. Hensen, *Appl. Surf. Sci.* **2015**, *330*, 476.

[125] A. Monshi, M. R. Foroughi, M. R. Monshi, *World J. Nano Sci. Eng.* **2012**, *02*, 154.

[126] J. M. Myoung, W. H. Yoon, D. H. Lee, I. Yun, S. H. Bae, S. Y. Lee, *Japanese J. Appl. Physics, Part 1 Regul. Pap. Short Notes Rev. Pap.* **2002**, *41*, 28.

[127] A. Yahyaoui, A. Elsharabasy, J. Yousaf, H. Rmili, **2020**, *20*, 7023.

[128] A. Belkadi, A. Weerakkody, G. Moddel, *Nat. Commun.* **2021**, *12*, 2925.

[129] M. A. Green, A. Ho-Baillie, H. J. Snaith, *Nat. Photonics* **2014**, *8*, 506.

[130] W. S. Yang, B. W. Park, E. H. Jung, N. J. Jeon, Y. C. Kim, D. U. Lee, S. S. Shin, J. Seo, E. K. Kim, J. H. Noh, S. Il Seok, *Science* **2017**, *356*, 1376.

[131] NREL, Best Research-CellEfficiencies Chart, www.nrel.gov/pv/assets/images/efficiency-chart.png, accessed: September, **2020**.

[132] D. Zhou, T. Zhou, Y. Tian, X. Zhu, Y. Tu, *J. Nanomater.* **2018**, *2018*, 8148072.

[133] K. Ibrahim, A. Shahin, A. Jones, A. H. Alshehri, K. Mistry, M. D. Singh, F. Ye, J. Sanderson, M. Yavuz, K. P. Musselman, *Sol. Energy* **2021**, *224*, 787.

[134] N. G. Park, *J. Phys. Chem. Lett.* **2013**, *4*, 2423.

[135] V. Zardetto, B. L. Williams, A. Perrotta, F. Di Giacomo, M. A. Verheijen, R. Andriessen, W. M. M. Kessels, M. Creatore, *Sustain. Energy Fuels* **2017**, *1*, 30.

[136] J. A. Raiford, S. T. Oyakhire, S. F. Bent, *Energy Environ. Sci.* **2020**, *13*, 1997.

[137] J. Li, R. Xia, W. Qi, X. Zhou, J. Cheng, Y. Chen, G. Hou, Y. Ding, Y. Li, Y. Zhao, X. Zhang, *J. Power Sources* **2021**, *485*, 229313.

[138] F. J. Ramos, T. Maindron, S. Béchu, A. Rebai, M. Frégnaux, M. Bouttemy, J. Rousset, P. Schulz, N. Schneider, *Sustain. Energy Fuels* **2018**, *2*, 2468.

[139] Y. Il Lee, N. J. Jeon, B. J. Kim, H. Shim, T. Y. Yang, S. Il Seok, J. Seo, S. G. Im, *Adv. Energy Mater.* **2018**, *8*, 1701928.

[140] L. Hoffmann, D. Theirich, S. Pack, F. Kocak, D. Schlamm, T. Hasselmann, H. Fahl, A. Raupke, H. Gargouri, T. Riedl, *ACS Appl. Mater. Interfaces* **2017**, *9*, 4171.

[141] R. D. Raninga, R. A. Jagt, S. Béchu, T. N. Huq, W. Li, M. Nikolka, Y. H. Lin, M. Sun, Z. Li, W. Li, M. Bouttemy, M. Frégnaux, H. J. Snaith, P. Schulz, J. L. MacManus-Driscoll, R. L. Z. Hoye, *Nano Energy* **2020**, *75*, 104946.

[142] L. Hoffmann, K. O. Brinkmann, J. Malerczyk, D. Rogalla, T. Becker, D. Theirich, I. Shutsko, P. Görrn, T. Riedl, *ACS Appl. Mater. Interfaces* **2018**, *10*, 6006.

[143] Y. Lv, P. Xu, G. Ren, F. Chen, H. Nan, R. Liu, D. Wang, X. Tan, X. Liu, H. Zhang, Z. K. Chen, *ACS Appl. Mater. Interfaces* **2018**, *10*, 23928.

[144] H. Klumbies, P. Schmidt, M. Hähnel, A. Singh, U. Schroeder, C. Richter, T. Mikolajick, C. Hoßbach, M. Albert, J. W. Bartha, K. Leo, L. Müller-Meskamp, *Org. Electron.* **2015**, *17*, 138.

[145] M. D. Groner, S. M. George, R. S. McLean, P. F. Carcia, *Appl. Phys. Lett.* **2006**, *88*, 051907.

[146] E. Kim, Y. Han, W. Kim, K. C. Choi, H. G. Im, B. S. Bae, *Org. Electron.* **2013**, *14*, 1737.

[147] K. L. Jarvis, P. J. Evans, *Thin Solid Films* **2017**, *624*, 111.

[148] C. Besleaga, L. E. Abramiuc, V. Stancu, A. G. Tomulescu, M. Sima, L. Trinca, N. Plugaru, L. Pintilie, G. A. Nemnes, M. Iliescu, H. G. Svavarsson, A. Manolescu, I. Pintilie, *J. Phys. Chem. Lett.* **2016**, *24*, 5168.

[149] X. Wang, S. Shen, Z. Feng, C. Li, *Cuihua Xuebao/Chinese J. Catal.* **2016**, *37*, 2059.

[150] J. Shi, J. Chen, Z. Feng, T. Chen, Y. Lian, X. Wang, C. Li, *J. Phys. Chem. C* **2007**, *111*, 693.

[151] S. Masubuchi, E. Watanabe, Y. Seo, S. Okazaki, T. Sasagawa, K. Watanabe, T. Taniguchi, T.

Machida, *npj 2D Mater. Appl.* **2020**, *4*, 1.

[152] S. Liu, C. N. Melton, S. Venkatakrishnan, R. J. Pandolfi, G. Freychet, D. Kumar, H. Tang, A. Hexemer, D. M. Ushizima, *MRS Commun.* **2019**, *9*, 586.

[153] G. B. Goh, A. Vishnu, C. Siegel, N. Hodas, inKDD '*18 Proc. of the 24th ACM SIGKDD Int. Conf. Knowl. Discov. Data Min*. **2018**, *1*, 302.

[154] A. Krizhevsky, I. Sutskever, G. E. Hinton, *Commun. ACM* **2017**, *60*, 84.

[155] S. Seo, S. Jeong, C. Bae, N. G. Park, H. Shin, *Adv. Mater.* **2018**, *30*, 1801010.

[156] R. Singh, S. Ghosh, A. S. Subbiah, N. Mahuli, S. K. Sarkar, *Sol. Energy Mater. Sol. Cells* **2020**, *205*, 110289.

[157] C. Y. Chang, K. T. Lee, W. K. Huang, H. Y. Siao, Y. C. Chang, *Chem. Mater.* **2015**, *27*, 5122.

[158] S. J. Kim, S. H. Yong, Y. J. Choi, H. Hwangbo, W.-Y. Yang, H. Chae, *J. Vac. Sci. Technol. A* **2020**, *38*, 022418.

[159] I. S. Kim, A. B. F. Martinson, *J. Mater. Chem. A* **2015**, *3*, 20092.

[160] D. Koushik, W. J. H. Verhees, Y. Kuang, S. Veenstra, D. Zhang, M. A. Verheijen, M. Creatore, R. E. I. Schropp, *Energy Environ. Sci.* **2017**, *10*, 91.

[161] M. Xiao, K. P. Musselman, W. W. Duley, N. Y. Zhou, *Nano-Micro Lett.* **2017**, *9*, 1.

[162] M. A. Dominguez, J. A. Luna-Lopez, S. Ceron, *Thin Solid Films* **2018**, *645*, 278.

[163] T. Kubo, J. J. Freedsman, Y. Iwata, T. Egawa, *Semicond. Sci. Technol.* **2014**, *29*. 045004.

[164] C. Martínez-Domingo, S. Conti, L. Terés, H. Gomes, E. Ramon, *Organic Electronics*. **2018**, *62*, 335.

Chapter 11
Contributions

1. **Abdullah H. Alshehri**, Ahmed Shahin, Kissan Mistry, Khaled Ibrahim, Mustafa Yavuz, Kevin. Musselman. *Metal-Insulator-Insulator-Metal Diodes with Responsivities Greater Than 30 A/W Based on Nitrogen-Doped TiO_x and AlO_x Insulator Layers*. Advanced Electronic Materials, **2021**, 2100467.
2. Khaled Ibrahim, Ahmed Shahin, Alexander Jones, **Abdullah H. Alshehri**, Kissan Mistry, Michael Singh, Fan Ye, Joseph Sanderson, Mustafa Yavuz, Kevin Musselman. *Humidity-resistant perovskite solar cells via the incorporation of halogenated graphene particles.* Solar Energy, **2021**, *224*, 787.
3. **Abdullah H. Alshehri,** Jhi Loke, Viet Nguyen, Alexander Jones, Hatameh Asgarimoghaddam, Louis-Vincent Delumeau, Ahmed Shahin, Khaled Ibrahim, Kissan Mistry, Mustafa Yavuz, David Muñoz-Rojas, and Kevin Musselman. *Nanoscale film Thickness Gradients Printed in Open Air by Spatially Varying Chemical Vapor Deposition.* Advanced Functional Materials, **2021**, *31*, 2103271.
4. **Abdullah H. Alshehri,** Khaled H. Ibrahim, Kissan Mistry, Viet Nguyen, David Muñoz-Rojas, Mustafa Yavuz, Kevin P. Musselman. *Quantum-Tunneling Metal-Insulator-Metal Diodes Made by Rapid Atmospheric Pressure Chemical Vapor Deposition*. Advanced Functional Materials, **2019**, *29*, 1805533.

5. Ahmed Y. Elsharabasy, **Abdullah H. Alshehri,** Bakr, M. H., Deen, M. J., Musselman, K. P., & Yavuz, M. (2019). *Near zero-bias MIIM diode based on TiO_2/ZnO for energy harvesting applications*. *AIP Advances*. **2019**, *9*, 115207.
6. **Abdullah H. Alshehri**, Nelson-Fitzpatrick, N., Ibrahim, K. H., Mistry, K., Yavuz, M., & Musselman, K. P. *Simple plasma assisted atomic layer deposition technique for high substitutional nitrogen doping of TiO_2. Journal of Vacuum Science & Technology A: Vacuum, Surfaces, and Films,* **2018**. *36*, 031602.